Large structures simulation for landscape evolution models

Julien Coatléven[1] and Benoit Chauveau[1]

[1]IFP Énergies nouvelles, 1 et 4 avenue de Bois-Préau, 92852 Rueil-Malmaison, France

Correspondence: Julien Coatléven (julien.coatleven@ifpen.fr)

Abstract. ~~Because of the chaotic behavior of the coupling between water flow and sediment erosion and transport, without any special treatment the practical results of landscape evolution models~~ The aim of this paper is to discuss the efficiency of a new methodology to maintain the accuracy of numerical solutions obtained from our landscape evolution model (LEM)~~are likely to be dominated by numerical errors. This paper describes two areas of improvement that we believe are necessary for the successful simulation of landscape evolution models. The first one concerns the expression of the water flux that was initially rebuilt in ? in a mathematically consistent way for the cell-to-cell multiple flow direction algorithms, thanks to a reinterpretation as a well chosen discretization of the Gauckler-Manning-Strickler continuous equation. Building on those results, we introduce here a general framework allowing to derive consistent expressions of the water flux for the most commonly used multiple/single flow direction (MFD/SFD) water flow routines, including node-to-node versions. If having a consistent water flux is crucial to avoid any mesh size dependence in a LEM and controlling the consistency error, the expected~~ . As in every LEM, the tricky part is the coupling between water and sediment flows that drives the non-linear self amplification mechanisms~~of the water and sediment coupling can still lead to simulations blurred by numerical errors. Those~~ . But this coupling is also responsible for the emergence and amplification of numerical errors, as we illustrate here. These numerical instabilities being ~~highly reminiscent of turbulence induced~~ strongly reminiscent of turbulence-induced instabilities in computational fluid dynamics (CFD), ~~in the second part of our paper we present a "large structure simulation"~~ we introduce a "large structures simulation" (LSS) approach for LEM, mimicking the ~~large-eddy~~ large eddy simulations (LES) used for turbulent CFD. ~~The LSS allows to control numerical errors while preserving the major physical based geomorphic patterns~~In practice, this treatment consists in a filtering strategy that controls small-scale perturbations in the solution. We demonstrate the accuracy of the LSS approach in the context of our LEM model.

1 Introduction

Since the pioneering work of Gilbert in the XIX century (**?**), the meaning of the term "landscape evolution model" (LEM) has evolved until reaching in the late XX century its modern definition. It is now considered has a numerical application of a mathematical system that seeks to simulate a part of the physical processes controlling the landscape dynamic. The capabil-

ity of LEMs to provide an integrated simulation in which several processes are addressed make them particularly relevant to tackle a large variety of contexts~~, such as the imprint of the upper mantle on the history of a sedimentary basin over thousands to millions of years (e. g., **??**), the control exerted by glacial dynamics (**??**), or the impact of climate change at variable time-scales on drainage basins and soils (e.g., **????**).~~ . The success of those numerical approaches depends on their ability to correctly handle the positive non-linear feedback between the water flow~~and~~ , the sediment erosion and deposition in a decent computational time. This non-linear coupling between water and sediments is indeed expected to potentially induce complex water flow networks even on initially small topographic variations, allowing in return the emergence of complex geomorphic landforms. ~~However, in the absence of reference analytic solutions, it is hard to~~ Some algorithms, in particular the family of MFD algorithms, have long been developed for solving surface water flow models in a low computational time. Until very recently, these solvers were not really linked to any physical model, which ruled out the use of an analytic solution to compare practical numerical results. It was therefore difficult to decipher if the obtained landform results only from physical processes or from the self-amplification of initially small numerical errors. ~~The objective of the present paper is to propose a general approach to considerably diminish the risk of producing inconsistent numerical results. The first ingredient is obviously to make sure to remove any anomalous consistency error in the numerical schemes, while the second one consists in introducing a method to control the evolution of the numerical errors. We believe that any LEMs developer will take advantage in following the recommendations resulting from this two topics, whatever the space and time scales considered. There is a wide variety of mathematical models describing the flow of water , depending on the prominent space and time scales of the considered problem. The most complete model is the Navier-Stokes model which allows for very precise but prohibitively costly simulations. The shallow-water approximation is sometimes used to solve rivers system (e.g. **?**) or to simulate glacial dynamics **?**. Despite a reduced computational cost compared to the Navier-Stokes model, this model has not been often explicitly deployed in LEMs. Probably one of the reasons is that computationally efficient water flow routing algorithms have been developed during the last decades. Those algorithms are built assuming that the water flow follows the direction of steepest descent (e.g. **???????**), and are able to simulate relatively complex water flow networks despite this inherent simplicity. Multiple flow direction (MFD) and single flow direction (SFD) algorithms are among the most known water-flow routing families implemented in reference LEMs such as in SIBERIA(**???**), CAESAR-Lisflood (**??**), FastScape (**?**), eSCAPE (**?**), CIDRE (**?**), EROS (**?**) or BadLand (**?**), or in stratigraphic models such as DionisosFlow (**?**). This list being not exhaustive, the reader is referred to **?????** for a complete review. The main differences between them is in their representation of the discretized domain (cell-to-cell or node-to-node interaction following the terminology in **?**) and by the empirical choice made to distribute water among the mesh elements. The empirical foundations of the MFD/SFD water flow routing and their lack of mathematical framework make them very difficult to validate. A first behavior known since a long time is not very encouraging: the water flow distribution $\mathcal{Q}_w$ is mesh dependent. This is probably the most documented problem of the LEM community since more than twenty years (e.g. **???**) and one that still disturbs current models. Smart solutions have been published to minimize this effect without making it completely vanish (**??**), while alternatively it was proposed to redefine drainage area at the continuous level **??** to allow a consistent discretization of $\mathcal{Q}_w$. From a mathematical point of view, it has been quite recently understood by **?** that the~~ An alternative definition of the specific catchment area often used to model water flow was proposed in

??, consisting in solving an abstract uniform flow equation in replacement of using one of the MFD algorithms. Independently and following an another path, in ? a first MFD algorithms family (those for which water is transferred from cell to cell) has been proved to coincide on cartesian meshes with a classical discretization of the water ~~discharge obtained from the cell-to-cell MFD/SFD corresponds in fact to a non-consistent approximation of the water flux of a Gauckler-Manning-Strickler model , a simplification of the shallow water model~~ mass conservation Gauckler-Manning-Strickler model (GMS). ~~This allowed ? to correct the MFD/SFD to obtain a consistent and thus mesh independent approximation for Q_w, in the usual numerical analysis sense of convergence when the mesh size go to zero. The first purpose of this paper is consequently to recall this result and then to explicitly show how all the classical MFD/SFD algorithms, even the node-to-node versions, can be in fact interpreted and thus corrected in the same way slightly generalizing the results of ? and finally solving the grid dependency issue. Because of~~ The output of the MFD algorithms is exactly a mesh-dependent mean of the water flux associated with the discrete GMS model. This result explains the mesh and numerical dependency since the output of the MFD does not fulfill the consistency criteria, but it also provides a way to correct it in a post-processing step leading to a consistent discrete approximation of the GMS water flux, extended in ? to general polygonal meshes. As the GMS model can be seen as a generalization of the model proposed in ??, this finally closes the loop between MFD algorithms and the specific catchment area defined in ?? (more details are given in section ??). For those reasons, in the present paper we will use a general GMS model to compute our water flow.

This paper has two objectives: (1) to investigate the conditions for which the geomorphic structures simulated from of a landscape evolution model derive from numerical instabilities; (2) to introduce a methodology that improves the accuracy of the numerical solution and to discuss its potential importance for LEMs. The landscape evolution model used in this paper considers the GMS model for the surface water flow coupled with a representative erosion and deposition sediment flux model detailed in section (??), that has been previously used for instance in ???? and which is a generalization of the models studied in ??. The linear stability analysis of this model brings out the key parameters that control the self-amplification mechanisms ~~at the core of the equation system and that are assumed to play a major role in valleys formation and their spacing (see ????), solving the consistency issue in these LEMs is thus absolutely necessary to avoid creating anomalous numerical errors but yet but not sufficient to guarantee that results are not dominated by numerical errors . Unless some special numerical treatment is added, the expected~~ of the various water-sediment flow regimes (see section ??). To illustrate the related numerical issues, we test the convergence of numerical solutions towards some prescribed analytic solutions for various water-driven and gravity transport coefficients. Comparison between the analytic and numerical solutions leads us to the conclusion that numerical errors must be treated with the greatest care to avoid any misinterpretation of LEM results: the self-amplification processes ~~can indeed also~~ at the core of the coupling between water flow and sediment evolution can amplify legitimate numerical round-off or solver errors~~up to the point that they potentially completely blur the numerical solution.This~~ . Thus estimating the relative impact of numerical errors on the final geomorphologic structures is challenging, making potentially hazardous the use of numerical approaches in particular those involving implicit time schemes to discuss and quantify the role of self-amplification mechanisms in realistic geodynamic contexts (e.g. the valley formation and spacing ????).

This self-amplification ("butterfly effect") is very reminiscent of the ~~turbulence issue~~ numerical issues arising in the field

of computational fluid dynamics (CFD) ~~. This observation~~ for turbulent flows, which prevents the use of direct numerical simulation for high Reynolds numbers unless high order methods are used over small space and time scales (along with sometimes some blow up problems). This comparison with CFD and turbulent flows is not new and was studied in details for instance in **??**. The modern solution found by the CFD community to achieve reproducible and meaningful simulations is to replace direct numerical simulation (DNS) of the Navier-Stokes equations by large eddy simulation (LES, **?**). The objective of LES is to obtain a ~~correct~~ good approximation of local spatial averages of turbulent flows, recovering the correct dynamics only for the organized structures of the flow (the eddies) which are larger than ~~some~~ a certain α target length scale~~α~~. Thus, LES chooses to abandon the idea of resolving all the scales involved in ~~the true~~ real physical processes, as there is no hope ~~to use~~ of using a mesh fine enough to ~~correctly~~ resolve the smallest scales correctly. In practice this is done by filtering the solution to distinguish ~~between the behavior of the flow~~ the flow behavior above and below α, and obtaining local averages that are ~~smoother and as mesh independent as~~ smooth and mesh-independent as possible. To our knowledge, the first attempt at using ~~an~~ a LES approach for simulating landscape evolution albeit without explicitly mentioning LES is **?**, where a Laplacian smoothing (equivalent to a mesh related box filter in the LES terminology) was applied ~~on the~~ to topography. More recently **??** ~~resorted to a mono-directional domain size related box filter~~ have used an average in one direction (which is a limit case of filtering) to obtain robust results on channelization statistics and scaling signatures: in other words they substitute the elevation and the specific drainage area by their mean values in the axial direction of their rectangular simulated domain. In their conclusion they suggest that the use of more general LES approaches seems a viable avenue for more complex landscape evolution simulations. In line with this observation, we also believe that the success of the attempts of **???**, as well the numerous analogies between the instabilities arising in landscape evolution models and turbulence reported in **????** ~~as well as~~ and the numerical experiments strongly advocate for the use of some LES technology to overcome the numerical issues arising in the non-linear coupling of sediment evolution and water flow. ~~Those are the reasons why we have considered deriving a "large structures simulation" (LSS) approach for landscape evolution. We will see that the numerical results of LSS seem remarkably reproducible~~Our main contribution is precisely to develop a LES-type methodolgy for our LEM. We refer to this method by the acronym LSS for "large structure simulation". Notice that contrary to **??** and more in line to what is done in the CFD community, we ~~will~~ fix a length scale that ~~will correspond~~ corresponds to the size of the smallest structures we want to resolve in the problem, quite independently of the domain size. We also consider a more advanced differential filter, namely the Leray-α filter (**??**) that is not related to any specific geometric configuration. In this sense, our work can be considered as a generalization of **??**. We ~~will show that the~~ show that when the filter size is correctly defined the results obtained from the LSS are actually free of the non-physical heterogeneity~~that appeared spontaneously from numerical errors. Notice that those numerical artifacts were often misleading as they induced more "realistic looking" solutions than the correct ones obtained by the LSS, in the sense that the obtained topography was more complex . Starting from the LSS approach, it then becomes relevant to inject physically controlled heterogeneity in order to bring out the complexity in the results. The two items addressed in this paper are complementary and should benefit to every LEMs.~~. We also highlight the difficulty to predict the "correct" filter size.

Obtaining a reproducible result and as error-free and mesh-independent as possible is, of course, what every modeler expects. On the other hand, the emergence of complex geomorphologic structures, which is an objective sought by many LEM users,

requires to manually introduce relevant physical heterogeneity after handling numerical errors. Several of our simulations are consequently performed using different types of heterogeneity carried by the initial topography or by other physical parameters, such as a a variable roughness index or a variable rain map. The ~~paper will be organized accordingly. In the first part we introduce the notations to describe a sedimentary system. The second part tackles the issue of the consistency in the MFD/SFD algorithms. After recalling the results of **?** on the classical cell-to-cell MFD algorithms, we detail the extension to the most classical MFD/SFD node-to-node algorithms of the literature. The resulting relations between the Gauckler-Manning-Strickler~~ emergence of large geomorphic structures is discussed by taking into consideration the understanding gained from this work.

The paper is organized as follows. We begin by introducing the water flow and the sediment flow models of the LEM used to perform the simulations discussed in this paper. We then construct analytic solutions and proceed to a comparison with numerical results in the relevant flow regimes. This leads to the first conclusion that for the studied landscape evolution model and the ~~water flow routing are summarized in a synthesis table, which should help the developer to implement a consistent version of the flow routing used in its landscape model. The third section of~~ considered classical implicit finite volume discretization, without any specific treatment, the obtained numerical solutions are potentially controlled by numerical errors. The second step of this work is to introduce and apply the filtering strategy on the ~~paper starts by illustrating on an easy to analyze synthetic sedimentary system the issue related to the self-reinforcement between the water flow and the sediment dynamics. We then introduce the LES inspired filtering strategy and apply this "large structure simulation" (LSS) approach on the illustrative test case as well as on a more complex model~~water-sediment equation system. The comparison between numerical and analytic solutions clearly shows the crucial role played by this method. Finally, we illustrate the behavior of our LEM in more complex contexts and we test the impact of variable (in space and time) roughness coefficients and rain maps in the final solution.

2 Model and notation

Following **?**, we assume that a sedimentary system can be idealized through the following assumptions: (H1) the basin topography can be represented as a mathematical surface, (H2) the principle of the conservation of mass applies to this surface, (H3) the sediment flux at any point of the surface is a function of the local slope and the local discharge of water. In other words, using an Eulerian approach (H1) implies that we consider a fixed geographical region over the time period $]0,T[$ mathematically modeled by means of a domain $\Omega \in \mathbb{R}^2$, a function $b : \Omega \times]0,T[\longrightarrow \mathbb{R}$ describing the basement i.e. the lower part of the basin in the z direction, and a function $h_s : \Omega \times]0,T[\longrightarrow \mathbb{R}$ describing the thickness of the sediments (see Fig. **??**). Thus, our basin $\mathcal{B} :]0,T[\longrightarrow \mathbb{R}^3$ can be described for almost every (a.e.) $t \in]0,T[$ by:

$$\mathcal{B}(t) = \left\{ (x,y,z) \in \mathbb{R}^3 \;\middle|\; (x,y) \in \Omega \text{ and } b(x,y,t) \leq z \leq b(x,y,t) + h_s(x,y,t) \right\}. \tag{1}$$

The evolution of the basement b is mostly governed by two processes: tectonics (both thermal and structural) and flexure. In the present paper we assume that the evolution of b is a data, and we focus on computing the evolution of the function h_s. For

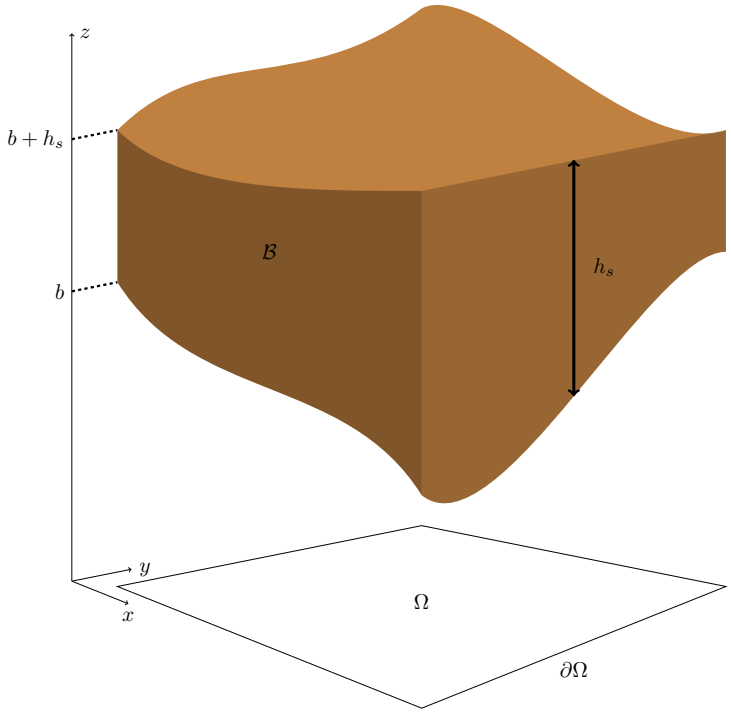

Figure 1. Representation of the two main surfaces considered in a landscape evolution model in the ~~(z~~(x, y, z), ~~Ω)~~ parameter space, where z is the elevation and Ω the spatial domain for (x, y) with boundary $\partial\Omega$. ~~the~~ The basement b surface represents the bottom part of the simulated block, on which sediments are deposited. The topographic surface is $b + h_s$ where h_s is the sediment thickness. The simulated sedimentary content is denoted $\mathcal{B}$.

the sake of clarity, we give the expression of the mass conservation (H2) equations, neglecting porosity for simplicity:

$$\begin{cases} \dfrac{\partial h_s}{\partial t} + div\,(\boldsymbol{J}_s) = S_s & \text{in } \Omega\times]t_0, T[, \\ -\boldsymbol{J}_s \cdot \boldsymbol{n} = B_s & \text{on } \partial\Omega_{\mathcal{N}}\times]t_0, T[, \\ h_s = 0 & \text{on } \partial\Omega_{\mathcal{D}}\times]t_0, T[, \\ h_s(t = t_0) = h_{s,0} & \text{in } \Omega, \end{cases} \tag{2}$$

where S_s and B_s are sediment source terms (coming from an in-situ sediment production, from soil erosion, or from sediment supplies defined in the domain boundaries) and $\boldsymbol{J}_s$ is the sediment flux. The domain boundary $\partial\Omega$ is divided between $\partial\Omega_{\mathcal{N}}$ where ~~Neumann~~ flux (also called Neumann) boundary conditions are imposed and $\partial\Omega_{\mathcal{D}}$ where we enforce ~~homogeneous Dirichlet~~fixed elevation (also called Dirichlet) boundary conditions. Let us precise that in the following the xy coordinates

corresponding to dthe computational domain Ω will be expressed in kilometers (km), while sediment height h_s and basement b will be expressed in meters (m). Choosing a model corresponds to choosing a specific expression for the sediment flux and the source terms. A common feature of almost all LEMs is that the sediment flux model $\boldsymbol{J}_s$ and/or the source term S_s depend non-linearly on the local discharge of water $\mathcal{Q}_w$, very often through a power law like $\mathcal{Q}_w^{r_s}||\nabla(h_s+b)||^{p_s+1}$. Self-amplification mechanisms are known to appear ~~as soon as~~ at least for $r_s > 1$ (**?**). ~~Let us precise that in the following the xy coordinates will be expressed in kilometers (km), while sediment height h_s and basement b will be expressed in meters (m).~~ **??**).

3 ~~From mesh dependent multiple flow direction algorithms to consistent approximations of continuous Gauckler-Manning-Strickler models~~

2.1 The water flow model

Landscape evolution models usually defines the "local discharge of water" $\mathcal{Q}_w$ directly from the so-called drainage or catchment area CA (also ~~sometimes called~~ referred as the contributing area). ~~Roughly speaking CA~~ It corresponds at a given outlet to the measure of the horizontal projection of the surface area from which the water contributing to this outlet is coming from (**???**). Despite being a very intuitive notion, it has evaded for a long time a precise mathematical definition. Classical multiple flow direction (MFD) algorithms are intended to provide a practical way at computing CA for a mesh cell. As is well documented (**????**) the discrete catchment ~~areas~~ area obtained from those algorithms strongly depends on the cell size, geometry and orientation with respect to the flow. Several attempts can be found in the literature to reduce this mesh dependency, defining the water flow discharge as $\mathcal{Q}_w = (CA/w)$, where w is a normalization factor ~~equal for instance to the cartesian cell side length or diagonal length~~ related to a geometric property of the cell (cf **?**) or to an estimate of the ~~width of the flow~~ flow width (**?**) defining the so-called specific or unit catchment area (SCA/UCA). A more modern mathematical definition of the specific catchment area a was proposed in **??**, consisting in solving an abstract uniform flow equation:

$$\left|\begin{array}{ll} -div\left(a\dfrac{\nabla(h_s+b)}{||\nabla(h_s+b)||}\right)=1 & \text{in } \Omega, \\ -a\dfrac{\nabla(h_s+b)}{||\nabla(h_s+b)||}\cdot\boldsymbol{n}=0 & \text{on } \partial\Omega_{in}, \end{array}\right. \tag{3}$$

where $\partial\Omega_{in} = \{\boldsymbol{x} \in \partial\Omega \mid \nabla(h_s+b)\cdot\boldsymbol{n} > 0\}$ is the part of the boundary that is in going and $\boldsymbol{n}$ denotes the outward normal to Ω. Setting $\mathcal{Q}_w = a$, this allows to reduce the mesh dependency to the usual consistency errors of numerical schemes.

~~A mathematical model encompassing the most~~ At first sight, model (**??**) could seem very different from MFD algorithms. However, considering for instance the classical cell-to-cell algorithms of **???**, one can see that those algorithms act as if one was distributing a fictitious water flow of a mesh cell to the neighboring cells with lower elevation proportionally to a function of the slope, as illustrated on figure **??**. One could then legitimately assume that those MFD algorithms could be related to a discretization of some water flow model. This is precisely the idea of **?**, where it was proved that the most classical cell-to-cell MFD algorithms ~~was described in ?where it is established that those algorithms coincide with a solver for a well chosen~~

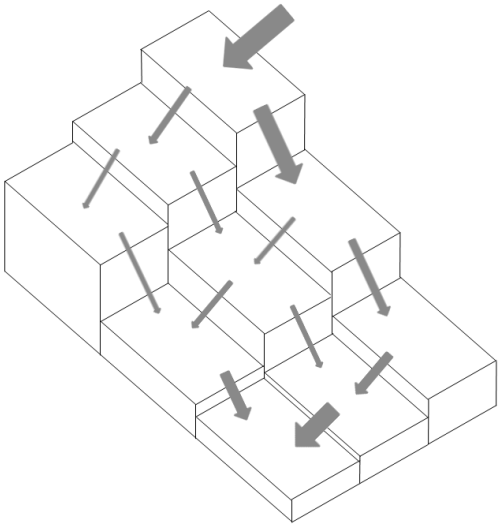

Figure 2. Basic principle of the simplest cell-to-cell MFD algorithm: water is distributed to lower neighboring cells proportionally to the slope (reproduced from **?**)

~~discretization of~~ are finally simply a way of implementing a solver for the following stationary water mass conservation with Gauckler-Manning-Strickler ~~flux model for~~ (GMS) flux modeling surface runoff:

$$\left| \begin{array}{ll} -div\left(k_m h_w \eta_w(h_w) s_{ref}^{-p_w} ||\nabla(h_s+b)||^{p_w} \nabla(h_s+b)\right) = S_w & \text{in } \Omega, \\ -k_m h_w \eta_w(h_w) s_{ref}^{-p_w} ||\nabla(h_s+b)||^{p_w} \nabla(h_s+b) \cdot n = 0 & \text{on } \partial\Omega_{in}, \end{array} \right. \tag{4}$$

where h_w is the water height, s_{ref}= 1 m.km^{-1} the reference slope, p_w a model parameter and η_w the water mobility function. For simplicity we assume here that the mobility function has no dimension, and that the source S_w is given in m^3.s^{-1}km^{-2} such that its integral over a 2d area measured in km^2 coincides with a discharge in m^3.s^{-1}. The coefficient ~~k_m~~ k_m can be though of as the Strickler coefficient or the inverse of the Gauckler-Manning coefficient up to a change of unit (strictly speaking, this identification is trully valid for channels and if the mobility function η_w is equal to a dimensionless hydraulic radius). For this choice of source, k_m has the unit m.s^{-1} of a speed. ~~Steady state analysis (??) for channels suggests to use values $\eta_w(h_w) = (h_w/h_{ref})^{1/2}$ and $p_w = -1/2$, while the classical Gauckler-Manning-Strickler formula would coincide with $\eta_w(h_w) = (R_h(h_w)/h_{ref})^{2/3}$~~ Comparing (**??**) with ~~$R_h(h_w)$ the hydraulic radius and again $p_w = -1/2$. However the hypothesis underlying those results is tailored to channel flows, which is probably not valid over the wide range of flow configurations occurring at the large time and space scales of landscape evolution models.For this reason, we prefer to not fix precise values for η_w and p_w and think of them as modeling parameters that can be tuned for each considered problem.~~ (**??**), we see that (**??**) corresponds to the particular case where $k_m = 1$, $p_w = -1$ and $a = h_w \eta_w(h_w)$. In this sense the GMS model (**??**) is a generalization of (**??**) that allows to include the classical ingredients (non linear slope dependency and some spatial heterogeneity) of the MFD algorithms family.

The analysis of **?** ~~allows to give a general definition of~~ explains how the catchment area ~~: for an open set $\mathcal{O} \subset \mathbb{R}^2$, the catchment area for the outlet of~~ $CA(\mathcal{O})$ for the outlet of a region $\mathcal{O}$ ~~is defined by~~ that is computed by MFD algorithms coincides with an intermediate discrete quantity appearing in the most natural discrete solver for (**??**). It also allows to give a continuous interpretation of the $CA(\mathcal{O})$ that is computed by MFD algorithms:

~~$$CA(\mathcal{O}) = \widetilde{q}_{\mathcal{O}}^{ex} = \int_{\partial\mathcal{O}} h_w \eta_w(h_w) \left(-k_m s_{ref}^{-p_w} ||\nabla(h_s+b)||^{p_w} \nabla(h_s+b)\cdot \boldsymbol{n}\right)^+,$$~~

$$CA(\mathcal{O}) = \int_{\partial\mathcal{O}} h_w \eta_w(h_w) \left(-k_m s_{ref}^{-p_w} ||\nabla(h_s+b)||^{p_w} \nabla(h_s+b)\cdot \boldsymbol{n}\right)^+, \tag{5}$$

where h_w is the solution of (**??**) with $S_w = 1$ and ~~$v^+ = \max(0, v)$. We~~ where we have denoted v^+ the positive part of v (i.e. $v^+ = max(0, v)$). Since model (**??**) describes a water flow, we recover that thanks to **?** we can reinterpret the catchment are $CA(\mathcal{O})$ computed through the classical cell-to-cell MFD algorithms the total flux leaving $\mathcal{O}$ of a fictitious water flow with a uniform water source $S_w = 1$. Unfortunately, we also see that $CA(\mathcal{O})$ strongly depends on the geometry of $\mathcal{O}$ and its orientation with respect to the flow. In particular~~if we take for $\mathcal{O}$ a cell of the mesh we understand why the MFD algorithms produce mesh dependent catchment areas~~, it is detailed in **?** that cell-to-cell MFD computations will compute in practice the catchment area $CA(\mathcal{K})$ for each cell K of a mesh through a discretized version of (**??**) for $\mathcal{O} = K$. Thus, when MFD algorithms are considering this expression of (**??**) to estimate the "local discharge of water" $\mathcal{Q}_w$, it produces cell and thus mesh dependency in the simulated surface water distribution. In line with the attempts of **?** or **?** to define a ~~unit~~ specific catchment area (~~UCA~~SCA) by rescaling the CA, ~~it is clear that~~ the correct scaling would be to set the normalization factor w to the length of the portion of $\partial\mathcal{O}$ ~~such that $\left(-k_m s_{ref}^{-p_w} ||\nabla(h_s+b)||^{p_w} \nabla(h_s+b)\cdot \boldsymbol{n}\right)^+ > 0$, which depending on the orientation of the flow will sometimes match the choices of **?** or **??** explaining their partial success. Thus a~~ along which the fictitious water flow is leaving $\mathcal{O}$. A corrected definition of the ~~unit catchment int~~ specific catchment in the spirit of **???** area would thus be to use:

~~$$UCA(\mathcal{O}) = \frac{1}{\int_{\partial\mathcal{O}} \chi_{-k_m s_{ref}^{-p_w} ||\nabla(h_s+b)||^{p_w} \nabla(h_s+b)\cdot\boldsymbol{n}>0}} \int_{\partial\mathcal{O}} h_w \eta_w(h_w) \left(-k_m s_{ref}^{-p_w} ||\nabla(h_s+b)||^{p_w} \nabla(h_s+b)\cdot \boldsymbol{n}\right)^+,$$~~

$$SCA(\mathcal{O}) = \frac{1}{\int_{\partial\mathcal{O}} \chi_{-k_m s_{ref}^{-p_w} ||\nabla(h_s+b)||^{p_w} \nabla(h_s+b)\cdot\boldsymbol{n}>0}} \int_{\partial\mathcal{O}} h_w \eta_w(h_w) \left(-k_m s_{ref}^{-p_w} ||\nabla(h_s+b)||^{p_w} \nabla(h_s+b)\cdot \boldsymbol{n}\right)^+, \tag{6}$$

where χ is the indicator function (i.e. the function with value 1 when the condition is satisfied and 0 otherwise). ~~This~~ Depending on the orientation of the flow, such a normalization will sometimes match the choices of **?** or **??** explaining their partial success. This SCA scales as an approximation of the continuous water flux magnitude ~~$q_w = |k_m h_w \eta_w(h_w)| s_{ref}^{-p_w} ||\nabla(h_s+b)||^{p_w+1}$~~:

$$q_w = |k_m h_w \eta_w(h_w)| s_{ref}^{-p_w} ||\nabla(h_s+b)||^{p_w+1}, \tag{7}$$

(in $m^3s^{-1}km^{-1}$) but is not equal to it~~, and~~. The SCA defined by (**??**) is in fact a mean of q_w along the outflow portion of $\partial\mathcal{O}$, and thus still retains some dependency in the geometry of $\mathcal{O}$ and its orientation with respect to the flow. ~~In this context it is more natural to use directly $\mathcal{Q}_w = q_w$ such that the erosion in depends on the local water flux magnitude and the slope. Comparing with~~ Meanwhile, notice that the specific catchment area a of model (**??**) ~~, we see that corresponds to the particular case where one chooses~~ can be reinterpreted through (**??**) as computing q_w since:

$$q_w = |k_m h_w \eta_w(h_w)|\, s_{ref}^{-p_w} ||\nabla(h_s + b)||^{p_w+1} = |a|\ ||\nabla(h_s + b)||^{-1+1} = a,$$

as we have set $a = h_w\eta_w(h_w) \geq 0$, $p_w = -1$, $k_m = 1$ and ~~$p_w = -1$ leading to $a = h_w\eta_w(h_w)$. Thus~~as was already explained in **?**, using ~~$\mathcal{Q}_w = a$ relates the erosion to (a power of) the water height and~~ $s_{ref} = 1$ to merge (**??**) inside (**??**). Thus, in view of the ~~slope. Both choices have pros and cons, however the choice $\mathcal{Q}_w = q_w$ seems more general to us. The results of **?** explain why such a strong mesh dependency resisting mesh refinement was observed in the geological literature for the CA obtained from~~ success of **?** and within the context of (**??**) it seems very natural to set $\mathcal{Q}_w = q_w$. One could consider that the equivalence between classical cell-to-cell MFD algorithms ~~. It also explains how to compute a correct approximation~~ established in **?** and the consistency correction proposed there that leads to consider using a discrete version of q_w ~~from the obtained CA which is the main objective of this section. We consequently start by recalling the results of **?** for cell-to-cell MFD in a slightly more general setting and to compute the sought approximation~~ is another path to recover the conclusions of (**??**) and in this sense that q_w is a generalization of a to more complex water flow models.

The consistency correction proposed in **?** for MFD algorithms precisely coincides precisely with the replacement of the computation of $CA(K)$ or $SCA(K)$ for a mesh cell K by a consistent discrete reconstruction q_K of q_w in each cell K. ~~As node-to-node MFD algorithms are the core of many legacy codes, to offer a more straightforward application of the results of **?**for such implementations we next detail how the most classical node-to-node MFD algorithmsalso enter this framework, suffer from the same deficiencies and how to correct them in the same way than for the cell-to-cell case that was already explored in **?**. Notice that~~ Convergence of this discrete version q_K to q_w when the mesh size goes to zero was proved in **?**, along with error estimates. Thus, apart from the usual discretization error no anomalous mesh dependency should remain in q_K in practice, contrary to what is observed for $SCA(K)$ given by MFD algorithms. In this sense, q_K can be seen as consistency correction for $SCA(K)$, as well as a generalization of (**??**) to a richer family of flow models. The interpretation of the local water discharge $\mathcal{Q}_w$ as being equal to the water flux magnitude q_w given by (**??**) from the solution of (**??**) is therefore the default configuration chosen in the water flow model used to perform all the simulations we introduce in this paper.

This water flow model is therefore physically justified by the GMS model. Its application domain is however not necessarily restricted to channels. It depends in fact to the specific choice made on the model parameter values. Steady state analysis (**??**) for channels suggests to use values $\eta_w(h_w) = (h_w/h_{ref})^{1/2}$ and $p_w = -1/2$, while the classical Gauckler-Manning-Strickler formula would coincide with $\eta_w(h_w) = (R_h(h_w)/h_{ref})^{2/3}$ with $R_h(h_w)$ the hydraulic radius and again $p_w = -1/2$. When applied to large time and space scales landscape evolution models, these calibrations are no more valid and at this stage we suggest to consider η_w and p_w as modeling parameters that can be tuned for each considered problem. In the following

numerical experiments, since we only consider the water fluw q_w the choice of the water mobility function as no influence and we set $\eta_w(h_w) = 1$ for simplicity, as well as $p_w = 0$. Notice that our conclusions would remain valid for more general choices of those parameters. The application domain is however limited by an additional mathematical condition. Notice that systems (**??**) and (**??**) are in fact stationary transport problems for a or h_w, which are rigorously speaking well-posed ~~from the mathematical point of view if~~ if the topography satisfies a sufficient condition. In particular conditions:

$$-\Delta(h_s + b) > 0 \quad \text{or} \quad -div\left(k_m s_{ref}^{-p_w} ||\nabla(h_s + b)||^{p_w} \nabla(h_s + b)\right) \geq 0, \tag{8}$$

~~(or quite equivalently $-div\left(k_m s_{ref}^{-p_w} ||\nabla(h_s + b)||^{p_w} \nabla(h_s + b)\right) > 0$), i.e. roughly speaking if there are no~~ ensures that model (**??**) is well-posed, which corresponds to prohibiting water accumulation areas ~~or~~ and flat areas (see **??????**). ~~This essentially implies that the flow model~~ Model (**??**) ~~is well justified for drainage basin only. If it used with topographies that do not fulfill , a modeling error can appear, ruining our efforts to achieve consistency. This assumption limits the domain of application of the model, and can be considered~~ being in fact a simplification of the shallow water equation (see section section **??**), this limitation can be seen as the price to pay ~~for a low computational cost strategy. Model being in fact a simplification of the shallow water equation, if extending the computation time is allowed~~ to simulate the water flow mass conservation with a very low computational expense. At the cost of a higher computational time alternative models also derived from the shallow water equation can be considered to overcome this limitation ~~. This will be discussed in section **??**~~(see section **??**).

2.2 ~~Mesh descriptionLet Ω be a bounded polyhedral connected domain of $\mathbb{R}^2$, whose boundary is denoted $\partial\Omega = \overline{\Omega} \setminus \Omega$. We recall the usual finite volume notations describing a mesh $\mathcal{M} = (\mathcal{T}, \mathcal{F})$ of Ω. The set of the cells of the mesh $\mathcal{T}$ is a finite family of connected open disjoint polygonal subsets of Ω, such that $\overline{\Omega} = \cup_{K \in \mathcal{T}} \overline{K}$. For any $K \in \mathcal{T}$, we denote by $|K|$ the measure of $|K|$, by $\partial K = \overline{K} \setminus K$ the boundary of K, by ρ_K its diameter and by x_K its barycenter. The set of faces of the mesh $\mathcal{F}$ is a finite family of disjoint subsets of $\mathbb{R}^2$ included in $\overline{\Omega}$ such that, for all $\sigma \in \mathcal{F}$, its measure is denoted $|\sigma|$, its diameter h_σ and its barycenter x_σ . For any $K \in \mathcal{T}$, the faces of cells K corresponds to the subset $\mathcal{F}_K$ of $\mathcal{F}$ such that $\partial K = \cup_{\sigma \in \mathcal{F}_K} \overline{\sigma}$. Then, for any face $\sigma \in \mathcal{F}$, we denote by $\mathcal{T}_\sigma = \{K \in \mathcal{T} \mid \sigma \in \mathcal{F}_K\}$ the cells of which σ is a face. Next, for all cell $K \in \mathcal{T}$ and all face $\sigma \in \mathcal{F}_K$ of cell K, we denote by $n_{K,\sigma}$ the unit normal vector to σ outward to K, and $d_{K,\sigma} = |x_\sigma - x_K|$. The set of boundary faces is denoted $\mathcal{F}_{ext}$, while interior faces are denoted $\mathcal{F}_{int}$. Finally for any $\sigma \in \mathcal{F}_{int}$, whenever the context is clear we will denote by K and L the two cells forming $\mathcal{T}_\sigma = \{K, L\}$, as well as $d_{KL} = |x_K - x_L|$. This for instance allows when looping over the faces σ of cell K todenote by L the other face of σ without resorting to a too heavy notation. To avoid any confusion with water and~~ The sediment ~~heights, $\epsilon = \max_{K \in \mathcal{T}} \rho_K$ will denote the mesh size. For any continuous quantity u, its discrete counterpart will be denoted $u_\mathcal{T} = ((u_K)_{K \in \mathcal{T}}, (u_\sigma)_{\sigma \in \mathcal{F}_{ext}})$ where for any $K \in \mathcal{T}$ u_K is the constant approximation of u in cell K while for any $\sigma \in \mathcal{F}_{ext}$ u_σ is the constant approximation of u over face σ.In the following we will assume that the mesh is orthogonal, i. e. there exists a family of centroids $(\overline{x}_K)_{K \in \mathcal{T}}$ such that:~~ flux model

In the present paper we have chosen to focus on the stratigraphic model that has already been discussed in detail in **????**, and which is a generalization of the models studied in **??**. The corresponding sediment flux $\boldsymbol{J}_s$ takes the following form:

$$\overline{\boldsymbol{x}}_K \in K \quad \forall K \in \mathcal{T} \quad \text{and} \quad \frac{\overline{\boldsymbol{x}}_L - \overline{\boldsymbol{x}}_K}{|\overline{\boldsymbol{x}}_L - \overline{\boldsymbol{x}}_K|} = \boldsymbol{n}_{K,\sigma} \quad \text{for} \quad \sigma \in \mathcal{F}_{int},\ \sigma = \{K, L\}$$

$$\boldsymbol{J}_s = -\eta_s(h_s) s_{ref}^{-p_s} ||\nabla(h_s + b)||^{p_s} \left(\left(\frac{q_w}{q_{ref}} \right)^{r_s} \nabla\psi_w(h_s + b) + \nabla\psi_g(h_s + b) \right) \quad \text{in } \Omega\times]t_0, T[, \tag{9}$$

~~and let us denote $\overline{\boldsymbol{x}}_\sigma$ the orthogonal projection of $\overline{\boldsymbol{x}}_K$ to the hyperplane containing σ for any $\sigma \in \mathcal{F}_K$ and any $K \in \mathcal{T}$ with $\overline{d}_{K,\sigma} = |\overline{\boldsymbol{x}}_K - \overline{\boldsymbol{x}}_\sigma|$, as well as $\overline{d}_{KL} = |\overline{\boldsymbol{x}}_K - \overline{\boldsymbol{x}}_L|$. Then, one can use a two-point finite volume scheme to discretize diffusion operators with scalar diffusion coefficients (no tensors).~~

2.3 ~~The cell-to-cell multiple flow direction algorithm and its link with Gauckler-Manning-Strickler models~~

~~As mentioned above, the results of this subsection are mostly reproduced from **?**. As a consequence, no true originality is claimed here however we believe that the node-to-node version will be easier to understand after this reminder.The starting point of a finite volume discretization is to integrate equation over each cell K:~~

$$-\int_K div\left(k_m h_w \eta_w(h_w) s_{ref}^{-p_w} ||\nabla(h_s + b)||^{p_w} \nabla(h_s + b)\right) = \int_K S_w.$$

~~Denoting $S_{w,K} = \frac{1}{|K|}\int_K S_w$ and using Stokes' formula, this leads to:~~

$$-\sum_{\sigma\in\mathcal{F}_K} \int_\sigma k_m h_w \eta_w(h_w) s_{ref}^{-p_w} ||\nabla(h_s + b)||^{p_w} \nabla(h_s + b)\cdot\boldsymbol{n}_{K,\sigma} = |K| S_{w,K}.$$

~~Choosing a finite volume scheme then simply amounts to choosing how to approximate each term appearing in the face integrals.The most natural~~ where $r_s > 0$ and ~~classical finite volume scheme consists in choosing constant approximate values $k_{m,\sigma}$~~ $p_s > 0$ are model parameters, q_w is the water flux obtained from (**??**), q_{ref} and ~~$\boldsymbol{G}_{s,\sigma}$ for k_m~~ s_{ref} are dimensional factors, and ~~$||\nabla(h_s + b)||^{pw}$ along each face σ and to use an upwind scheme $h_{w,\sigma}^{up}$ for the true unknown $h_w \eta_w(h_w)$~~ η_s is a dimensionless sediment mobility function such that:

$$-\int_\sigma k_m h_w \eta_w(h_w) s_{ref}^{-p_w} ||\nabla(h_s + b)||^{p_w} \nabla(h_s + b)\cdot\boldsymbol{n} \approx -k_{m,\sigma} s_{ref}^{-p_w} ||\boldsymbol{G}_{s,\sigma}||^{p_w} h_{w,\sigma}^{up} \int_\sigma \nabla(h_s + b)\cdot\boldsymbol{n}.$$

$$0 \le \eta_s(u) \le 1 \quad \text{and} \quad \eta_s(0) = 0, \tag{10}$$

~~Finally, thanks to our hypothesis on mesh orthogonality we can use the two-point flux approximation to compute $\int_\sigma \nabla(h_s + b)\cdot\boldsymbol{n}$.The TPFA consists in noticing that for a linear function $h_s + b$, the gradient being constant and satisfying $\nabla(h_s + b)\cdot\boldsymbol{n}_{K,\sigma} = \frac{1}{d_{KL}}((h_s + b)(\boldsymbol{x}_L)$~~

~~the following formula:~~ whose main role is to ensure that the sediment height h_s remains positive. In the following we use:

$$-\int_\sigma \nabla(h_s+b)\cdot\boldsymbol{n} = -\nabla(h_s+b)\cdot\int_\sigma \boldsymbol{n} = \frac{|\sigma|}{\bar{d}_{KL}}((h_s+b)(\boldsymbol{x}_K)-(h_s+b)(\boldsymbol{x}_L)),$$

$$\eta_s(u) = \begin{cases} 1-\dfrac{h_c}{u+h_c} & \text{if } u \geq 0, \\ 0 & \text{otherwise} \end{cases} \tag{11}$$

~~is exact since $\frac{1}{\bar{d}_{KL}}(\boldsymbol{x}_L-\boldsymbol{x}_K)=\boldsymbol{n}_{K,\sigma}$ and will thus be a first order approximation of the flux. More precisely, denoting $h_{w,K}$ for any $K\in\mathcal{T}$ the discrete water height value associated to cell K, if one further assumes that $h_{s,\sigma}+b_\sigma = h_{s,K}+b_K$ for any $\sigma\in\mathcal{F}_{ext}$ and $K\in\mathcal{T}_\sigma$ which is generally what is done in practical applications of the MFD algorithm, for any $K\in\mathcal{T}$ the proposed finite volume scheme rewrites:~~

$$\sum_{\sigma\in\mathcal{F}_K\cap\mathcal{F}_{int}} \tau_{KL} h_{w,\sigma}^{up}\,(h_{s,K}+b_K-h_{s,L}-b_L) = |K|S_{w,K},$$

~~where the upwind value is given by $h_{up}^{w,\sigma}=h_{w,K}\eta_w(h_{w,K})$ if $h_{s,K}+b_K \geq h_{s,L}+b_L$~~ with h_c a parameter. The function with subscript w is intended to model the water driven processes, while the function with subscript g models gravity related processes. We consider here the most common form for functions ψ_w and ~~$h_{up}^{w,\sigma}=h_{w,L}\eta_w(h_{w,L})$ if $h_{s,K}+b_K<h_{s,L}+b_L$, the transmissivity τ_{KL} is given by:~~ ψ_g corresponding to:

$$\tau_{KL} = \frac{|\sigma|k_{m,\sigma}}{\bar{d}_{KL}s_{ref}^{-p_w}}||\boldsymbol{G}_{s,\sigma}||^{p_w},$$

$$\psi_w(u)=\int_0^u k_w(v)dv \quad \text{and} \quad \psi_g(u)=\int_0^u k_g(v)dv, \tag{12}$$

~~and where $\boldsymbol{G}_{s,\sigma}=\frac{1}{2}(\boldsymbol{G}_{s,K}+\boldsymbol{G}_{s,L})$ and $\boldsymbol{G}_{s,K}$ is a discrete reconstruction of the gradient of h_s+b in cell K. To derive it, we use:~~ where k_w and k_g are diffusion coefficients such that:

$$\mathbb{I}_d = \sum_{\sigma\in\mathcal{F}_K} |\sigma|(\boldsymbol{x}_\sigma-\boldsymbol{x}_K)\boldsymbol{n}_{K,\sigma},$$

$$0\leq k_g^- \leq k_g(u) \leq k_g^+ < +\infty \quad \text{and} \quad 0\leq k_w^- \leq k_w(u) \leq k_w^+ < +\infty, \tag{13}$$

~~leading to~~ in such a way that:

$$\boldsymbol{G}_{s,K} = \sum_{\sigma\in\mathcal{F}_K} |\sigma|\boldsymbol{G}_{s,K}\cdot\boldsymbol{n}_{K,\sigma}(\boldsymbol{x}_\sigma-\boldsymbol{x}_K),$$

$$\nabla\psi_w(h_s+b)=k_w(h_s+b)\nabla(h_s+b) \quad \text{and} \quad \nabla\psi_g(h_s+b)=k_g(h_s+b)\nabla(h_s+b), \tag{14}$$

~~and thus on the orthogonal meshes we consider here as by consistency $|\sigma|\boldsymbol{G}_{s,K}\cdot\boldsymbol{n}_{K,\sigma}\approx\int_\sigma\nabla(h_s+b)\cdot\boldsymbol{n}_{K,\sigma}$, $\boldsymbol{G}_{s,K}$ is naturally given by:~~

$$\boldsymbol{G}_{s,K}=\frac{1}{|K|}\sum_{\sigma\in\mathcal{F}_K\cap\mathcal{F}_{int}}\frac{|\sigma|}{\overline{d}_{KL}}(h_{s,L}+b_L-h_{s,K}-b_K)(\boldsymbol{x}_\sigma-\boldsymbol{x}_K)$$

$$+\frac{1}{|K|}\sum_{\sigma\in\mathcal{F}_K\cap\mathcal{F}_{ext}}\frac{|\sigma|}{\overline{d}_{K\sigma}}(h_{s,\sigma}+b_\sigma-h_{s,K}-b_K)(\boldsymbol{x}_\sigma-\boldsymbol{x}_K).$$

~~From the mathematical point of view, a natural choice for the face value $k_{m,\sigma}$ is the harmonic mean:~~

$$k_{m,\sigma}=\frac{\overline{d}_{KL}k_{m,K}k_{m,L}}{k_{m,K}\overline{d}_{L,\sigma}+k_{m,L}\overline{d}_{K,\sigma}} \quad \text{with for instance} \quad k_{m,K}=\frac{1}{|K|}\int_K k_m \ \forall K\in\mathcal{T},$$

~~but many other choices are possible. Let us now recall the elementary proof given in **?**: gathering the faces by upwinding kind,~~ so that the sediment flux follows the topographic slope $\nabla(h_s+b)$.

This sediment flux model is implemented in our modeling platform ArcaDES (**?**), and all the simulations shown in the following sections are performed using the ArcaDES platform (although ArcaDES is mentioned for the first time in a scientific paper, it is used since 2015 in the stratigraphic numerical forward model DionisosFlow™ initially developed by **?**). Both soil erosion and sediment deposition are considered. As ArcaDES is tailored for large time and space scales simulations, this is the reason why we have chosen to express the xy coordinates in kilometers (km), time in million years (My), sediment height h_s and basement b in meters (m). Thus the unit of sediment sources will be meters per million years (m.My^{-1}). Since we have chosen to use $\mathcal{Q}_w=q_w$ with q_w the water flux from (**??**), the unit for the water discharge q_w is m^3.s^{-1}.km^{-1} and thus we naturally set q_{ref}= 1 m^3.s^{-1}.km^{-1}. The natural unit of coefficients k_g and k_w is km^2.My^{-1}, with the reference slope again set to s_{ref}= 1 m.km^{-1}.

2.3 Some insights from perturbation theory

In this subsection, in order to give a feeling of the potential stability issues related to model (**??**)-(**??**)-(**??**), we will perform a brief analysis of the behavior of solutions under perturbations. We assume for simplicity that k_g and k_w are constant functions. Let us denote $(h_{s,*},h_{w,*})$ a reference solution of (**??**)-(**??**)-(**??**) with sources $(S_{s,*},S_{w,*})$, whose stability is to be tested. We denote $(h_{s,\delta},h_{w,\delta})$ a perturbation of magnitude δ of this reference solution with perturbed source $(S_{s,*}+S_{s,\delta},S_{w,*}+S_{w,\delta})$ and consider the evolution of $(h_s,h_w)=(h_{s,*}+h_{s,\delta},h_{w,*}+h_{w,\delta})$. Since both the perturbed and unperturbed solutions have to satisfy the boundary conditions, we deduce that the perturbation $(h_{s,\delta},h_{w,\delta})$ itself also satisfies the same boundary conditions. Then in line with for instance the analysis of **?**, injecting (h_s,h_w) into (**??**)-(**??**), multiplying by $h_{s,\delta}$ and integrating by parts

we get:

$$\sum_{\sigma\in\mathcal{F}_K\cap\mathcal{F}_{int},h_{s,K}+b_K\geq h_{s,L}+b_L}\tau_{KL}\frac{d}{dt}\left(\frac{1}{2}\int_\Omega h_{w,K}s_{s,\delta}^2\right)=-\int_\Omega \eta_w s(h_{w,K}s)s_{ref}^{-p_s}||\nabla(h_{s,K}s+b_K-h_{s,L}-b_L)||^{p_s}\left(\left(\frac{q_w}{q_{ref}}\right)^{r_s}k_w+k_g\right)$$

$$\sum_{\sigma\in\mathcal{F}_K\cap\mathcal{F}_{int},b_K<b_L}\tau_{KL}h_{w,L}\eta_w(h_{w,L})\left(h_{s,L}+b_L-h_{s,K}-b_K\right)=|K|S_{w,K}.$$

$$+\int_\Omega \eta_s(h_{s,*})s_{ref}^{-p_s}||\nabla(h_{s,*}+b)||^{p_s}\left(\left(\frac{q_{w,*}}{q_{ref}}\right)^{r_s}k_w+k_g\right)\nabla(h_{s,*}+b)\cdot\nabla h_{s,\delta}$$

Setting

$$-\int_\Omega \eta_s(h_s)s_K=\sum_{\sigma\in\mathcal{F}_K\cap\mathcal{F}_{int},h_{s,K}+b_K\geq h_{s,L}+b_L}\tau_{KL}s_{ref}^{-p_s}||\nabla(h_{s,K}s+b_K-h_{s,L}-b_L)||^{p_s}\left(\left(\frac{q_w}{q_{ref}}\right)^{r_s}k_w+k_g\right)\nabla(h_{s,*}+b)\cdot\nabla h_{s,\delta}+\int_\Omega$$

and noticing that $s_L>0$ as soon as there exists $\sigma\in\mathcal{F}_L\cap\mathcal{F}_{int}$ such that $b_L>b_K$, we see that equation can be rewrittenDenoting:

$$s_K h_{w,K}\eta_w j_s(h_{w,K}u,v,w)-\sum_{\sigma\in\mathcal{F}_K\cap\mathcal{F}_{int},b_K<b_L}\tau_{KL}h_{w,L}=\eta_w s(h_{w,L}u)s_{ref}^{-p_s}||\nabla v||^{p_s}\left(h_{s,L}\left(\frac{w}{q_{ref}}\right)^{r_s}k_w+b_L-h_{s,K}-b_K k_g\right)=|K|S$$

Defining the water outflux by $\widetilde{q}_K=s_K h_{w,K}\eta_w(h_{w,K})$, we thus obtain we obtain the equation governing the evolution of the perturbation's total energy:

$$\widetilde{q}_K-\sum_{\sigma\in\mathcal{F}_K\cap\mathcal{F}_{int},h_{s,K}+b_K<h_{s,L}+b_L}\tau_{KL}\frac{\widetilde{q}_L}{s_L}\left(h_{s,L}+b_L-h_{s,K}-b_K\right)=|K|S_{w,K}.$$

$$\frac{d}{dt}\left(\frac{1}{2}\int_\Omega h_{s,\delta}^2\right)=-\int_\Omega j_s(h_s,h_s+b,q_w)||\nabla h_{s,\delta}||^2+\int_\Omega S_{s,\delta}h_{s,\delta}$$

Basic principle of the simplest cell-to-cell MFD algorithm: water is distributed to lower neighbouring cells proportionally to the slope (reproduced from **?**) The cell-to-cell MFD algorithm admits a reformulation as a linear system first mentioned by **?** although without exhibiting an explicit formula. In **?**, it is established that linear system underlying the cell-to-cell MFD algorithm illustrated on Fig. **??** is equivalent to solving for $k_m=1$ and $p_w=0$ using a lower triangular solver and a cell ordering based on decreasing topography. Indeed the algorithm illustrated Fig. **??** consists in distributing the total outflow $\widetilde{q}_K$ of cell K along the neighbouring cells of K with lower altitude altitude proportionally to the ratio s_{KL}/s_K of the discrete slope s_{KL} between the high cell K and the low cell L regarding the total positive slope s_K of the high cell K. It is then easy to observe that the formula corresponds to reversing this idea, expressing how the inflow received by the low cell K is computed from the outflow of its higher neighbours.From this equivalence between the classical MFD and the two-point flux

approximation (TPFA) of the classical Gauckler-Manning-Strickler model, a crucial observation of ? is that the usual unknown $\widetilde{q}_K$ of the MFD algorithm that corresponds to the CA of cell K in the case $S_w = 1$ is not the good quantity to represent the water flux magnitude. Indeed, from $\widetilde{q}_K = s_K h_{w,K} \eta_w(h_{w,K})$ and the consistency of the two-point formula we see that it approximates as announced:

$$\widetilde{q}_K \approx \widetilde{q}_K^{ex} = \sum_{\sigma \in \mathcal{F}_K} \int_\sigma h_w \eta_w(h_w) \left(-k_m s_{ref}^{-p_w} ||\nabla(h_s + b)||^{p_w} \nabla(h_s + b) \cdot \boldsymbol{n}_{K,\sigma} \right)^+.$$

$$+ \int_\Omega \left(j_s(h_{s,*}, h_{s,*} + b, q_{w,*}) - j_s(h_s, h_s + b, q_w) \right) \nabla(h_{s,*} + b) \cdot \nabla h_{s,\delta}. \tag{15}$$

As explained in ? the quantity $\widetilde{q}_K$ approximates the outflux of a cell which thanks to the equivalence with a discretization of a Gauckler-Manning-Strickler model we can easily identify as a mesh dependent quantity. Thus, the only convergence that can be expected for $\widetilde{q}_K$ is to zero. As explained in the introductory part of this section we could normalize it by the portion of ∂K along which the flow is outgoing but this is highly impractical and still prone to some mesh dependency depending on the cell orientation with respect to the flux. To effectively compute an accurate discrete water flux magnitude q_K for each cell $K \in \mathcal{T}$, from ? we know that we can reconstruct cellwise the water flux vector using by setting: The first term of the right hand side is always negative and thus always contributes to the stability of the system. The second term describes the contribution to the evolution of the sediment perturbation's energy of potential pertubation sources other that the initial conditions. The last term:

$$\boldsymbol{Q}_K = \sum_{\sigma \in \mathcal{F}_K \cap \mathcal{F}_{int}, h_{s,K} + b_K > h_{s,L} + b_L} \frac{\tau_{KL} \widetilde{q}_K}{|K| s_K} (h_{s,K} + b_K - h_{s,L} - b_L)(\boldsymbol{x}_\sigma - \boldsymbol{x}_K) -$$

$$A_\delta = \int_\Omega \left(j_s(h_{s,*}, h_{s,*} + b, q_{w,*}) - j_s(h_s, h_s + b, q_w) \right) \nabla(h_{s,*} + b) \cdot \nabla h_{s,\delta}, \tag{16}$$

$$\sum_{\sigma \in \mathcal{F}_K \cap \mathcal{F}_{int}, h_{s,K} + b_K < h_{s,L} + b_L} \frac{\tau_{KL} \widetilde{q}_L}{|K| s_L} (h_{s,L} + b_L - h_{s,K} - b_K)(\boldsymbol{x}_\sigma - \boldsymbol{x}_K),$$

and simply deduce a consistent water flux magnitude by setting $q_K = ||\boldsymbol{Q}_K||$. This consistent water flux magnitude is mesh independent in the usual numerical analysis sense: it converges to the continuous flux when the mesh size ε goes to zero, contrary to $\widetilde{q}_K$. The use of $\widetilde{q}_K$ or its normalized versions instead of q_K in the geological literature is originates partially from the non-linearity of the main reason why such a strong mesh dependency was observed, without any significant improvement with mesh refinement. Instead, the convergence of the consistent water flux magnitude q_K was rigorously established and illustrated in ?, up to providing error estimates. Thus, it is important to use q_K sediment transport model but most importantly from the coupling between the flow and the sediment transport. If A_δ is negative or if it is small enough and if the perturbation source is also small enough, then the sediment perturbation energy will decrease with time. In this case, the solution $(h_{s,*}, h_{w,*})$

is said to be stable under perturbation $(h_{s,\delta}, h_{w,\delta})$. However the sign of A_δ is not always negative and will often take non necessarily small positive values. If A_δ is large enough, instead of ~~$\widetilde{q}_K$ when coupling with sediment evolution models i.e. using $\mathcal{Q}_w = q_w$ in and not $\widetilde{q}_K$. From the flow routing literature perspective and by virtue of , q_K can certainly be considered as a post-processing consistency correction of $\widetilde{q}_K$, easy to implement in legacy softwares.~~ being diffused by the first term the sediment perturbation energy will grow with time and potentially become as large as the unperturbed solution: the solution $(h_{s,*}, h_{w,*})$ is then unstable under perturbation $(h_{s,\delta}, h_{w,\delta})$. This is a self-amplification mechanism, as the magnitude of A_δ will grow with the perturbation's magnitude and cancel if the perturbation if zero, and also because of the dependency of the water flux $q_{w,\delta}$ on the topography perturbation $h_{s,\delta}$. We will say that growing perturbations correspond to the physically unstable regime.

~~The MFD formulation allows in turn some interesting observations for the Gauckler-Manning-Strickler model: it is indeed clear that the choice of the water mobility function η_w has no influence on the water flux strength q_w, as it appears nowhere in and . In the same way, only the contrasts of the coefficient k_m will impact q_w, as only ratios τ_{KL}/s_K are appearing in and .~~

2.4 ~~The classical node-to-node MFD/SFD algorithms interpreted as discrete Gauckler-Manning-Strickler solvers~~

~~In this subsection, we will explain how to reinterpret the most classical node-to-node flow routing algorithms as attempts to discretize a continuous Gauckler-Manning-Strickler model. Such an explicit interpretation seems to be absent from the literature, so at least to the author's knowledge the results of this subsection are quite new. To this end, for simplicity we restrict ourselves in this section to uniform cartesian meshes, and we adopt the usual cartesian index (i,j) notation for designating its nodes (see Fig. **??**) as well as Δx~~ We can anticipate that the relative magnitude of the gravity and water coefficients k_g and ~~Δy for the cartesian cell side lengths. This is by no means a restriction but simply a more convenient way to explain how to link node-to-node flow routing with Gauckler-Manning-Strickler models. In order to reinterpret the node-to-node flow routing algorithms as finite volume schemes, we must associate a volume to each node. The easiest way to do so is to consider the dual mesh, formed by joining the centers of the cells of the primal mesh (see again Fig. **??**, where the dual mesh corresponds to the dashed lines). On the dual mesh, the node (i,j) of the primal mesh becomes the center of the dual cell $K_{i,j}$. The cartesian mesh (plain lines) and its dual (dashed lines)~~

~~Decomposition and notations for the dual cartesian cell boundaries In Fig. **??**, we propose a decomposition of the boundary of the dual cartesian cell $K_{i,j}$ centered on the primal node (i,j) into 12 faces $(\sigma_l)_{1\leq l\leq 12}$. The faces $\sigma_{j\pm1}$ are of length $\gamma_x\Delta x$, with of course the faces $\sigma_{j\pm1}^{i\pm1}$ of length $\frac{1-\gamma_x}{2}\Delta x$. In the same way, faces $\sigma_{i\pm1}$ are of length $\gamma_y\Delta y$ and the faces $\sigma_{i\pm1}^{j\pm1}$ of length $\frac{1-\gamma_y}{2}\Delta y$. Using those notations, we integrate over the dual cell $K_{i,j}$ to get:~~

~~$$-\sum_{l=1}^{12}\int_{\sigma_l} k_m h_w \eta_w(h_w) s_{ref}^{-p_w} ||\nabla(h_s+b)||^{p_w}\nabla(h_s+b)\cdot\boldsymbol{n}_{K_{i,j}} = |K_{i,j}|S_{w,K}.$$~~

~~On the four faces σ_{i-1}, σ_{i+1}, σ_{j-1} and σ_{j+1}, we use the same finite volume discretization than before~~k_w will play a key role in the stability of solutions. Indeed denoting $\tau = (k_w q_w^{r_s})/(k_g q_{ref}^{r_s})$, if k_g is much larger than k_w large and thus τ is very small

we have assuming for simplicity that $\eta_s = 1$:

$$\int_{\sigma_{j-1}} A_\delta \approx k_m h_w \eta_w g s_{ref}^{-p_s} \left(||\nabla(h_{w\,s,*} + b) s_{ref}^{-p_w}||^{p_s} - ||\nabla(h_s + b)||^{p_w p_s} \right) \nabla(h_{s\,s,*} + b) \cdot K_{i,j} \nabla h_{s,\delta} + O(\tau)$$

$$\approx \frac{\gamma_x \Delta x}{s_{ref}^{p_w} \Delta y} k_{m,\sigma_{j-1}} - k_g s_{ref}^{-p_s} \left(p_s ||_{s,\sigma_{j-1}} \nabla(h_{s,*} + b)||^{p_w} h_{w,\sigma_{j-1}}^{up\ p_s - 2} |\nabla(h_{s,i,j-1\,s,*} + b_{i,j-1} -) \cdot \nabla h_{s,i,j} - b_{i,j\,s,\delta}|^2 \right) + O(\tau), + O(\delta^3).$$

~~and~~

$$\int_{\sigma_{i-1}} k_m h_w \eta_w(h_w) s_{ref}^{-p_w} ||\nabla(h_s + b)||^{p_w} \nabla(h_s + b) \cdot \boldsymbol{n}_{K_{i,j}}$$

$$\approx \frac{\gamma_y \Delta y}{s_{ref}^{p_w} \Delta x} k_{m,\sigma_{i-1}} ||\boldsymbol{G}_{s,\sigma_{i-1}}||^{p_w} h_{w,\sigma_{i-1}}^{up}(h_{s,i-1,j} + b_{i-1,j} - h_{s,i,j} - b_{i,j}),$$

~~and~~

$$\int_{\sigma_{j+1}} k_m h_w \eta_w(h_w) s_{ref}^{-p_w} ||\nabla(h_s + b)||^{p_w} \nabla(h_s + b) \cdot \boldsymbol{n}_{K_{i,j}}$$

$$\approx \frac{\gamma_x \Delta x}{s_{ref}^{p_w} \Delta y} k_{m,\sigma_{j+1}} ||\boldsymbol{G}_{s,\sigma_{j+1}}||^{p_w} h_{w,\sigma_{j+1}}^{up}(h_{s,i,j+1} + b_{i,j+1} - h_{s,i,j} - b_{i,j}),$$

~~and~~

$$\int_{\sigma_{i+1}} k_m h_w \eta_w(h_w) s_{ref}^{-p_w} ||\nabla(h_s + b)||^{p_w} \nabla(h_s + b) \cdot \boldsymbol{n}_{K_{i,j}}$$

$$\approx \frac{\gamma_y \Delta y}{s_{ref}^{p_w} \Delta x} k_{m,\sigma_{i+1}} ||\boldsymbol{G}_{s,\sigma_{i-1}}||^{p_w} h_{w,\sigma_{i+1}}^{up}(h_{s,i+1,j} + b_{i+1,j} - h_{s,i,j} - b_{i,j}),$$

~~while for the remaining height cells, we gather the faces to form the corners illustrated in Fig. . More precisely, we denote~~(where we recall that a function f is $O(h)$ if there exists a constant $C > 0$ independent on h such that $||f|| \leq Ch$ for a suitable norm $||.||$). Then for large values of k_g the term A_δ is always negative and thus stabilizing. On the contrary, if k_w is much larger than k_g then τ is also very large and we have:

$$_{i-1,j-1} = {}^{j-1}_{i-1} \cup {}^{i-1}_{j-1}, A_\delta \approx -k_w s_{ref}^{-p_s} q_{ref}^{-r_s} \left(q_{w,*}^{r_s} ||\nabla(h_{s,*} + b)||^{p_s} - q_w^{r_s} ||\nabla(h_s + b)||^{p_s} \right) \nabla(h_{s,*} + b) \cdot \nabla h_{s,\delta} + O(1/\tau)$$

$$_{i-1,j+1} = {}^{j+1}_{i-1} \cup {}^{i-1}_{j+1}, \approx -k_w s_{ref}^{-p_s} r_s \frac{q_{w,*}^{r_s - 1}}{q_{ref}^{r_s}} q_{w,\delta} ||\nabla(h_{s,*} + b)||^{p_s} \nabla(h_{s,*} + b) \cdot \nabla h_{s,\delta}$$

$$i+1,j-1 = \overline{i+1}^{j-1} \cup \overline{j-1}^{i+1}, -k_w s_{ref}^{-p_s} \left(\frac{q_{w,*}}{q_{ref}} \right)^{r_s} \sim \left(p_s ||\nabla(h_{s,*}+b)||^{p_s-2} |\nabla(h_{s,*}+b) \cdot \nabla h_{s,\delta}|^2 \right) + O(1/\tau) + O(\delta^3).$$

$$\overline{\sigma}_{i+1,j+1} = \overline{\sigma}_{i+1}^{j+1} \cup \overline{\sigma}_{j+1}^{i+1},$$

~~those four corners, $\sigma_{i\pm1,j\pm1}$ thus being the corner corresponding to the neighbouring cell $K_{i\pm1,j\pm1}$. On those corners, we perform the same discretization than before considering the whole corner as if it was a single face: in other words we use constant values $k_{m,\sigma}$ and $||\boldsymbol{G}_{s,\sigma}||^{p_w}$~~ Regions for which $\nabla(h_{s,*}+b) \cdot \nabla h_{s,\delta} < 0$ will amplify the perturbation proportionally to k_w and the power $r_s - 1$ of the water flux. We also see that the term A_δ will behave quite differently if $r_s > 1$ or $r_s < 1$. Indeed, for ~~k_m and $||\nabla(h_s+b)||^{p_w}$ along the corner, an upwind scheme for the unknown $h_w \eta_w(h_w)$ and the a two-point flux formula for in the average normal direction to the corner. Denoting $(\nabla(h_s+b))_{\sigma_{i\pm1,j\pm1}}$ the equivalent constant gradient exact for linear function underlying the TFPA along the corner, this leads to the following approximation:~~

$$\int_{\sigma_{i\pm1,j\pm1}} k_m h_w \eta_w(h_w) s_{ref}^{-p_w} ||\nabla(h_s+b)||^{p_w} \nabla(h_s+b) \cdot \boldsymbol{n}_{K_{i,j}} \approx$$

$$k_{m,\sigma_{i\pm1,j\pm1}} s_{ref}^{-p_w} ||\boldsymbol{G}_{s,\sigma_{i\pm1,j\pm1}}||^{p_w} h_{w,\sigma_{i\pm1,j\pm1}}^{up} (\nabla(h_s+b))_{\sigma_{i\pm1,j\pm1}} \cdot \int_{\sigma_{i\pm1,j\pm1}} \boldsymbol{n}_{K_{i,j}}.$$

~~By construction~~$r_s > 1$ the water flux will reinforce the amplification term in a kind of positive feedback loop. On the contrary, for $r_s < 1$ the water flux will temper the amplification term, thus we can anticipate that it will require much larger values of τ for instability to occur in this situation. Going back to the general case for η_s, we have for small values of τ:

$$\int_{\sigma_{i\pm1,j\pm1}} \overline{K_{i,j}} = \frac{(1-\gamma_y)}{2}\Delta y \frac{(1-\gamma_x)}{2}\Delta x, A_\delta \approx -k_g s_{ref}^{-p_s} \left(\eta_s'(h_{s,*}) ||\nabla(h_{s,*}+b)||^{p_s} h_{s,\delta} \nabla(h_{s,*}+b) \cdot \nabla h_{s,\delta} + \right.$$

~~Denoting~~

$$p_s \eta_s(h_{s,*}) |\sigma_{i\pm1,j\pm1}| = \frac{(1-\gamma_x)}{2}\Delta x \nabla(h_{s,*} + \frac{(1-\gamma_y)}{2}\Delta y = b) ||^{p_s-2} |\nabla(h_{s,*}+b) \cdot \nabla h_{s,\delta}|^2 \Big) + O(\tau) + O(\delta^3).$$

~~we seek γ_x and γ_y such that~~while for large values of τ we have:

$$\frac{(1-\gamma_x)}{2\delta}\Delta x = \frac{\Delta y}{(\Delta x^2+\Delta y^2)^{1/2}} \text{ and } \frac{(1-\gamma_x)}{2\delta}\Delta y = \frac{\Delta x}{(\Delta x^2+\Delta y^2)^{1/2}}, A_\delta \approx -k_w s_{ref}^{-p_s} r_s \frac{q_{w,*}^{r_s-1}}{q_{ref}^{r_s}} q_{w,\delta} \eta_s(h_{s,*}) ||\nabla(h_{s,*}+b)||^{p_s} \nabla(h_{s,*}+b)$$

~~leading to:~~

$$\gamma_x = 1 - \frac{2\delta\Delta y/\Delta x}{(\Delta x^2+\Delta y^2)^{1/2}} \quad \text{and } \gamma_y = 1 - \frac{2\delta\Delta x/\Delta y}{(\Delta x^2+\Delta y^2)^{1/2}},$$

$$-k_w s_{ref}^{-p_s}\left(\frac{q_{w,*}}{q_{ref}}\right)^{r_s}\left(\eta_s'(h_{s,*})||\nabla(h_{s,*}+b)||^{p_s}h_{s,\delta}\nabla(h_{s,*}+b)\cdot\nabla h_{s,\delta}+\right.$$

~~which can be achieved with $\gamma_x \geq 0$ and $\gamma_y \geq 0$ provided δ satisfies:~~

$$0 \leq \delta \leq \frac{1}{2}\min\left(\frac{\Delta x}{\Delta y}, \frac{\Delta y}{\Delta x}\right)(\Delta x^2+\Delta y^2)^{1/2}.$$

$$\left.p_s\eta_s(h_{s,*})||\nabla(h_{s,*}+b)||^{p_s-2}|\nabla(h_{s,*}+b)\cdot\nabla h_{s,\delta}|^2\right)+O(1/\tau)+O(\delta^3).$$

~~With this choice for γ_x and γ_y, for all δ satisfying we get that~~

$$\int_{\sigma_{i\pm1,j\pm1}} \boldsymbol{n}_{K_{i,j}} = \frac{\pm\Delta x}{(\Delta x^2+\Delta y^2)^{1/2}}\boldsymbol{e}_x + \frac{\pm\Delta y}{(\Delta x^2+\Delta y^2)^{1/2}}\boldsymbol{e}_y,$$

~~and thus the average normal at the corner $\sigma_{i\pm1,j\pm1}$ is precisely pointing from $\boldsymbol{x}_{K_{i,j}}$ to $\boldsymbol{x}_{K_{i\pm1,j\pm1}}$. Thus it is natural to use the two point flux formula:~~

$$(\nabla(h_s+b))_{\sigma_{i\pm1,j\pm1}}\cdot\int_{\sigma_{i\pm1,j\pm1}}\boldsymbol{n}_{K_{i,j}} \approx \frac{\delta}{(\Delta x^2+\Delta y^2)^{1/2}}(h_{s,i\pm1,j\pm1}+b_{i\pm1,j\pm1}-h_{s,i}-b_i).$$

~~The upwinding is done exactly as before, following the sign of the difference in elevation h_s+b between the two value forming the TPFA. This gives for the non-corners:~~

$$h^{up}_{w,\sigma_{i\pm1}} = \begin{cases} h_{w,i,j}\eta_w(h_{w,i,j}) & \text{if } h_{s,i,j}+b_{i,j} \geq h_{s,i\pm1,j}+b_{i\pm1,j}, \\ h_{w,i\pm1,j}\eta_w(h_{w,i\pm1,j}) & \text{if } h_{s,i,j}+b_{i,j} < h_{s,i\pm1,j}+b_{i\pm1,j}, \end{cases}$$

$$h^{up}_{w,\sigma_{j\pm1}} = \begin{cases} h_{w,i,j}\eta_w(h_{w,i,j}) & \text{if } h_{s,i,j}+b_{i,j} \geq h_{s,i,j\pm1}+b_{i,j\pm1}, \\ h_{w,i,j\pm1}\eta_w(h_{w,i,j\pm1}) & \text{if } h_{s,i,j}+b_{i,j} < h_{s,i,j\pm1}+b_{i,j\pm1}, \end{cases}$$

~~and for the corners:~~

$$h^{up}_{w,\sigma_{i\pm1,j\pm1}} = \begin{cases} h_{w,i,j}\eta_w(h_{w,i,j}) & \text{if } h_{s,i,j}+b_{i,j} \geq h_{s,i\pm1,j\pm1}+b_{i\pm1,j\pm1}, \\ h_{w,i\pm1,j\pm1}\eta_w(h_{w,i\pm1,j\pm1}) & \text{if } h_{s,i,j}+b_{i,j} < h_{s,i\pm1,j\pm1}+b_{i\pm1,j\pm1}. \end{cases}$$

~~To get more compact notations, let us denote~~

$$\mathcal{N}(i,j) = \{(m,n) \in \{i-1,i,i+1\}\times\{j-1,j,j+1\} \mid (m,n) \leq (i,j)\},$$

the neighbours of node (i,j), and define the transmissivities:

$$\tau_{i,j}^{m,n} = \begin{cases} \dfrac{\gamma_x \Delta x}{s_{ref}^{p_w} \Delta y} k_{m,\sigma_{j\pm1}} ||\boldsymbol{G}_{s,\sigma_{j\pm1}}||^{p_w} & \text{if } (m,n) = (i,j-1) \text{ or } (i,j+1), \\ \dfrac{\gamma_y \Delta y}{s_{ref}^{p_w} \Delta x} k_{m,\sigma_{i\pm1}} ||\boldsymbol{G}_{s,\sigma_{i\pm1}}||^{p_w} & \text{if } (m,n) = (i-1,j) \text{ or } (i+1,j), \\ \dfrac{\delta}{s_{ref}^{p_w} (\Delta x^2 + \Delta y^2)^{1/2}} k_{m,\sigma_{i\pm1,j\pm1}} ||\boldsymbol{G}_{s,\sigma_{i\pm1,j\pm1}}||^{p_w} & \text{otherwise,} \end{cases}$$

assuming for simplicity that the gradients $\boldsymbol{G}_{s,\sigma}$ are obtained on the dual mesh in the same way as in the cell-to-cell case (of course, a reconstruction formula using also the diagonal neighbours is possible). Using those notations, we get gathering by upwind kind as in the case of the cell-to-cell flow routing the following expression for the proposed finite volume scheme on the dual mesh:

$$h_{w,i,j}\eta_w(h_{w,i,j}) \left(\sum_{(m,n)\in\mathcal{N}(i,j), h_{s,i,j}+b_{i,j} > h_{s,m,n}+b_{m,n}} \tau_{i,j}^{m,n} (h_{s,i,j} + b_{i,j} - h_{s,m,n} - b_{m,n}) \right)$$

$$- \left(\sum_{(m,n)\in\mathcal{N}(i,j), h_{s,i,j}+b_{i,j} < h_{s,m,n}+b_{m,n}} \tau_{i,j}^{m,n} h_{w,m,n}\eta_w(h_{w,m,n})(h_{s,m,n} + b_{m,n} - h_{s,i,j} - b_{i,j}) \right) = |K_{i,j}| S_{w,i,j}.$$

Proceeding as in the cell-to-cell case, denoting:

$$s_{i,j} = \sum_{(m,n)\in\mathcal{N}(i,j), h_{s,i,j}+b_{i,j} > h_{s,m,n}+b_{m,n}} \tau_{i,j}^{m,n} (h_{s,i,j} + b_{i,j} - h_{s,m,n} - b_{m,n}) \quad \text{and} \quad \widetilde{q}_{i,j} = h_{w,i,j}\eta_w(h_{w,i,j}) s_{i,j}$$

, we finally get:

$$\widetilde{q}_{i,j} - \left(\sum_{(m,n)\in\mathcal{N}(i,j), h_{s,i,j}+b_{i,j} < h_{s,m,n}+b_{m,n}} \tau_{i,j}^{m,n} \frac{\widetilde{q}_{m,n}}{s_{m,n}} (h_{s,m,n} + b_{m,n} - h_{s,i,j} - b_{i,j}) \right) = |K_{i,j}| S_{w,i,j}.$$

The flow sharing formula common to all flow routing algorithms of the literature identifies in this context with the ratios:

$$\frac{1}{s_{m,n}} \tau_{i,j}^{m,n} (h_{s,m,n} + b_{m,n} - h_{s,i,j} - b_{i,j}),$$

for $(m,n) \in \mathcal{N}(i,j), h_{s,i,j} + b_{i,j} < h_{s,m,n} + b_{m,n}$, which expresses how node (i,j) receives water from other nodes. Reversing the point of view, it rewrites in probably more familiar fashion by expressing how node (i,j) distributes water to its neighbours through the flow sharing formula (noticing that $\tau_{i,j}^{m,n} = \tau_{m,n}^{i,j}$):

$$\frac{\tau_{i,j}^{m,n} \max(0, h_{s,i,j} + b_{i,j} - h_{s,m,n} - b_{m,n})}{\sum_{m',n'\in\mathcal{N}(i,j)} \tau_{i,j}^{m',n'} \max(0, h_{s,i,j} + b_{i,j} - h_{s,m',n'} - b_{m',n'})}.$$

Notice that several attempts of the literature at improving the behavior of the flow routing consider powers q of the two point slope instead of the slope in The behavior is roughly speaking the same, with the main difference that the flow sharing formula, which with our notations rewrites:

$$\frac{\tau_{i,j}^{m,n}\max(0,h_{s,i,j}+b_{i,j}-h_{s,m,n}-b_{m,n})^q}{\sum_{m',n'\in\mathcal{N}(i,j)}\tau_{i,j}^{m',n'}\max(0,h_{s,i,j}+b_{i,j}-h_{s,m',n'}-b_{m',n'})^q}.$$

Another important consequence of the formal identification of cell-to-cell flow routing algorithms with a numerical scheme for additional term in $\eta_s'(h_{s,*})$ can also contribute with the wrong sign. Since $\eta_s'(h_{s,*})$ will be almost zero as soon as $h_{s,*}$ is large enough (see equation (**??**)), this can only happens in regions where $h_{s,*}$ is close to zero (in particular near Dirichlet boundaries). In this case, the potential contribution to the stationary Gauckler-Manning-Strickler model is the fact that if one wants to incorporate powers of the slope in the flow distribution procedure, then one should not use powers of the directional slope $\frac{1}{d_{KL}}(h_{s,L}+b_L-h_{s,K}-b_K)$ but rather use powers of $||\boldsymbol{G}_{s,\sigma}||$ to remain consistent with a continuous model incorporating powers of $||\nabla(h_s+b)||$. Otherwise, the consistency of the flow routing algorithm will be lost again. In **?** it is even suggested to choose different values of q for different grid sizes, emphasizing this non-consistency. However, the sought flow concentration effect can be achieved in a consistent manner through the use of p_w: the full gradient and not only the directional gradient being used this way, this does not endanger consistency and a value independent of the mesh should be chosen according to physical considerations. An option that we do not consider here is to make the value of p_w spatially variable, as was suggested in **?** but still on the non-consistent formulation . instabilities is controlled by the magnitude of $|\eta_s'(h_{s,*})h_{s,\delta}| \leq |h_{s,\delta}|/h_c$. If the perturbation is not amplified by other engines, which will be the case if τ is small, and if the parameter h_c is not chosen too small (a typical valid value is 20 cm), then no severe instability can occur through this additional term. Thus we can be confident that parameter τ will be the main criterion governing the appearance of instabilities even for our most general model.

Although clearly leads to some non consistency, this expression is useful to derive a classification of the most prominent flow routing algorithms of the literature. To exactly match the definitions of most node-to-node flow routing schemes of the literature, we now consider the special case of square cartesian cells for which $\Delta x = \Delta y = \Delta_{xy}$. In For a subclass of model (**??**)-(**??**)-(**??**) with $\eta_s = 1$, $k_g = 0$ and $p_w = -1$ and $p_s = 0$, the stability of solutions have been theoretically studied in **??** . It was for instance established in **?** that if the reference solution is stationary, that the second term is negative only if some specific condition on the gradient $\nabla(h_s+b)$ is satisfied on the boundary of the region of interest, here Ω. The linear stability of analytic stationary solutions that are uniform in one direction has also been considered in **?**. Their conclusion is that under periodic perturbations in the transverse direction, for $r_s \leq 1$, the linear stability analysis does not reveal any instability while for $r_s > 1$, the stationary solutions are linearly unstable if the frequency of the periodic perturbation is large enough. Notice that the case $p_w = -1$ greatly simplifies such studies: the linear stability analysis can be showed to be equivalent to solving a one dimensional ordinary differential equation.

The studies mentioned above are focused on the stability of physically meaningful solutions. Here, we want to draw attention

on the numerical consequences of this ~~case we get from that $\gamma_x = \gamma_y = 1 - (2\delta)/(\sqrt{2}\Delta_{xy})$. It remains to choose a value for δ. The most natural choice is choose to enforce $\delta = \gamma_x \Delta x = \gamma_y \Delta y$ and thus balance the contribution to each neighbour. This immediately leads to~~self-amplification phenomenon, in this way we focus on the stability of numerical solutions. Let us explain the key idea: assuming that all functions are regular enough, one could consider (for instance in a finite difference setting) that our numerical solution is roughly speaking a perturbation of the exact continuous solution, where the source terms $S_{s,\delta}$ and $S_{w,\delta}$ represent the unavoidable consistency and solver errors of our solving process. Then the numerical sediment perturbation energy will satisfy (**??**) and will self-amplify in the same way than physical perturbations self-amplify. In the unstable regime, this means than the numerical solution can potentially diverge from the exact one from a large amount up to the point that it cannot be considered a relevant approximation of the continuous solution, even if the numerical perturbation arises from initially small numerical errors.

3 Numerical instabilities arising from the non linear coupling of overland flow and sediment dynamic

To illustrate the numerical issues linked to the self-amplification of initially small numerical errors, we consider in this section several situations where we have either the full knowledge of the exact solution or a criterion to distinguish it from incorrect solutions. Thanks to those information on the exact solution, we can illustrate the stability issues of simulations using model (**??**)-(**??**)-(**??**) (discretized by the finite volume scheme detailed in appendix **??**).

3.1 Instabilities for analytic solutions

In this subsection we consider stationary analytic functions of the form:

$$\delta = \frac{\sqrt{2}}{2+\sqrt{2}}\Delta_{xy} \text{ and } \gamma_x = \gamma_y = \frac{\sqrt{2}}{2+\sqrt{2}}, \quad \left| \begin{array}{l} h_s^{ex}(x,y) = h_{s,x}(x) + \sum_{p=1}^{N_b} g_b\left(\frac{x-x_p}{\delta_x}, \frac{y-y_p}{\delta_y}\right), \\ h_w^{ex}(x,y) = h_{w,x}(x), \end{array} \right.$$

~~implying that~~ incorporating N_b small smooth bumps randomly positioned at points (x_p, y_p) chosen such that they do interfere with the boundary conditions, with the smooth bump function given by:

$$\frac{\delta}{(\Delta x^2 + \Delta y^2)^{1/2}} g_b(x,y) = \frac{1}{2+\sqrt{2}} \text{ and } \frac{\gamma_x \Delta x}{\Delta y} g_b(r^2) = \frac{\sqrt{2}}{2+\sqrt{2}} \text{ and } \frac{\gamma_y \Delta y}{\Delta x} = \frac{\sqrt{2}}{2+\sqrt{2}}, \quad \left| \begin{array}{ll} H_{pert} \exp\left(\frac{-\gamma}{1-r^2}\right) \exp(\gamma) & \text{for } r^2 = x^2 + y \\ 0 & \text{otherwise .} \end{array} \right.$$

~~thus the diagonal transmissivities differ from the non-diagonal ones by the factor $1/\sqrt{2}$ which corresponds to the D8, Rho8 and most MFD algorithms. To recover the FD8/TOPMODEL noticing that the L_1 and L_2 non diagonal and diagonal "face measures" of this MFD algorithm satisfy $L_1 = \Delta_{xy}/2$~~ with in practice N_b=5, H_{pert}=0.03 m, γ=10 and ~~$L_2 = \frac{\sqrt{2}}{4}\Delta_{xy}$, we recover the same weighting within our notations by setting~~

$$\delta = \frac{\sqrt{2}}{4}\Delta_{xy} \quad \text{and} \quad \gamma_x = \gamma_y = \frac{1}{2},$$

which is compatible with as in this case :

$$\frac{(1-\gamma_x)}{2\delta}\Delta x = \frac{(1-\gamma_y)}{2\delta}\Delta y = \frac{1}{\sqrt{2}} = \frac{\Delta x}{(\Delta x^2+\Delta y^2)^{1/2}} = \frac{\Delta y}{(\Delta x^2+\Delta y^2)^{1/2}}.$$

Finally denoting:

$$\Delta\mathcal{H}_{i,j}^{m,n} = \max(0, h_{s,i,j} + b_{i,j} - h_{s,m,n} - b_{m,n}),$$

in table **??** we recast the most classical MFD algorithms using our notations, with $p_w = 0$ for all the presented methods. For the Rho8 method (**?**),the ρ_8 parameter is a random number generated for each face, while for the MFD-md (**?**), the parameter e is the maximum downslope gradient and $f(e) = 8.9\min(e, 1) + 1.1$.

This reinterpretation calls for several comments.The main one is that the node-to-node situation is no better than the cell-to-cell one: $\widetilde{q}_{i,j}$ will be as non consistent,non convergent and thus strongly mesh dependent than its cell-to-cell counterpart.The node-to-node routing is indeed simply a cell-to-cell routing on a dual mesh, with a more involved cell boundary decomposition. The quantity $\widetilde{q}_{i,j}$ should not be used to couple with sediment evolution, one should instead reconstruct a consistent water flux vector $\boldsymbol{Q}_{i,j}$ for instance by setting:

$$\boldsymbol{Q}_{i,j} = \sum_{(m,n)\in\mathcal{N}(i,j), h_{s,i,j}+b_{i,j}>h_{s,m,n}+b_{m,n}} \frac{\tau_{i,j}^{m,n}\widetilde{q}_{i,j}}{|K_{i,j}|s_{i,j}}(h_{s,i,j}+b_{i,j}-h_{s,m,n}-b_{m,n})(\boldsymbol{x}_{i,j}^{m,n}-\boldsymbol{x}_{K_{i,j}})-$$

$$\sum_{(m,n)\in\mathcal{N}(i,j), h_{s,i,j}+b_{i,j}<h_{s,m,n}+b_{m,n}} \frac{\tau_{i,j}^{m,n}\widetilde{q}_{m,n}}{|K_{i,j}|s_{m,n}}(h_{s,m,n}+b_{m,n}-h_{s,i,j}-b_{i,j})(\boldsymbol{x}_{i,j}^{m,n}-\boldsymbol{x}_{K_{i,j}})$$

where:

$$\boldsymbol{x}_{i,j}^{m,n} = \begin{cases} \frac{1}{2}(\boldsymbol{x}_{K_{i,j}} + \boldsymbol{x}_{K_{m,n}}) & \text{if } (m,n)\in\{(i,j-1),(i,j+1),(i-1,j),(i+1,j)\} \\ \frac{1}{|\sigma_m^n|+|\sigma_n^m|}\left(|\sigma_m^n|\boldsymbol{x}_{\sigma_m^n} + |\sigma_n^m|\boldsymbol{x}_{\sigma_n^m}\right) & \text{otherwise} \end{cases}$$

and then use $q_{i,j} = ||\boldsymbol{Q}_{i,j}||$ which again can be considered as an easy to implement post-processing consistency correction step.The second one is that it is clear that contrary to what is done in some flow routing algorithms of the literature, the chosen value for $k_{m,\sigma}$ should be a discretization of an inverse of acontinuous roughness with amore or less physical interpretation. Apart from the unavoidable sampling induced by the mesh, it should be as mesh independent as possible and in particular should not depend on cell orientations. The single flow direction D8 δ_x=δ_y=0.25 km. The numerical domain is rectangular and centered at (0,0) with the dimensions $Lx = 1$ km in the x axis and $Ly = 5$ km in the y axis, and Rho8 methods reinterpreted this way introduce a coefficient $k_{m,\sigma}$ that is clearly mesh dependent and not the discretization of a continuous coefficient. This will consequently increase the mesh dependency of the overall method.The two point flux approximation (TPFA) is of course not the only possible approximation for the terms $(\nabla(h_s+b))_{\sigma_{i\pm1,j\pm1}} \cdot \int_{\sigma_{i\pm1,j\pm1}} \boldsymbol{n}$. In particular, if one reconstructs an

approximation $\hat{\boldsymbol{G}}_{s,\sigma}$ of the full topographic gradient along each face σ, then it can be used to compute an approximation of the flux. We denote it $\hat{\boldsymbol{G}}_{s,\sigma}$ to distinguish it from the reconstruction $\boldsymbol{G}_{s,\sigma}$ used to approximate the non-linear dependency in the slope, as the two can be different. In this case, becomes:

$$\frac{|\sigma_{m,n}|(\Delta\mathcal{H}_{i,j}^{m,n})^q}{\sum_{m',n'\in\mathcal{N}(i,j)}|\sigma_{m',n'}|(\Delta\mathcal{H}_{i,j}^{m',n'})^q} \quad \text{and} \quad \Delta\mathcal{H}_{i,j}^{m,n} = \max\left(0, \hat{\boldsymbol{G}}_{s,\sigma_{m,n}} \cdot \int_{\sigma_{m,n}} \boldsymbol{n}_{K_{i,j}}\right).$$

Then, more flow routing algorithms of the literature can be rewritten this way. In particular, choosing $\gamma_x = \gamma_y = 0$ or 1 we can easily recover the flux decomposition method (Desmet et al. 1996 **?**) and a variation of the MD∞ method (Seibert et al. 2007 **?**). The flux decomposition method chooses a single value for $\hat{\boldsymbol{G}}_{s,K_{i,j}}$ for each cell, the basement b is set to zero. We impose homogeneous Dirichlet boundary conditions ($h_s = 0$) on the boundaries $x = -Lx/2$ and $x = Lx/2$ and homogeneous Neumann boundary conditions ($\partial_y h_s = 0$) on the boundaries $y = -Ly/2$ and then loop over cells and set $\hat{\boldsymbol{G}}_{s,\sigma} = \hat{\boldsymbol{G}}_{s,K_{i,j}}$ for the faces of the current cell that have not already been handled through a previous cell in $y = Ly/2$ as illustrated on figure **??**. We use for the monodimensional functions ($h_{s,x}$,$h_{w,x}$) the stationary solution of model (**??**)-(**??**)-(**??**) in the case $\eta_s = 1$

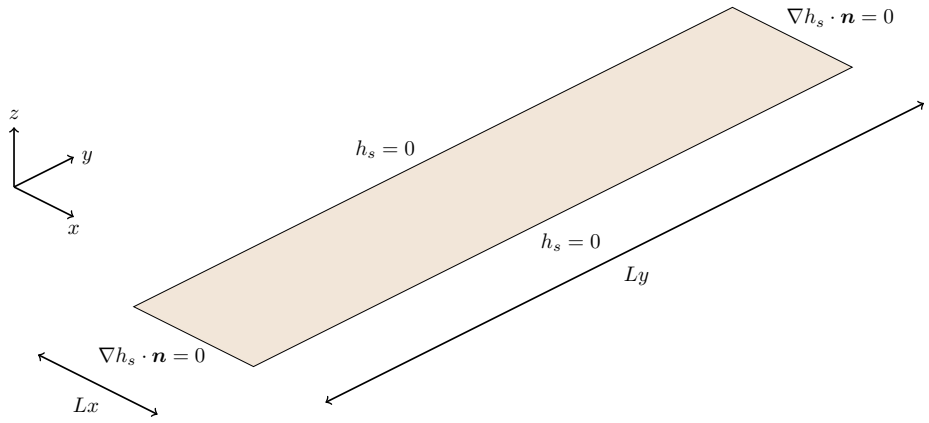

Figure 3. Domain configuration for the analytic tests cases

given in appendix **??** that satisfies the boundary conditions. For all our simulations, the loop. The MD∞ methods computes $\hat{\boldsymbol{G}}_{s,\sigma}$ for each face using a triangular reconstruction of the slope: to be precise, with our notations $\hat{\boldsymbol{G}}_{s,\sigma}$ is for face $\sigma_{m,n}$ half the sum of the two triangular gradients computed in **?** that can contribute to $\sigma_{m,n}$. We say that this is a variation of **?** as it is unclear whether they use the normal component of the gradient as we do here or the full norm of constant source terms ($S_{s,x}$,$S_{w,x}$) for the gradient in their flow sharing formula. Other flow routing algorithms than do not seem to easily enter this framework are also available in the literature.We mention in particular the ANSWERS (**?**), DEMON (**?**)and Lea's method (**?**) , that are all based on a local planar approximation of the topography and use either a multiple or single direction flow sharing

formula based on purely geometric considerations.The D∞ method (Tarboton 1997 ?)strongly looks like the SFD method at first sight, however because the flow sharing formula used when analytic the stationary solution $(h_{s,x}, h_{w,x})$ in the case $\eta_s = 1$ (see appendix ?? for details) are always equal to (10 m.My^{-1},1 m^3.s^{-1}km^{-2}). Injecting (h_s, h_w) into (??)-(??)-(??), after some straightforward but tedious computations one can derive exact expressions for the corresponding source terms (S_s^{ex}, S_w^{ex}), making the pair (h_s, h_w) an analytic solution of our model for those source terms.

Given those analytic source terms, initializing the sediment height to the steepest direction is not aligned with meshdirection is based on angular considerations similar to those of ANSWERS and DEMON, it is not immediately obvious how to relate the D∞ method to a continuous model. Finally, let us mention that many variations around the classical algorithms have been explored since their first publications leading for instance to some generalization to triangular meshes ??. We refer the reader to ??? and references therein for a broader review on flow routing algorithms and their numerical behavior.

4 Large structures simulation for numerical instabilities free landscape evolution models

In this section, after illustrating the numerical problems arising when non-linearly coupling water flow and sediment evolution on an easy to analyze synthetic test case, we explain how to transpose the ideas underlying the concept of large eddy simulation from the computational fluid dynamics community to our landscape evolution model. In our opinion, this is a key ingredient for achieving reproducible LEM simulations. All the simulations shown in the following sections are performed using the ArcaDES platform (?) (although ArcaDES is mentioned for the first time in a scientific paper, it is used since 2015 in the stratigraphic numerical forward model DionisosFlow™ initially developed by ?).

3.1 Model description

At first let us mention that all the observations, conclusions and recommendations coming from this section are not linked to any specific sediment evolution model and should in principle apply to any coherent sediment model satisfying (H1) , (H2)and (H3) . In the present paper we have chosen to focus on the sediment model that has already been discussed in detail in ????:

$$\boldsymbol{J}_s = -\eta_s(h_s) s_{ref}^{-p_s} ||\nabla(h_s+b)||^{p_s} \left(\left(\frac{q_w}{q_{ref}} \right)^{r_s} \nabla\psi_w(h_s+b) + \nabla\psi_g(h_s+b) \right) \quad \text{in } \Omega\times]t_0, T[,$$

where $r_s > 0$ and $p_s > 0$ are model parameters, q_w is the water flux obtained from analytic value $h_s(x,y,0) = h_s^{ex}(x,y)$ and the water height to the analytic value $h_w(x,y,0) = h_w^{ex}(x,y)$ the exact solution of model (??)-(??)-(??) is of course simply equal to (h_s^{ex}, h_w^{ex}) for all times. Thus, any reasonable numerical solution should remain a correct approximation of (h_s^{ex}, h_w^{ex}) for all times.

Using the finite volume discretization described in appendix ?? on a cartesian mesh with square cells for which we denote Δ_{xy} the size of the edges of the cartesian cells, we attempt to reproduce the stationary analytic solution by initializing the system to $(h_s(x,y,0), h_w(x,y,0))$=$(h_s^{ex}(x,y), h_w^{ex}(x,y))$ and using the analytic source terms (S_s^{ex}, S_w^{ex}), for various values of the parameters k_g, k_w r_s and p_s. The simulation total time is 0.25 My, and we use time steps of maximum length Δt=0.002

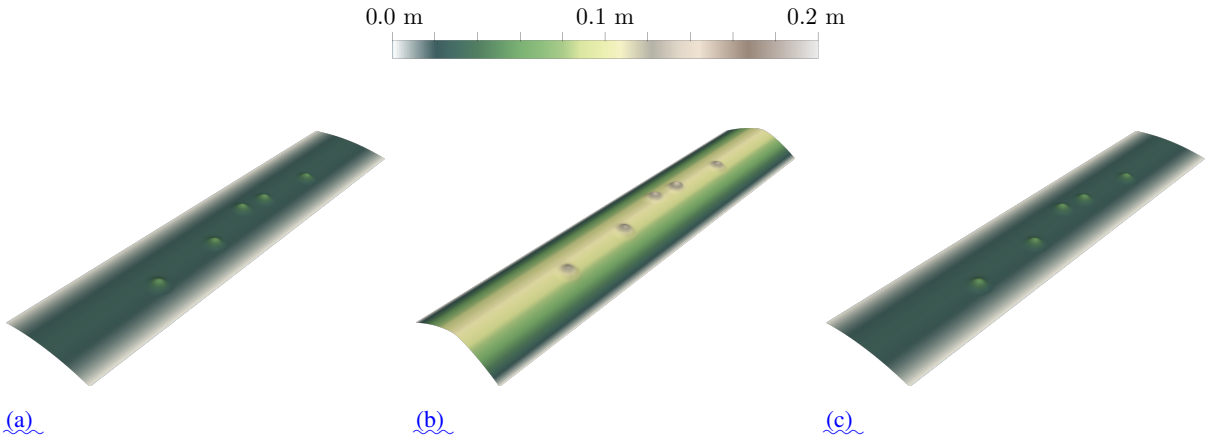

Figure 4. Sediment height h_s^{ex} of the analytic solution for the case k_g=50 km^2.My^{-1} and k_w=1 km^2.My^{-1}. a: r_s=1, p_s=0, b: r_s=3/2, p_s=1, c: r_s=2, p_s=0

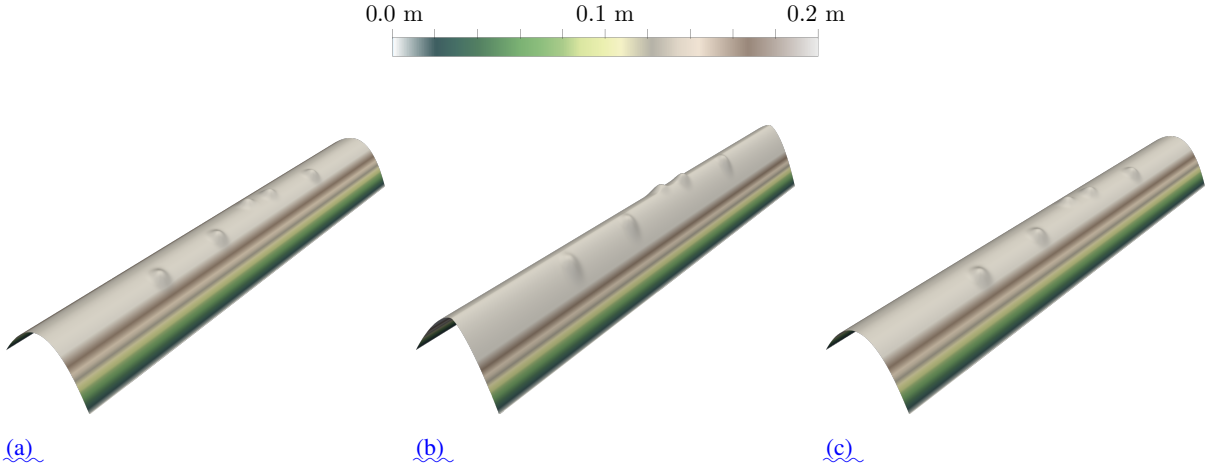

Figure 5. Sediment height h_s^{ex} of the analytic solution for the case k_g=5 km^2.My^{-1} and k_w=1 km^2.My^{-1}. a: r_s=1, p_s=0, b: r_s=3/2, p_s=1, c: r_s=2, p_s=0

My. The corresponding analytic solutions are presented on figures **??**, **??**, **??** and **??** for the different values of the parameters k_g, ~~q_{ref}~~ k_w r_s and ~~s_{ref} are dimensional factors, and η_s is a dimensionless sediment mobility function such that:~~

$$0 \leq \eta_s(u) \leq 1 \quad \text{and} \quad \eta_s(0) = 0,$$

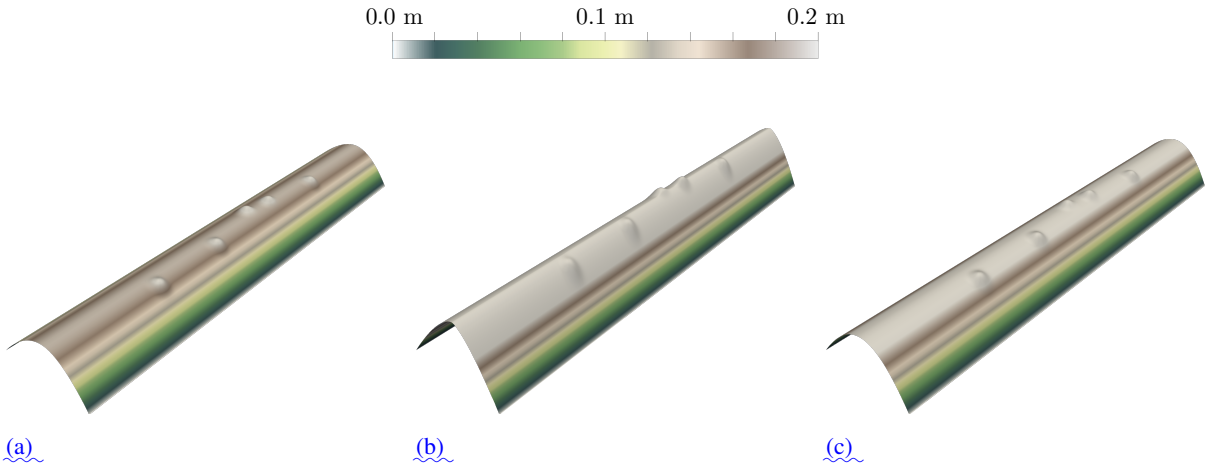

Figure 6. Sediment height h_s^{ex} of the analytic solution for the case k_g=5 km^2.My^{-1} and k_w=5 km^2.My^{-1}. a: r_s=1, p_s=0, b: r_s=3/2, p_s=1, c: r_s=2, p_s=0

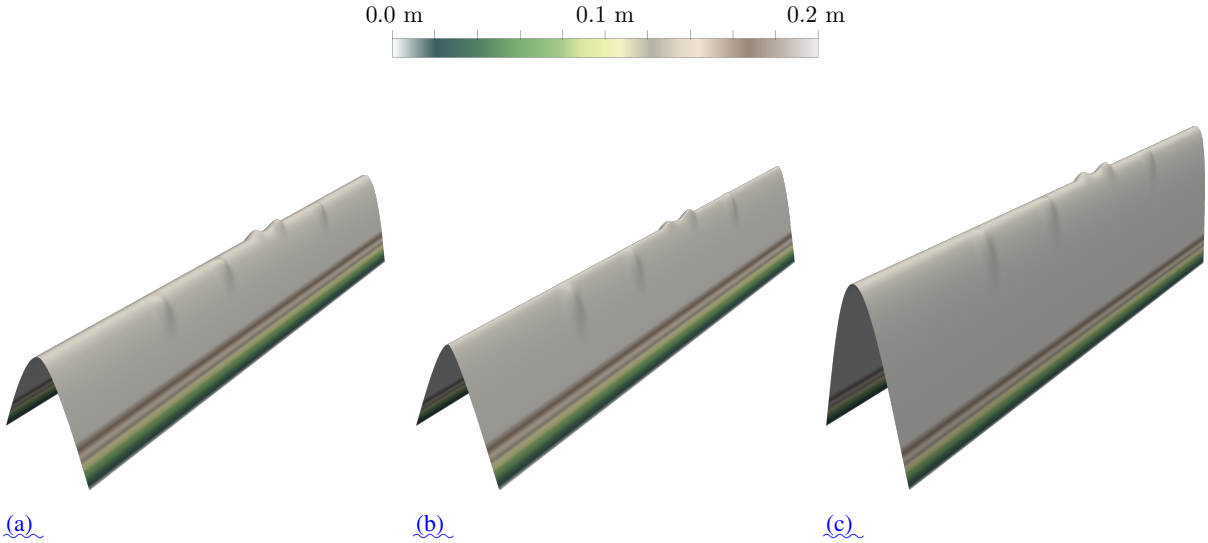

Figure 7. Sediment height h_s^{ex} of the analytic solution for the case k_g=1 km^2.My^{-1} and k_w=5 km^2.My^{-1}. a: r_s=1, p_s=0, b: r_s=3/2, p_s=1, c: r_s=2, p_s=0

~~whose main role is to ensure that the sediment height h_s remains positive. In the following we use:~~

$$\eta_s(u) = \begin{cases} 1 - \dfrac{h_*}{u + h_*} & \text{if } u \geq 0, \\ 0 & \text{otherwise} \end{cases}$$

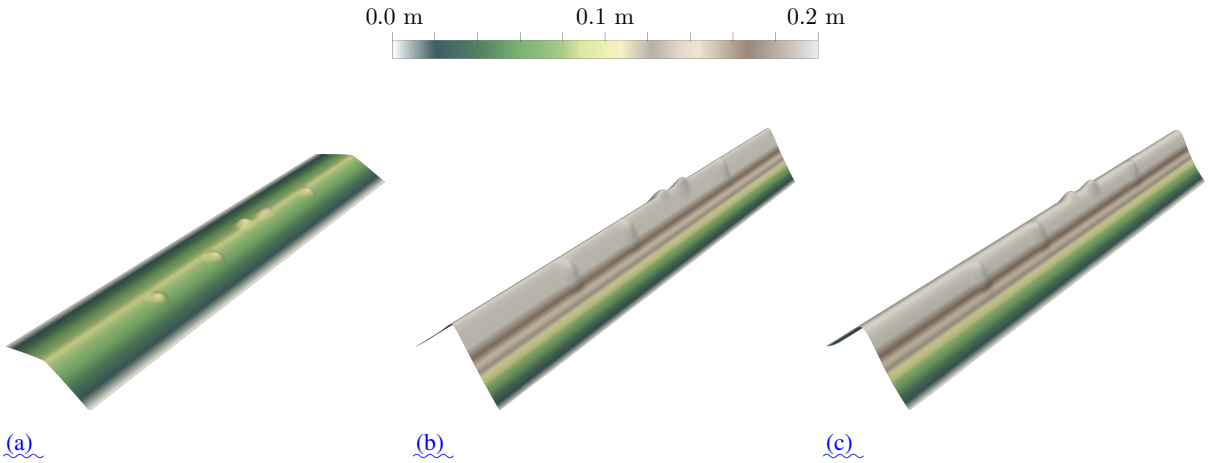

Figure 8. Sediment height h_s^{ex} of the analytic solution for the case k_g=1 km^2.My^{-1} and k_w=50 km^2.My^{-1}. a: r_s=1, p_s=0, b: r_s=3/2, p_s=1, c: r_s=2, p_s=0

with ~~h_s~~p_s we have considered. All those simulations have been performed in parallel on 108 processors through the use of the MPI library.

On figure **??**, we present the obtained convergence curves for all the tested analytic solutions, i.e. we plot the standard L^2 error measuring the difference between the simulated sediment height and the exact analytic sediment height. We see on figure **??** that for all configurations except the case (k_g=1 ~~cm. We consider here the most common form for functions ψ_w and ψ_g corresponding to:~~

$$\psi_w(u) = \int_0^u k_w(v)dv \quad \text{and} \quad \psi_g(u) = \int_0^u k_g(v)dv,$$

~~where~~ km^2.My^{-1}, k_w ~~and k_g are diffusion coefficients such that :~~

$$0 \leq k_g^- \leq k_g(u) \leq k_g^+ < +\infty \quad \text{and} \quad 0 \leq k_w^- \leq k_w(u) \leq k_w^+ < +\infty,$$

~~in such a way that:~~

$$\nabla\psi_w(h_s+b) = k_w(h_s+b)\nabla(h_s+b) \quad \text{and} \quad \nabla\psi_g(h_s+b) = k_g(h_s+b)\nabla(h_s+b),$$

~~so that the sediment flux follows the topographic slope $\nabla(h_s+b)$. This sediment flux model is implemented in our modeling platform ArcaDES (?) (although ArcaDES is mentioned for the first time in a scientific paper, it is used since 2015 in the stratigraphic numerical forward model DionisosFlow™ initially developed by ?). Both soil erosion and sediment deposition are considered. As ArcaDES is tailored for large time and space scales simulations, this is the reason why we have chosen to express~~

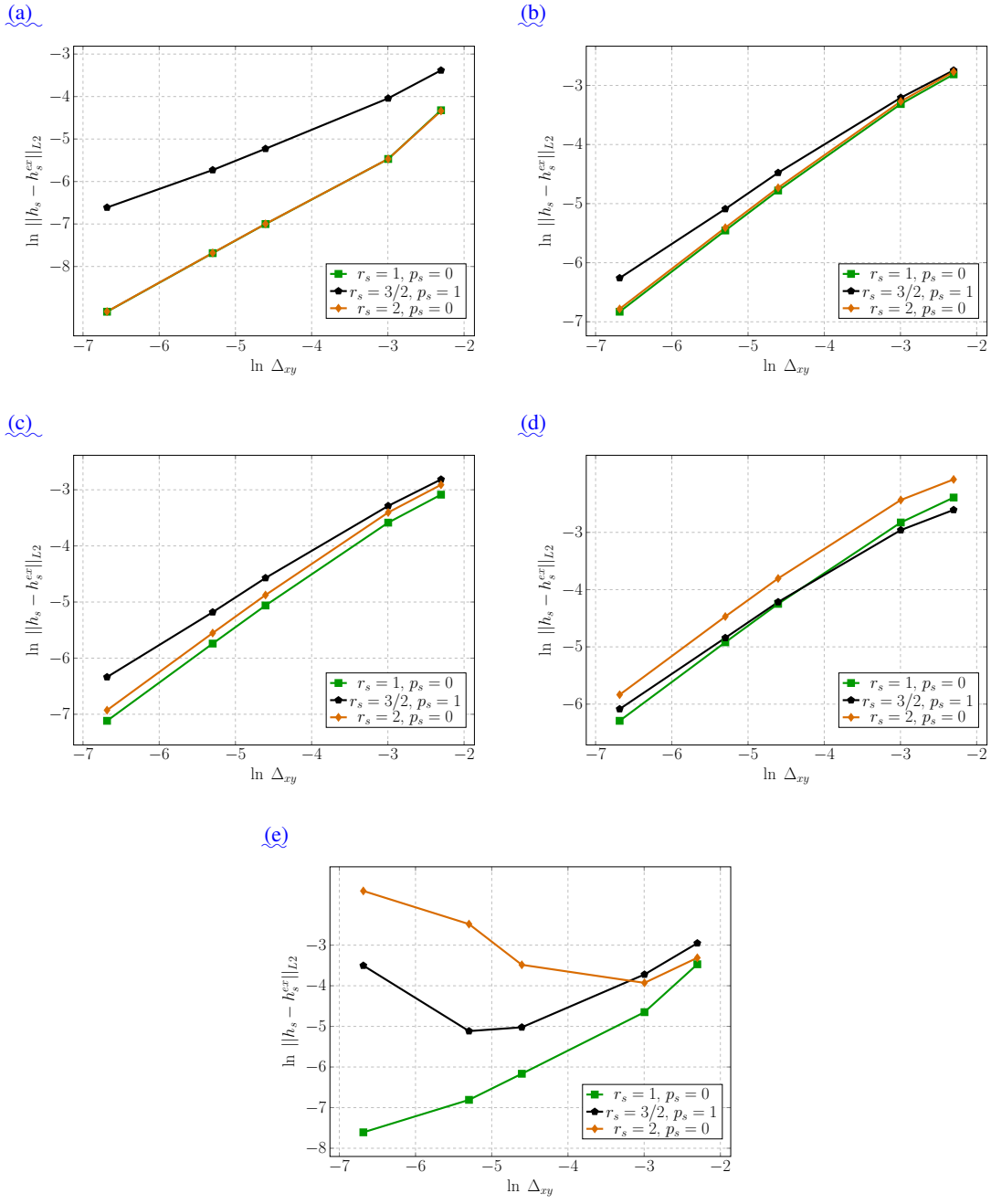

Figure 9. Convergence curves. a: case k_g=50 km^2.My^{-1} and k_w=1 km^2.My^{-1}. b: case k_g=5 km^2.My^{-1} and k_w=1 km^2.My^{-1}. c: case k_g=5 km^2.My^{-1} and k_w=5 km^2.My^{-1}. d: case k_g=1 km^2.My^{-1} and k_w=5 km^2.My^{-1}. e: case k_g=1 km^2.My^{-1} and k_w=50 km^2.My^{-1}

Table 1. Approximate maximum analytic value of $\tau = \frac{k_w}{k_g}\left(\frac{q_w}{q_{ref}}\right)^{r_s}$ for each convergence test

	$(r_s$=1,p_s=0)	$(r_s$=3/2,p_s=1)	$(r_s$=2,p_s=0)
(k_g,k_w)=(50,1) km^2.My^{-1} ~~.km^{-1} and thus we naturally set q_{ref}~~	0.01	0.00353	0.0025
(k_g,k_w)=(5,1~~m^3.s~~) km^2.My^{-1} ~~.km^{-1}. The natural unit of coefficients~~	0.1	0.0353	0.025
(k_g~~and~~,k_w)=(5,5) km^2.My^{-1}	0.5	0.353	0.25
(k_g,k_w~~is km~~)=(1,5) km^2.My^{-1}	2.5	1.767	1.25
(k_g,k_w)=(1,50) km^2.My^{-1} ~~, with the reference slope again set to s_{ref}~~	25	17.67	12.5

~~the xy coordinates in kilometers (km), time in million years (My), sediment height h_s and basement b in meters (m). Thus the unit of sediment sources will be meters per million years (m.My= 50 km^2.My^{-1}). Since we have chosen to use $Q_w = q_w$ with q_w the water flux from , the unit for the water discharge q_w is m^3. s~~), we obtain clean convergences curves, assessing the correctness of our numerical scheme even for the non-linear couplings. However, for the case (k_g=1 ~~m.km~~km^2.My^{-1}~~.~~

3.1 ~~Numerical issues with non linear coupling of overland flow and sediment erosion and transport~~

~~From ?, we know that for sublinear to linear coupling, i.e. $r_s \leq 1$ no chaotic behavior is expected, as is confirmed by numerical experiments. However as soon as $r_s > 1$~~ , k_w= 50 km^2.My^{-1}) the two non-linear couplings (r_s=3/2,p_s=1) and (r_s=2,p_s=0) fail to converge. Looking at table **??** where we regroup the value of τ for each test case using the knowledge of the exact solution, we see that convergence problems appear as expected when τ becomes large. Indeed, since the error increases when we refine the mesh, this error is not a discretization consistency error as moreover all the other test cases validate both our implementation and discretization. On the contrary it increases with the size of the numerical systems, which strongly suggests that it originates from solver (both linear and non-linear) errors, and this perfectly illustrates the phenomenon of numerical errors self-amplification ~~mechanism is expected leading to highly non linear behaviors and complex topographies. This is precisely the domain we explore in this section.~~ that we have discussed from the theoretical point of view in the section **??**. Another reason for which problems are probably more severe with finer meshes is that numerical diffusion which is much smaller than the true physical diffusion in view of the values of k_g adds nevertheless enough additional smoothing for large values of Δ_{xy} to dissipate large parts of the numerical errors while this is no longer the case for the finer meshes.

Now, to illustrate how treacherous those numerical solutions are, we present on figures **??** and **??** a comparison between the analytic solution and its erroneous numerical counterpart.

The erroneous solutions are dangerously "good looking": indeed, if only the initial topography and the rain and production data are shown, one could easily be tempted to interpret the quite complex topographies obtained as the realistic self-amplification of the perturbations due to the presence of the bumps. However since we know the exact solution, we are sure that this is not the case: the appealing numerical solutions are completely wrong. The overall "geologically realistic" look of the erroneous

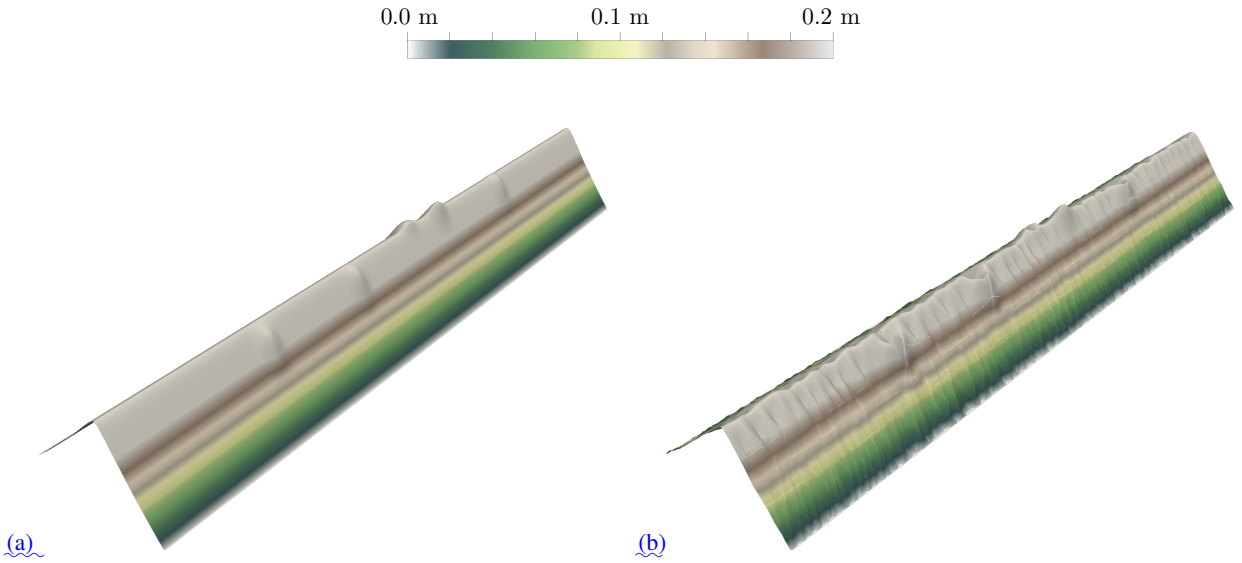

Figure 10. Comparion between the sediment height h_s^{ex} of the analytic solution and numerical solution h_s for the case k_g=1 km^2.My^{-1}, k_w=50 km^2.My^{-1}, $r_s = 3/2$ and p_s=1. a: Analytic solution h_s^{ex}, b: numerical solution h_s

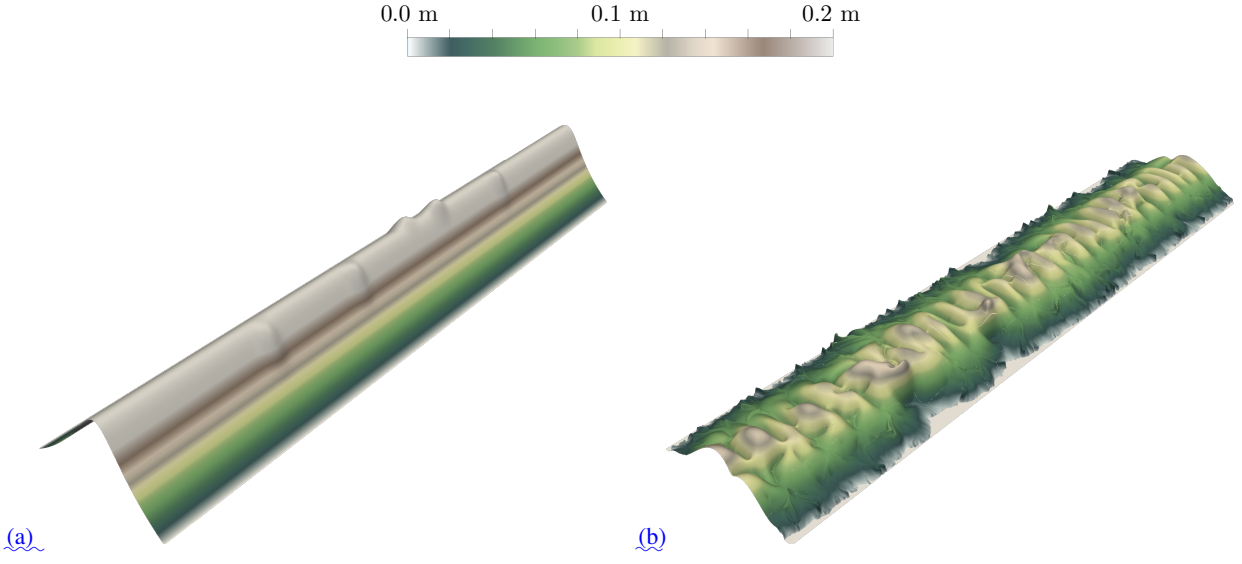

Figure 11. Comparion between the sediment height h_s^{ex} of the analytic solution and numerical solution h_s for the case k_g=1 km^2.My^{-1}, k_w=50 km^2.My^{-1}, $r_s = 2$ and p_s=0. a: Analytic solution h_s^{ex}, b: numerical solution h_s

solution comes from the fact that numerical noise is amplified not by some numerical scheme deficiency but by the capacity of our continuous model to amplify perturbations that we described in the previous section. In other words, the numerical noise is reworked by the system, giving a "realistic" look to it. This is the reason why we stress that when performing real-life simulations for which of course the correct solution is unknown (otherwise we would not need to simulate anything at all), it can become very hard to decide if the numerical results are correct or blurred by realistic looking amplified numerical noise. The quality of the numerical scheme, although essential, is not in question: the issue is the self-amplification mechanisms of the continuous model. They are the reason for its physical interest but simultaneously its main issue for performing reliable simulations.

3.1 Identifiable instabilities in a non analytic case

As mentioned in the introduction ~~, in the absence of~~ and above, in real applications one does not have a reference analytic solution and it is in general hard on complex topographies to decide whether a numerical solution of (**??**) is correct or not. To illustrate how one can sometimes partially circumvent this difficulty, we consider a simple synthetic topographic surface defined by three constant slope planes. The numerical domain is rectangular with the dimensions $Lx = 400$ km in the x axis and $Ly = 300$ km in the y axis (see Fig. **??**-a,**??**-b). ~~The mesh size is~~ We use again a cartesian mesh with square cells, the edges of each cell being of length $\Delta_{xy} = 2$ km. The gravity diffusion coefficient k_g is equal to 100 km^2.My^{-1} in the whole domain while $k_w = 10$ km^2.My^{-1} for $h_s + b \geq 0$ and $k_w = 0.1$ km^2.My^{-1} for $h_s + b < 0$, corresponding to a modulation of the water induced transport in a fictitious marine domain. Water is supplied by three constant water-flux sources located at the domain boundary (black arrows in Fig. **??**-a), so we call this "three rivers" test case. Each water source is 12 km large and supplies 1200 m^{3}s^{-1} of water.

An essential remark is that the whole configuration is ~~symmetrical~~ symmetric with respect to the vertical plane $x = Lx/2$, including the cartesian mesh used for this simulation. In principle, the equation system consisting of (**??**) and (**??**), here used with $r_s = 2$, $p_s = 1$, ~~p_w=0 and k_m=1 m.s^{-1}~~ should maintain this symmetry. ~~Therefore symmetry will be our main tool to evaluate solution quality~~Since we do not know this time the exact solution, at least we can use symmetry to identify erroneous results that do not fulfill this elementary requirement. Using the finite volume scheme depicted in section **??**~~which for water flow corresponds to using the consistent water flux obtained from~~ , we perform a set of three identical simulations in terms of physical parameters but using different numerical settings in order to illustrate the impacts of numerical errors. For simplicity, the cartesian mesh shares the symmetry of the problem, to avoid any additional symmetry approximation error. We perform a sequential computation using GMRES as linear solver for all systems, its parallel equivalent on 4 processors and another sequential simulation using BiCGStab as linear solver for all systems. The linear solvers are part of the well-known and reference PETSc library (**?**) to avoid any potential mistake in their implementation, while the parallelism relies on the Arcane framework (**?**). Final topographies and water flux are shown on the bottom row of Fig. **??**. Figure **??**-c corresponds to sequential GMRES, Fig. **??**-d to parallel GMRES and Fig. **??**-e to sequential BiCGStab.

All the results from these simulations should be almost identical and in any case symmetrical with respect to the vertical plane

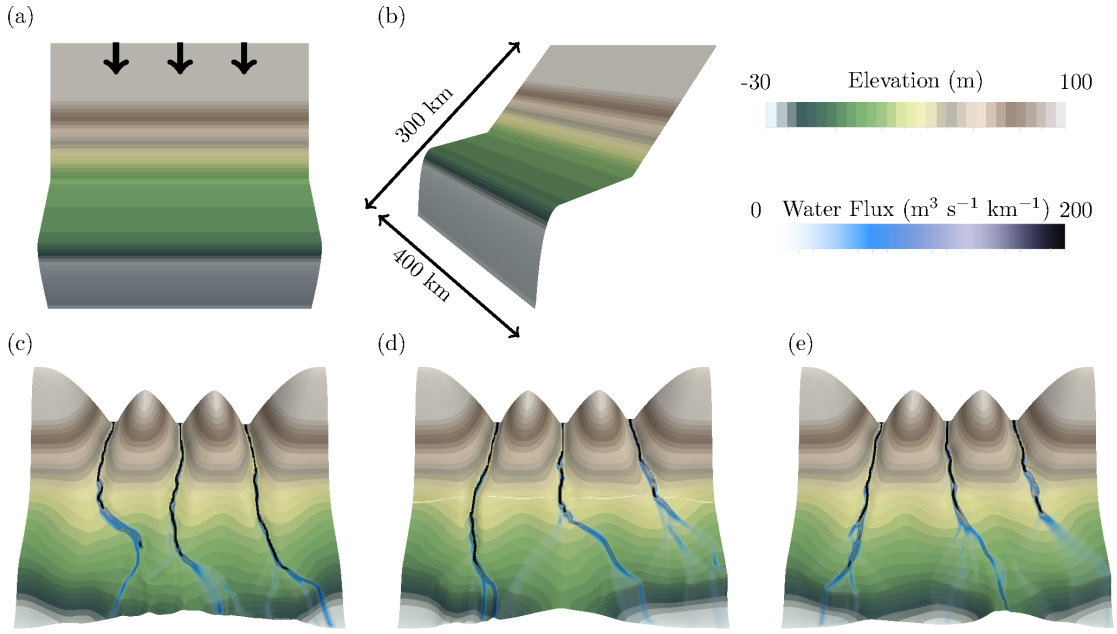

Figure 12. The "three rivers" test case with Δ_{xy}=2 km. a-b : Initial topography, black arrows represent the position of the water inflows. Bottom row : topography and water flux after 6 My obtained under different numerical settings. c: sequential GMRES, d: parallel GMRES, e: sequential BiCGStab

$x = Lx/2$ in absence of any spatial heterogeneity in the input data. Clearly, symmetry is lost in the three cases and what is even more striking is that we get three very different results. The only difference between the three cases being the numerical solvers, this indicates that this has originated from numerical errors. As we are using a decoupled time scheme between water flow and sediment evolution (see section **??**), one may argue that those instabilities are arising from some violated coupling constraint on the time step. Should this be the case, reducing the time step enough would ultimately lead to clean solutions. However, we have observed the exact opposite: the smaller the time step is, the larger are the obtained instabilities. The fact that reducing the time step makes things even worse is thus another clear sign that our problems are the result of amplified error accumulation ~~. Finally if the same experiments are performed with $r_s \leq 1$ then this time the symmetry is maintained and all three solutions are almost identical however small the time step might be, which clearly indicates that the non-linearity of the coupling for $r_s > 1$ is responsible of the observed chaotic behavior. Our interpretation is that small numerical perturbations are rapidly amplified by the model~~ up to the point that ~~they become of the same order of magnitude that the originally dominant part of the solution, and do influence~~ it influences flow branching. ~~From the modeling perspective the model behaves as expected in the sense that small perturbations are amplified and strongly impact the final result. However in our simulations no heterogeneity is present in data thus this phenomenon should not spontaneously occur: the non-physical numerical errors are amplified up to the point that the numerical solution is no longer a reasonable approximation. This clearly also implies that the numerical schemes must~~

~~be as precise as possible to reduce the numerical noise. In particular it is mandatory to use our consistent MFD discretization of rather than the non consistent flow routing algorithms of the literature~~

4 Large structures simulation (LSS): an attempt to get rid of instabilities in LEMs

In this section, we explain how to transpose the ideas underlying the concept of large eddy simulation from the computational fluid dynamics community to our landscape evolution model. In our opinion, this is a key ingredient for achieving reproducible LEM simulations.

4.1 Principles and physical interpretation of filtering

Recall that the main idea of LES is to filter the solution to distinguish between the behavior of the flow above and below the target length scale, to obtain local averages that are smoother and as mesh independent as possible. This target length scale controls the size of the smallest structures that we will be able to resolve in the problem, quite independently of the domain size. The main practical consequence is that our mesh will have to resolve this length scale, i.e. the mesh size ε will have to be smaller than the chosen length scale.

LES filters/models are probably as numerous as the various authors working on the subject (**?**), thus we will very brief on the subject and refer the reader to a the quite recent review **?**. The very first LES model is called the Leray-α model. It was used by Leray in 1934 to establish existence of weak solutions to the Navier-Stokes equations (**?**). Originally, the filtering in **?** as well as in many classical LES models was achieved by using a convolution operator $\mathcal{F}$ defined by:

$$\mathcal{F}(u)(\boldsymbol{x}) = \int_{\mathbb{R}^d} u(\boldsymbol{y}) g_\delta(\boldsymbol{x}-\boldsymbol{y}) d\boldsymbol{y}, \quad \text{where} \quad g_\delta(\boldsymbol{x}) = \frac{1}{\delta^d} g\left(\frac{\boldsymbol{x}}{\delta}\right),$$

where the filter kernel g satisfies:

$$0 \leq g(\boldsymbol{x}) \leq 1, \qquad g(\boldsymbol{0}) = 1, \qquad \int_{\mathbb{R}^d} g(\boldsymbol{x}) d\boldsymbol{x} = 1.$$

Several kernels are used in the literature, such as a low-pass filter, a box-filter or the very natural Gaussian filter $g(\boldsymbol{x}) = \pi^{-d/2} e^{-|\boldsymbol{x}|^2}$.

In figure **??** we illustrate the smoothing effect of a Gaussian kernel on an oscillating data: as expected, it preserves the high amplitude and low frequency oscillation while filtering out the high frequency and low amplitude oscillations. Such filters might therefore be ideal for our application to landscape evolution models: the small topographic perturbations will be cleaned out such that the flow routing will not be affected by it. Although convolution operators produce averages with the desired properties, they are impractical on bounded domains. The modern way of defining the Leray-α filter for bounded domains

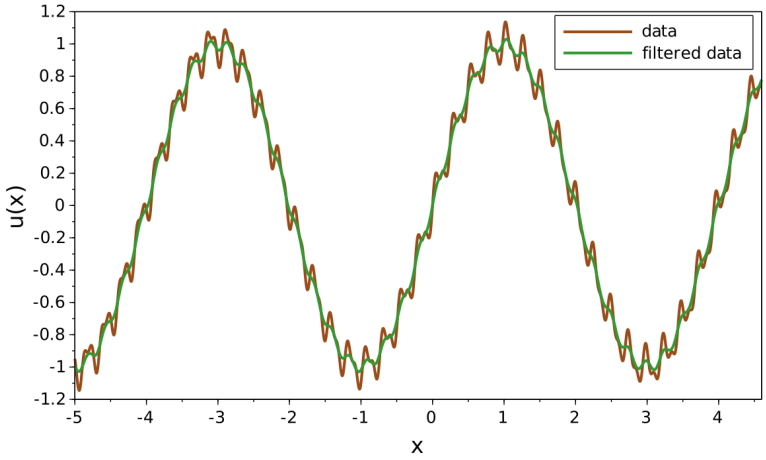

Figure 13. Illustration of the effect of the convolution by a Gaussian function

consists in using the differential filter $\mathcal{F}_\alpha$ defined by (**??**):

$$\left|\begin{array}{ll} -\alpha^2\Delta\mathcal{F}_\alpha(u)+\mathcal{F}_\alpha(u)=u & \text{in } \Omega, \\ \nabla\mathcal{F}_\alpha(u)\cdot\boldsymbol{n}=0 & \text{on } \partial\Omega_{\mathcal{N}}, \\ \mathcal{F}_\alpha(u)=0 & \text{on } \partial\Omega_{\mathcal{D}}. \end{array}\right. \tag{17}$$

The filtered result $\mathcal{F}_\alpha(u)$ basically amounts to a convolution of u by the underlying Green's function (**??**), i.e. the filter applied to the Dirac distribution. Using a finite volume scheme $\mathcal{F}_\alpha$ we can this time easily obtain a discrete version $\mathcal{F}_{\alpha,h}$ which is one of the main reasons why we have chosen to use this filter, along with its theoretical and practical success for CFD. Notice that contrary to **??**, we use homogeneous Neumann and Dirichlet boundary conditions instead of periodic boundary conditions to simplify the treatment of the boundary. The main drawback of this choice is that our filter does not commute with differential operators. Resorting to only Dirichlet boundary conditions would have solved this issue, however from our numerical experiments we found that this can create boundary effects unless the chosen Dirichlet boundary condition is adapted to the filtered quantity. The Neumann choice avoids those difficulties without creating any practical issues, which has motivated our choice. For quantities such as the water flux for which Neumann everywhere is a more natural boundary condition, we introduce the alternative filter $\mathcal{F}_\alpha^{\mathcal{N}}$ with only Neumann boundary conditions:

$$\left|\begin{array}{ll} -\alpha^2\Delta\mathcal{F}_\alpha^{\mathcal{N}}(u)+\mathcal{F}_\alpha^{\mathcal{N}}(u)=u & \text{in } \Omega, \\ \nabla\mathcal{F}_\alpha^{\mathcal{N}}(u)\cdot\boldsymbol{n}=0 & \text{on } \partial\Omega. \end{array}\right. \tag{18}$$

4.2 Leray filtering applied to our landscape evolution model

From the numerical observations that the model governing the simultaneous evolution of sediment and water seems for large values of τ as intractable to solution as the Navier-Stokes system is for large Reynolds numbers, following the idea of LES we

~~abandon the idea of resolving all the scales involved in the landscape evolution problem and will only try to simulate the large sedimentary and water structures. In practice, this~~ will now apply filtering to key parts of our model problem to obtain a more numerically stable approximate model. This means that the sediment flux used in the mass conservation equations:

$$\left|\begin{array}{ll} \dfrac{\partial h_s}{\partial t} + div\,(\boldsymbol{J}_s) = S_s & \text{in } \Omega\times]t_0,T[, \\ -\boldsymbol{J}_s\cdot\boldsymbol{n} = B_s & \text{on } \partial\Omega_{\mathcal{N}}\times]t_0,T[, \\ h_s = 0 & \text{on } \partial\Omega_{\mathcal{D}}\times]t_0,T[, \\ h_s(t=t_0) = h_{s,0} & \text{in } \Omega, \end{array}\right.$$

will now be given by:

$$\boldsymbol{J}_s = -\eta_s(h_s)s_{ref}^{-p_s}||\nabla(h_s+b)||^{p_s}\left(\left(\frac{\mathcal{F}_\alpha^{\mathcal{N}}(q_w)}{q_{ref}}\right)^{r_s}\nabla\psi_w(h_s+b)+\nabla\psi_g(h_s+b)\right) \quad \text{in } \Omega\times]t_0,T[, \tag{19}$$

where we use the filtered water flux magnitude $\mathcal{F}_\alpha^{\mathcal{N}}(q_w)$ instead of directly using the water flux q_w. In the same way, in the water equations, we will now use the filtered topography $\mathcal{F}_\alpha(h_s+b)$ instead of the topography h_s+b, leading to:

$$\left|\begin{array}{ll} -div\left(k_m h_w\eta_w(h_w)s_{ref}^{-p_w}||\nabla(\mathcal{F}_\alpha(h_s+b))||^{p_w}\nabla(\mathcal{F}_\alpha(h_s+b))\right) = S_w & \text{in } \Omega, \\ -k_m h_w\eta_w(h_w)s_{ref}^{-p_w}||\nabla(\mathcal{F}_\alpha(h_s+b))||^{p_w}\nabla(\mathcal{F}_\alpha(h_s+b))\cdot n = B_w & \text{on } \partial\Omega, \end{array}\right. \tag{20}$$

with the associated water flux:

$$q_w = ||k_m h_w\eta_w(h_w)s_{ref}^{-p_w}||\nabla(\mathcal{F}_\alpha(h_s+b))||^{p_w}\nabla(\mathcal{F}_\alpha(h_s+b))||. \tag{21}$$

Our ~~"reproducible"~~ so-called large structures simulation (LSS) for landscape evolution thus consists in solving (**??**)-(**??**)-(**??**)-(**??**). The name "large structures" originates from the fact that since we use filtering in the coupling process, the water model does not see anymore topographic details that are smaller than α, and in the same way the sediment evolution is no longer influenced by water flow details smaller than α. We have thus abandoned the idea of resolving all the scales involved in the landscape evolution problem and will only try to simulate the large sedimentary and water structures, hence the name LSS: only structures several times larger than the filter resolution α will appear in the final result.

4.3 Numerical results with filtering

~~We reproduce the very same experiment that was performed at the beginning of this section on the~~ Before turning to numerical experiments, one has to choose a value for the filter parameter α. Following LES principles, we know that the filter scale α corresponds to the spatial resolution of our continuous approximate model, that in practice one will want to be as small as possible. However it must naturally be resolved by the grid resolution, meaning we should have at the very least $\Delta_{xy} < \alpha$ for cartesian grids. Moreover, as we test our numerical solution against an analytic solution for the unfiltered case, we need to make the filter size go to zero at the same speed than the mesh size in order to measure a convergence. For simplicity, we

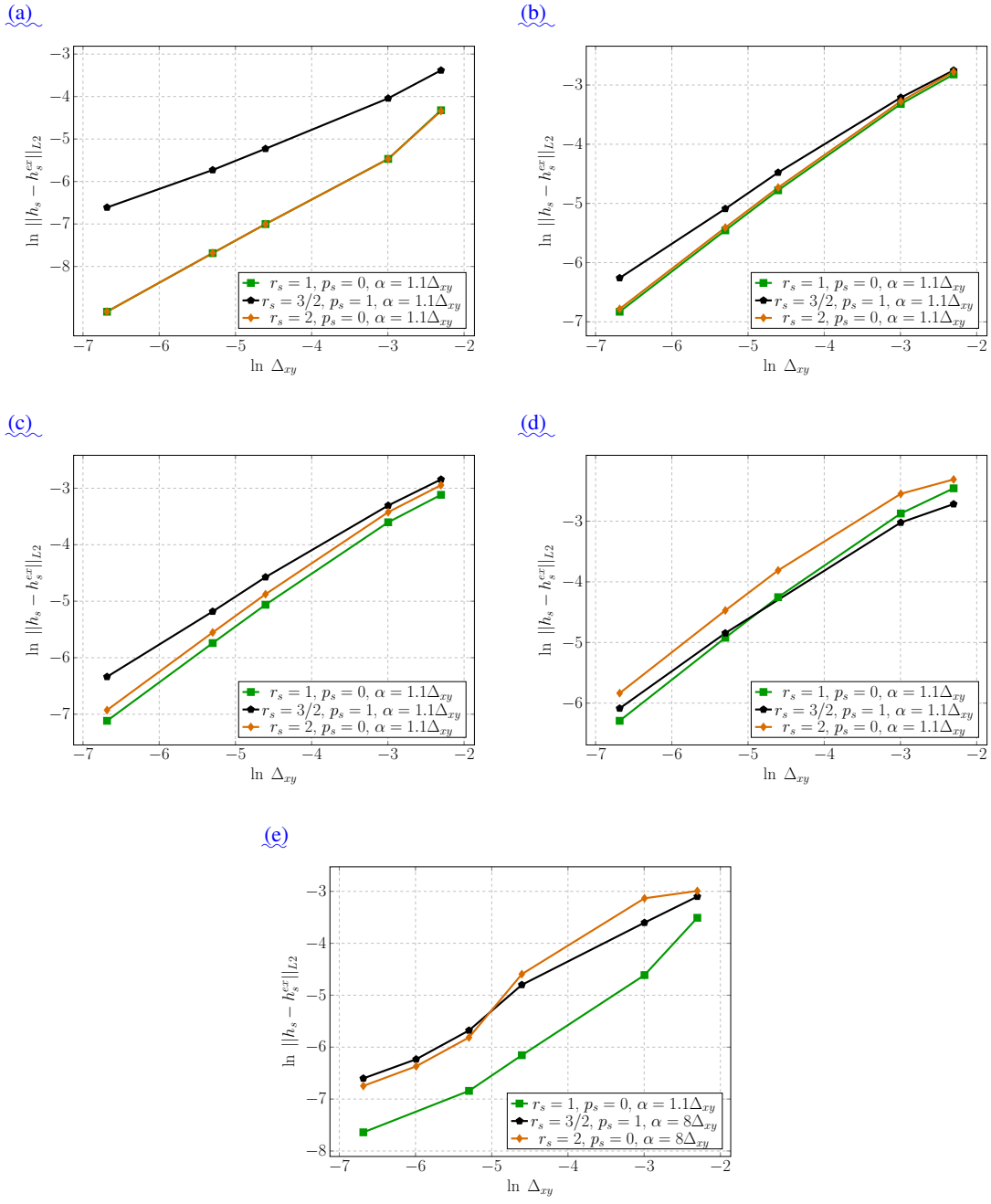

Figure 14. Convergence curves with filters. a: case k_g=50 km^2.My^{-1} and k_w=1 km^2.My^{-1}. b: case k_g=5 km^2.My^{-1} and k_w=1 km^2.My^{-1}. c: case k_g=5 km^2.My^{-1} and k_w=5 km^2.My^{-1}. d: case k_g=1 km^2.My^{-1} and k_w=5 km^2.My^{-1}. e: case k_g=1 km^2.My^{-1} and k_w=50 km^2.My^{-1}

have chosen to use filter parameters $\alpha = \gamma\Delta_{xy}$ with $\gamma > 1$. On figure **??** we present the convergence results obtained for the analytic test cases of section **??** this time using filters. Convergence is recovered with $\alpha = 1.1\Delta_{xy}$ (i.e. $\gamma = 1.1$) for every case that was already working without filter, suggesting that the LSS approach at least does not deteriorate correct results previously obtained. We also see that for the test cases with (k_g=1 km^2.My^{-1}, k_w=50 km^2.My^{-1}) convergence is now obtained for α= $8\Delta_{xy}$ (γ = 8). This choice for the ratio γ between the filter size α and the mesh size Δ_{xy} is not random. Indeed, with $\alpha = \gamma\Delta_{xy}$ when Δ_{xy} tends to zero so does the filter size and if γ is not large enough then the filtering parameter α will no longer be large enough to compensate for solver errors and numerical approximation errors. We illustrate this on figure **??**.

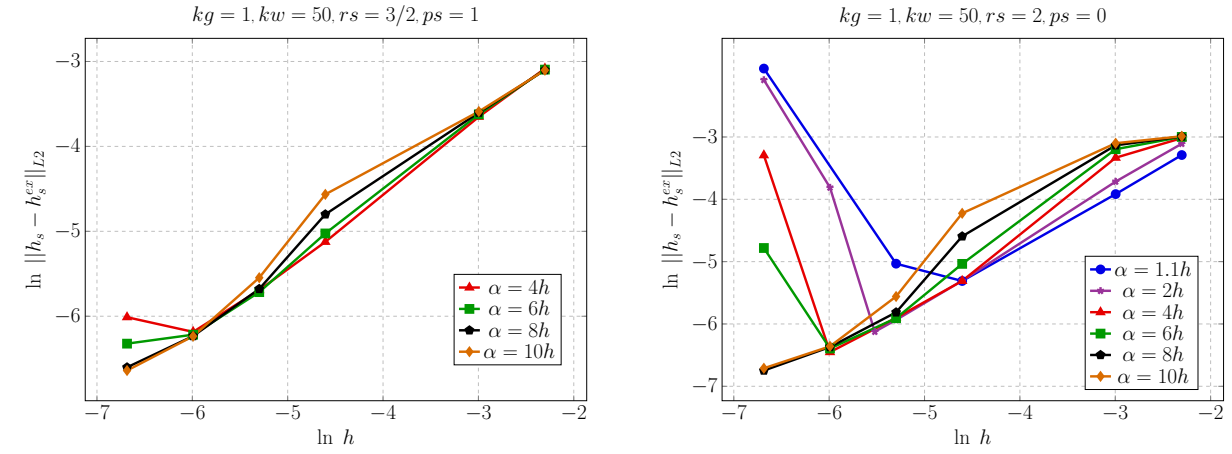

(a) (b)

Figure 15. Convergence curves for various values of the ratio α/Δ_{xy}. a: (r_s,p_s)=(3/2,1), b:(r_s,p_s)=(2,0)

Keeping in mind that we are necessarily using a fixed Newton non linear solver tolerance (1e-6 in practice) what we observe on those curves is that when the parameter α becomes smaller than some threshold value that allows to control the corresponding accumulated solver (and numerical approximation) errors, the obtained solution is no longer correct. Of course, with a larger value of γ this threshold is reached for a smaller value of Δ_{xy} which explains why once γ is large enough we can obtain the correct solution along the entire convergence curve. This threshold is likely to depend on Δ_{xy}, in the sense that for finer meshes since the size of the system is larger, so is the solver error. It is also very likely that since we expect larger values of τ to imply an increase in both the numerical approximation and solver errors, modifying τ might also probably influence this threshold value. Nevertheless the results of figure **??** exlain why we have presented results with γ =8 on figure **??**: to get a correct approximation even for the finer meshes and thus a clean convergence curve. We nevertheless see on figure **??** that for more realistic mesh sizes, smaller values of γ will be more than enough to obtain the correct solution, and that using filters is not prohibitively costly in realistic configurations. We also observe that for mesh sizes allowing all the values of the ratio to γ to give a correct approximation, the error of course increases with γ, which is perfectly expected since α is our largest approximation parameter.

We finally reproduce the very same experiment that was performed on the "three rivers" test case, with sequential GMRES, parallel GMRES and sequential BiCGStab, but using a filter ~~α = 2.2 km~~ α= 2.2 km for Δ_{xy}=2 km. Contrary to Fig. **??**, the symmetry is maintained and we obtain almost identical results for the three configurations **??**. The expected impact of the filter on the simulated water flow and topography is a smoothing effect, which is what is observed when comparing for example the width of the three valleys. However, the differences remain marginal in this case.

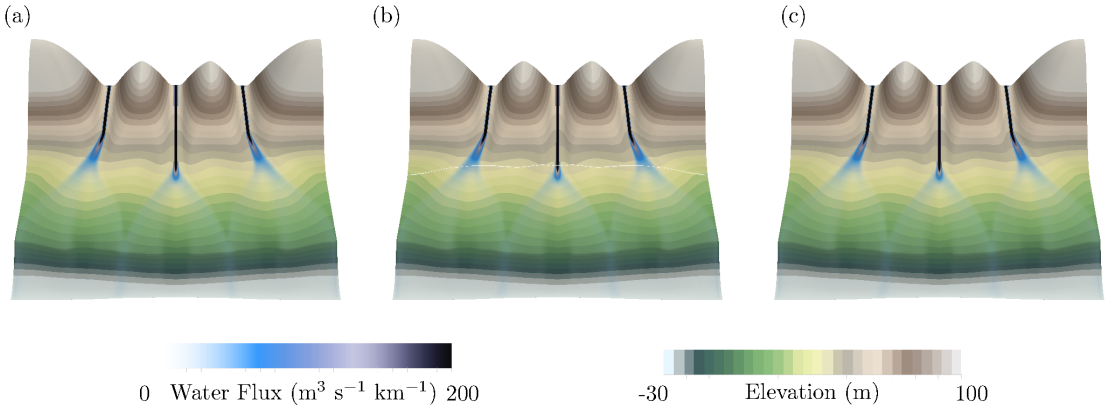

Figure 16. The "three rivers" test case with filter α= 2.2 km and Δ_{xy}=2 km. Topography and water flux after 6 My. a: sequential GMRES, b: parallel GMRES, c: sequential BiCGStab

~~Following LES principles, the filter scale α corresponds to the spatial resolution of our continuous model, which must naturally be resolved by the grid resolution, meaning we should have at the very least $\Delta_{xy} < \alpha$ for cartesian grids (and more generally $c < \alpha$ for a general mesh recalling that $c = \sqrt{2}\Delta_{xy}$ for cartesian meshes). To assess the legitimacy of this condition, still~~ Still on our "three rivers" test case~~we first fix the grid size to Δ_{xy}=2 km and observe the~~ , from our observations on the analytic cases and as we do not know the exact solution, to assess the legitimacy of our choice of filter size we analyze the behavior of the solution for various values of the filter parameter α (fixing the grid size to Δ_{xy}=2 km). Results are displayed Fig. **??**. We clearly see that symmetric solutions are obtained for ~~$\alpha \geq \Delta_{xy}$~~$\alpha > \Delta_{xy}$, while further reducing the filter parameter leads to behavior similar to the no filter case. This is first coherent with the principle of LES that the filter should control what happens below the grid scale, which can only be done if $\alpha > \Delta_{xy}$~~.~~ , and also a clear sign that our initial choice for the ratio $\gamma = \alpha/\Delta_{xy}$ belongs to the stable region.

4.4 Impacts of ~~water flow consistency and~~ filtering on the emergence of geomorphic structures

~~The three rivers synthetic case has highlighted the absolute necessity of considering a filtering strategy in LEMs using a MFD/SFD water flow algorithm. We now switch on a second synthetic case study~~ We now consider two synthetic case studies to observe the formation of geomorphic features. The idea underlying the first test case is very simple: we re-use as our initial

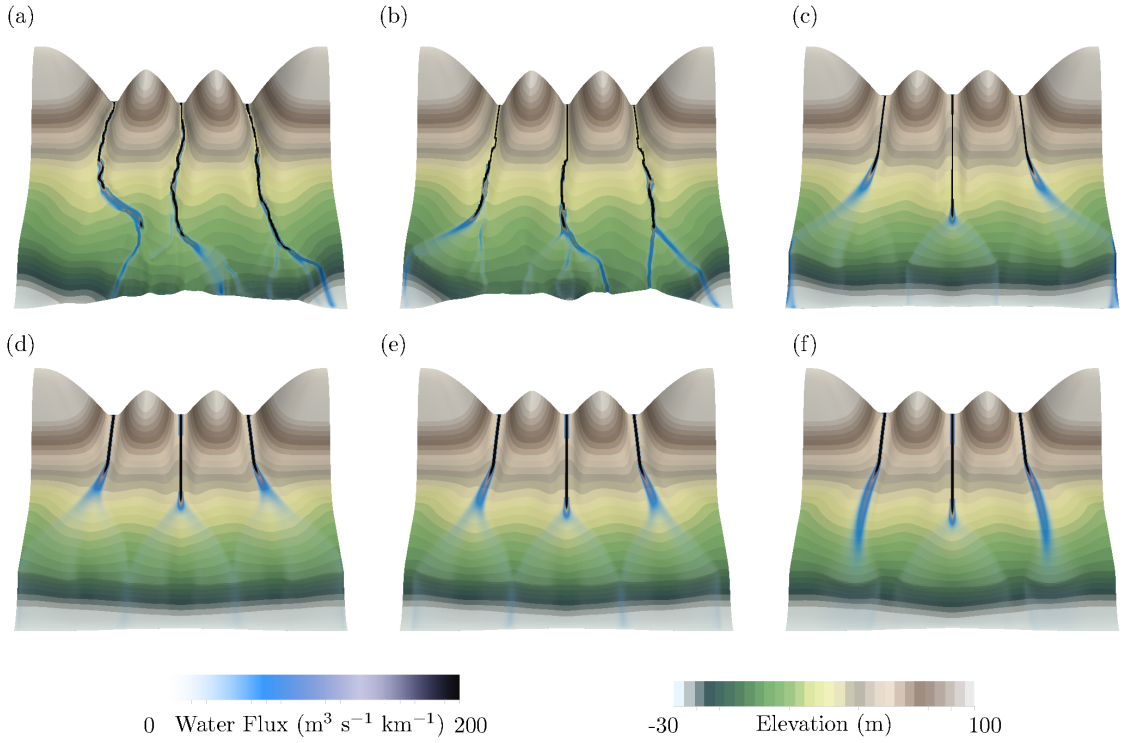

Figure 17. The "three rivers" test case with Δ_{xy}=2 km. Final topography and water flux after 6 My obtained with different values of the filter parameter α. a: no filter, b: α= 0.2 km, c: α=1 km, d: α= 2.2 km, e: α=2.5 km , f: α= 3 km

data the analytic solution described in section **??** in the case (r_s=2,p_s=0) and (k_g = 1 km^2.My^{-1}, ~~using either a homogeneous or a perturbed initial topography. The characteristics of this test case are relatively close to the models published by **??**.~~ k_w = 50 km^2.My^{-1}) the rectangular domain described in figure **??**. However, instead of using the analytic source terms allowing to recover the analytic solution for all times, we simply use a constant source term (S_s =10 m.My^{-1}, S_w =1 m^3.s^{-1}km^{-2}), corresponding to a uniform constant uplift supply and a uniform constant rain.

We fix the mesh size to Δ_{xy} = 0.005 km, and we again perform the simulation over a time period of 0.25 My with maximum time steps of length Δt = 0.002 My. On figure **??**, we recall the initial elevation corresponding to our analytic solution along with the final solution obtained for our now constant source terms, for various values of the filter size as well as without filters. Since our new source terms are of the same magnitude than the analytic ones and since every other property of the problem is kept the same, we can anticipate using the convergence curves of figure **??** what are the filter sizes giving a correct solution (up to the approximation due to the filtering process itself). Since $\ln \Delta_{xy} \approx$ -5.298, we see on figure **??** that for our choice of Δ_{xy} we can be confident that the filter size $\alpha = 2\ \Delta_{xy}$ will give us the correct solution with a small numerical approximation error, and we use this case as a reference. Thus, the first observation on the result obtained with $\alpha = 2\ \Delta_{xy}$ is that the correct

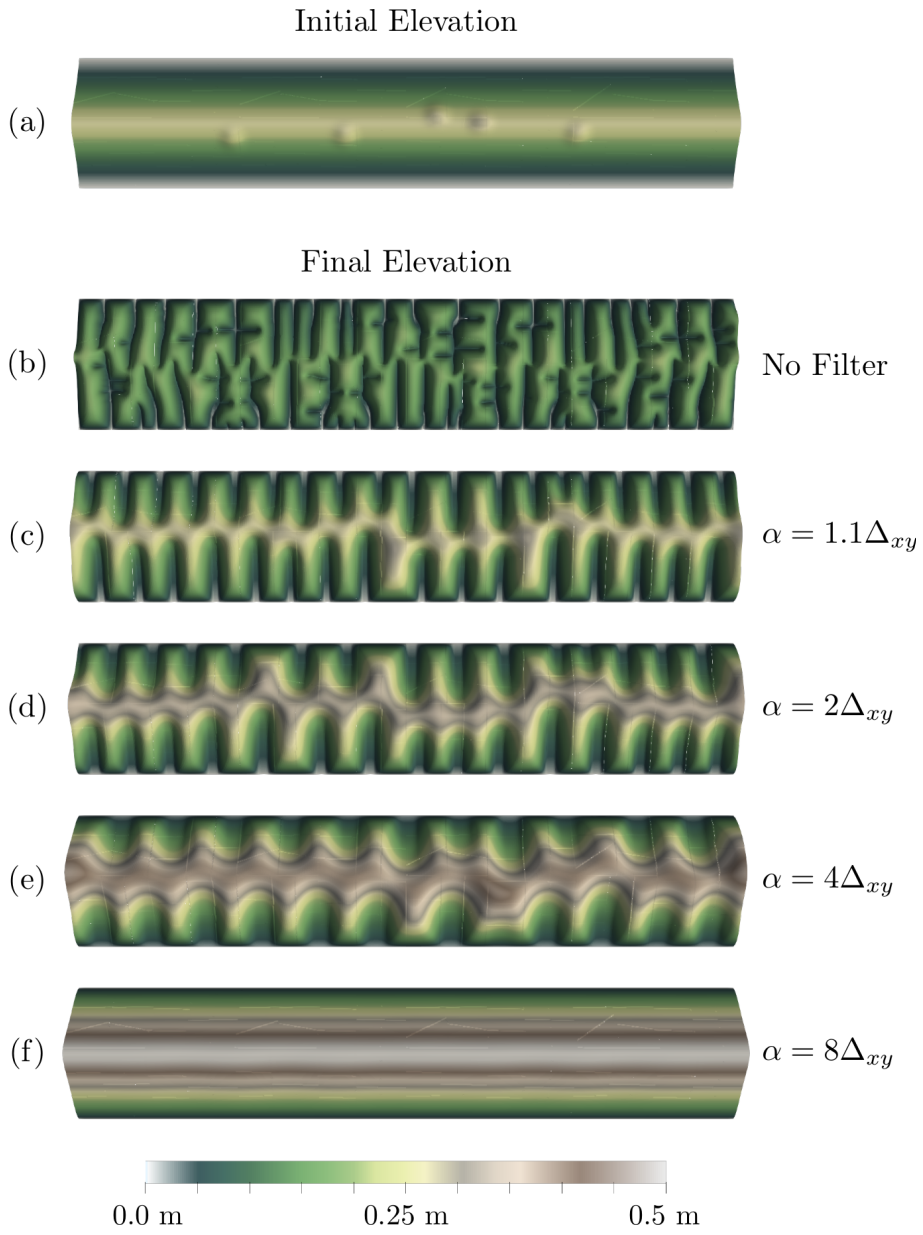

Figure 18. Results for a mesh size Δ_{xy}=5e-3 km. a : Initial elevation. Final elevation : b: no filter, c: $\alpha = 1.1\ \Delta_{xy}$, d: $\alpha = 2\ \Delta_{xy}$, e: $\alpha = 4\ \Delta_{xy}$, f: $\alpha = 8\ \Delta_{xy}$

890 solution this time allows some legitimate geomorphic structures to appear and self organize. Those structures originate from the bumps, as if we perform the very simulation with constant source terms but without bumps, we obtain a clean uniform final state deprived of any geomoprhic complexity. With the larger filter size $\alpha = 4\ \Delta_{xy}$, we obtain an averaged version with

slightly less geomorphic complexity, illustrating the way the filter only keeps "large" structures. However for the very large filter α = 8 Δ_{xy} the approximation for Δ_{xy} = 0.005 km is too crude and we loose all the geomorphic complexity. We have checked that if we refine the mesh we recover the correct solution with the ratio α = 8 Δ_{xy}. This confirms that the uniform crude approximation obtained for α = 8 Δ_{xy} and Δ_{xy} = 0.005 km on figure **??** is as expected due to the fact that we have increased our approximation error too much by oversizing α. Now, let us consider the final solutions of figure **??** for the value α= 1.1 Δ_{xy} as well as without filter. Both of those results present more complexity than the reference case α = 2 Δ_{xy}. Using the convergence curves of figure **??**, we expect the result obtained for α = 1.1 Δ_{xy} to belong to the hazardous region where the error level starts to increase and this solution while not completely erroneous is becoming untrustworthy. However for the solution without filter strange small structures appear and the overall topography, despite being the more complex of all, does not have any physical origin.

We now switch to a second synthetic case study. The numerical domain corresponds again to a rectangular grid ~~with the~~ but this time with dimensions $Lx = 600$ km in the x axis and $Ly = 80$ km is the y axis containing a mesh of resolution $\Delta_{xy} = 0.25$ km. The basement is b is constant equal to 0 m, while the sediment thickness h_s is initially given by a uniform in x smooth bump:

$$g(x,y) = \begin{cases} H \exp\left(\dfrac{-1}{1-r_y^2}\right) & \text{for } r_y = \frac{(y-y_c)}{\delta_y} \leq 1, \\ 0 & \text{otherwise}, \end{cases}$$

with $H = 20$m , $y_c = 40$ km and $\delta_y = 20$ km. This symmetry in the x direction of the initial topography is then perturbed by ~~a~~ N_b=30 small smooth bumps randomly positioned at points (x_p, y_p):

$$g_{pert}(x,y) = \begin{cases} H_{pert} \exp\left(\dfrac{-1}{1-r^2}\right) & \text{for } r^2 = \frac{(x-x_p)^2}{\delta^2} + \frac{(y-y_p)^2}{\delta^2} \leq 1, \\ 0 & \text{otherwise}, \end{cases}$$

with $H_{pert} = 1$ m and $\delta = 2$ km. Rain-fall is constant in time and space (3000 mm/y) and is the unique water supply for this case. The sediment source (here we simulate a sediment production) goes from $S_s = 0$ m.My^{-1} at $y = 0$ and $y = Ly$ sides to $S_s = 100$ m.My^{-1} at $y = Ly/2 = y_c$. The variation is continue over the whole domain following :

$$S_s(x,y) = \begin{cases} S_{max} \exp\left(\dfrac{-1}{1-r_y^2}\right) & \text{for } r_y = \frac{(y-y_c)}{\delta_y} \leq 1 \\ 0 & \text{otherwise} \end{cases}$$

with $\delta_y = 40$ km. Model boundary conditions are fixed elevation on the sides normal to the x axis and zero gradient on the sides normal to the y axis. Models parameters controlling the non-linearity in the water-sediment coupling are set as $r_s = 2$, $p_s = 0$~~, $p_w = 0$ and $k_m = 1$ m. s^{-1}~~. Simulation takes place over the time period $T = 6$ My~~, using the numerical schemes detailed in section **??**. The first simulation use constant diffusive coefficients k_g~~c: solution with filter for (k_g, k_w)=(50,5) km^2.~~My~~.My^{-1} ~~and k_w~~, d: solution without filter for (k_g, k_w)=(5,5) km^2.~~My~~.My^{-1}~~, and the initial topography is built with $N_b = 30$. In order to analyze the results of this simulation and the following ones, it is also important to discuss the implications of the values of the~~

diffusion coefficients. At this point, we want to stress the fact that those specific values k_g, e: solution with filter for (k_g, k_w)=50 km ^{2}.My^{-1} and k_w= (5,5) km^2.My^{-1} have been chosen on purpose, such that our non-linear diffusive model should be able to diffuse quickly small initial perturbations such as the ones we introduce and thus loose memory of its initial state as would a classical linear diffusive model. Of course the key parameter is the dimensionless ratio $\tau = (k_w q_w^{r_s})/(k_g q_{ref}^{r_s})$ which plays an essential role here, small valuesimplying a gravity dominated case while larger values correspond to a water dominated case. The ratio τ is clearly reminiscent of the Reynolds number for turbulent flows, with true turbulence appearing with large Reynolds numbers.It is our belief, although we do not have any formal proof at this stage, that one can anticipate the "chaotic" or "non chaotic" behavior of the solution by considering the values of τ. For this test case, in the part of the domain where the slope is significant, the ratio τ is below 10. We expect this case to be close to a quite gravity dominated one, but not too much such that the potential problems linked to numerical errors are not completely dissipated by the gravity diffusion. With that in mind, we could expect no specific amplification of the initial bumps in the topography. In order to emphasize the impact of the consistency and the effect of filtering on the emergence of complex geomorphic features, we have first performed a simulation mimicking those of the literature using the non-consistent version of the water flux without filtering, i. e. we momentarily chose for $\mathcal{Q}_w$ to use the non consistent $\widetilde{q}_K$ of the MFD literature chosen from Freeman **?** and updated by **?**). However, final elevation is clearly not homogeneous in the x direction, suggesting a dominant effect of the bumps on the results. Figure **??** shows that in this non consistent, unfiltered setting the obtained elevation is quite complex and the final heterogeneity do not seem necessary located at the same x_p positions. In fact, all the domain seems to have been impacted by the small perturbations in the initial topography. Water flow distribution (represented by the dark blue color in figure **??**) is organized, suggesting the emergence of characteristic length-scale that controls the valley spacing. The illustrates the issue describe din the introduction: without any reference it is very hard to decide wether this result is the correct physcial one or not. a: initial unperturbed topography, b: final state for consistent MFD and Δ_{xy} = 1 km, c: final state for non consistent MFD and Δ_{xy} = 1 km, d: final state for consistent MFD and Δ_{xy} = 0.25 km, e: final state for non consistent MFD and Δ_{xy} = 0.25 km a: initial topography with a single perturbation, b: final state for consistent MFD and Δ_{xy} = 1 km, c: final state for non consistent MFD and Δ_{xy} = 1 km, d: final state for consistent MFD and Δ_{xy} = 0.25 km, e: final state for non consistent MFD and Δ_{xy} = 0.25 km a: initial perturbed topography, b: final state for consistent MFD and Δ_{xy} = 1 km, c: final state for non consistent MFD and Δ_{xy} = 1 km, d: final state for consistent MFD and Δ_{xy} = 0.25 km, e: final state for non consistent MFD and Δ_{xy} = 0.25 km a: initial topography with a single perturbation, b: final state for with consistent MFD with filter, α= 1200 m and Δ_{xy} = 1 km, c: final state with consistent MFD with filter, α= 0.3 km and Δ_{xy} = 0.25 km a: initial perturbed topography, b: final state with consistent MFD with filter, α= 1200 m and Δ_{xy} = 1 km, f: final state with consistent MFD with filter, α= 0.3 km and Δ_{xy} = 0.25 km

As a first step towards a clear answer to this, we perform a set of four simulations using an initial homogeneous in the x-direction topography ($N_b = 0$), still with the same diffusive coefficients. We respectively display in Fig. **??** the initial topography without any perturbation and the final result obtain without any filter, , f: solution without filter for $\Delta_{xy}(k_g, k_w)$=1 kmand Δ_{xy}=0.25 km, for the consistent and non consistent MFD. In all cases, the final topography remains uniform in the large direction as expected, and the result is clean of any perturbations for both mesh sizes, for both choices of water flux. This series of run indicate here that under the right circumstances (probably linked to τ) the corrections such as the one of **?** can

lead to the false impression that they do correct $\widetilde{q}_K$ in the right way.Simulations shown Fig. **??** are similar to those in Fig. **??** but the initial topography contains a single perturbation ($N_b = 1$) . We display the initial topography with a single perturbation (one bump), as well as the final topography obtained using again the consistent and non-consistent MFD, both without filter and again for Δ_{xy}=1 km and Δ_{xy} =0.25 km. Looking at the results for Δ_{xy} = 1 km, we see that the consistent version leads to the same uniform final topography than in the unperturbed situation. On the contrary, the non-consistent MFD introduces a non negligible error in the final result: we see here how the non-consistent MFD of the literature can clearly introduce numerical artifacts. However when we look at the results for Δ_{xy}= 0.25 km, both schemes produce finals topographies with large perturbations induced by the initial bump, but with much wider ones for the non-consistent case as should be expected. At this point it is hard to decide if the solution **??**-D of the consistent MFD with Δ_{xy} =0.25 km is the correct approximation of the solutionof --, implying in this case that the previous mesh size Δ_{xy}= 1 km was too coarse, or if what we see are again numerical artifacts. Comparing with the results obtained combining the consistent MFD with filters, which are presented for the case with a single perturbation in Fig. **??**-b for (α, Δ_{xy})= (1.2 km, 1km) and **??**-c ,5) km^2.My^{-1}, g: solution with filter for $(\alpha, \Delta_{xy})(k_g, k_w)$=(0.3 km, 0.25 km), we see that the consistent plus filter version always leads to the uniform final topography for both mesh sizes. Of course, only one of the two consistent results (with or without filters) can be the correct one. At the very least this first comparison emphasizes why the non-consistent MFD should no longer be used: indeed, it should now be obvious that the complexity observed in Fig. **??** was undoubtedly the mainly the product of amplified numerical errors. However as the values Δ_{xy}=0.25 km and α=0.3 km have been chosen small enough to resolve the small initial bumps or the "width" of the water flow appearing around the bumps, we are confident that the consistent plus filter uniform solution (Fig **??**-c) that used those parameters is the correct approximation of the solution of --, implying that the consistent without filter solution (Fig. **??**-d) was erroneous. Another strong argument in this sense is that noise appears in the unfiltered consistent case when refining the mesh, with even more noise for more refined meshes: our interpretation is that numerical diffusion, which is much smaller that the true physical diffusion in view of the values of k_g adds nevertheless enough additional smoothing for Δ_{xy} = 1km to dissipate large parts of the numerical errors while this is no longer the case for the finer mesh Δ_{xy} = 0.3 km. We finally perform the very same experiments with the fully perturbed initial topography (30 bumps). The results for the unfiltered non consistent and consistent MFD are presented in Fig. **??**, while the consistent plus filter results are displayed in Fig. **??**. It is obvious that the same conclusions apply to this more complex case: considering the results for Δ_{xy} = 1 km, we recover the fact that using a consistent scheme improves the results, but this time not even enough to keep numerical errors under control. However we see that in the consistent case, not all bumps correspond to a final deformation. This is another clear sign that something is wrong with this solution, even if the errors remain relatively small. For Δ_{xy} = 0.25 km we obtain very complex topographies which may appear as realistic but are in fact clearly solutions blurred by numerical noise. This affirmation is enhanced when look at the clean uniform final state obtain with filters which is again the correct approximation of the solution of --,5) km^2.

As we have already explained, the values of k_g and k_w were purposely chosen in the above experiments to lead to this treacherous situation where the correct solutions are clean and uniform despite of

The second synthetic case study has similarities with the initial perturbations. However, this does not mean that solutions obtained using filters will never develop complex topographies, but that they can only contain heterogeneity that is not the

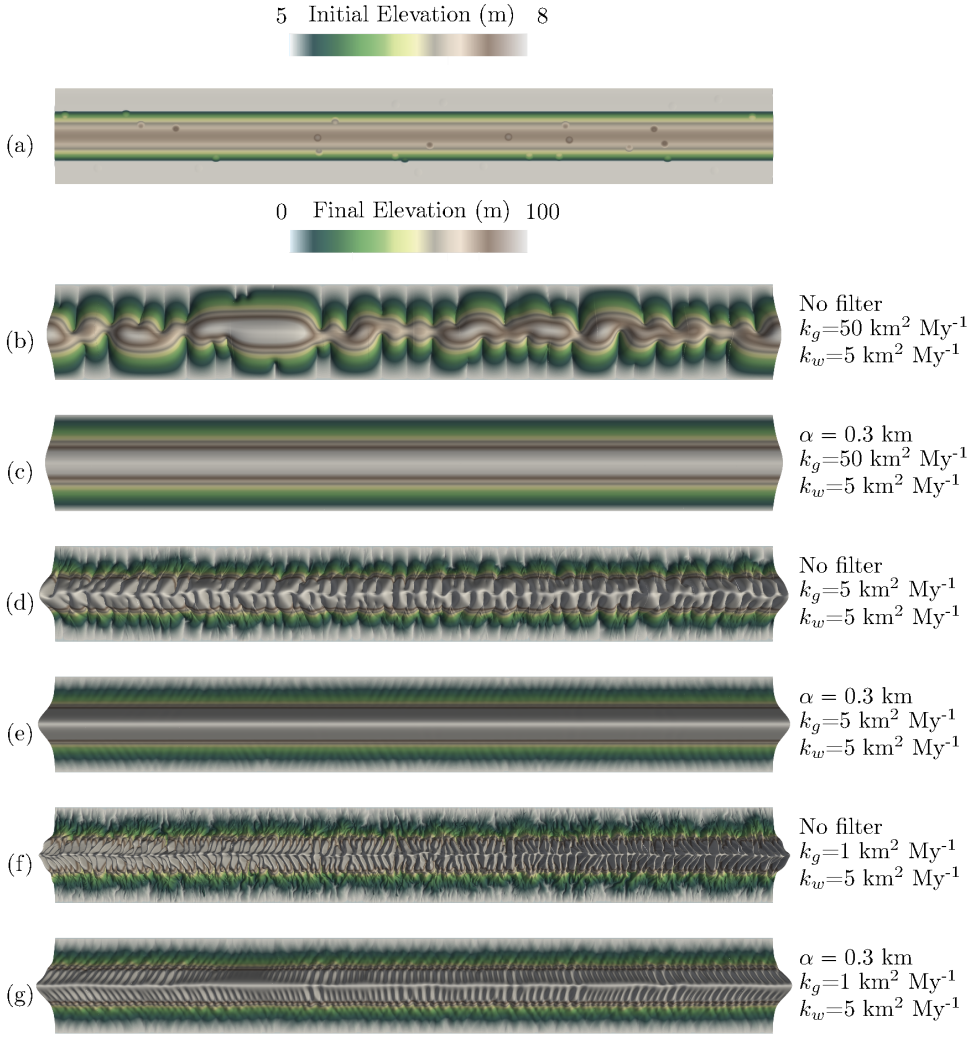

Figure 19. Final topographies obtained for three different set of diffusive coefficients, systematically tested without filter and with a filter using $\alpha = 0.3$ km. a: initial perturbed topography. b: solution without filter for (k_g, k_w)=(50,5) km^2.My^{-1}, c: solution with filter for (k_g, k_w)=(50,5) km^2.My^{-1}, d: solution without filter for (k_g, k_w)=(5,5) km^2.My^{-1}, e: solution with filter for (k_g, k_w)=(5,5) km^2.My^{-1}, f: solution without filter for (k_g, k_w)=(1,5) km^2.My^{-1}, g: solution with filter for (k_g, k_w)=(1,5) km^2.My^{-1}

product of amplified numerical errors. To illustrate this, we consider again the perturbed test case but this time using $k_g$previous one in terms of boundary conditions, but its larger spatial-scale makes it relatively close to the case studies published in **??** . We display the initial topography (Fig **??**-a) as well as the final topography obtained with and without filter for k_w= 5 km^2.My^{-1} , then and for three different k_g values. The first case considers k_g= 1 50 km^2.My^{-1} ^{2}.My^{-1}. The relative high k_g value compared to k_w should not favor the emergence of geomorphic structures. This is however not what we observe in

the simulation performed without filter (Fig **??**-b). The filter, defined by $\alpha = 0.3$ km, has a huge impact and no geomorphic structure is produced (Fig. **??**-c) which is undoubtedly the correct solution. An order of magnitude smaller k_g coefficient is used for the second simulation. By decreasing k_g, the emergence of structure may be considered as a realistic result. In this case, complex structures controlled by at least one wavelength appear in the simulation performed without filter (Fig. **??**), for which we easily get $\tau >> 10$ in the key parts of the domain and we expect the system to start producing more complex topographies. We only consider the situations with α =0.3 km and Δ_{xy}=0.25 km, again to ensure that at least some of the small scales of the model are correctly resolved by both the filter **??**-d). The effect of filter however indicates the very likely artificial origin of these structures. A residual perturbation can still be observed in the final topography (Fig. **??**-e), indicating that this k_g and the mesh. Of course, for such large values of τ what we obtain is potentially an averaged version at the filter scale of k_w configuration is at the transition between two regimes, the correct continuous solution of --. We present in Fig. **??** results with and without filters for the consistent scheme, recovering the fact that the numerical solution without filters is blurred by noise. In the intermediate case gravity-driven and the water-driven erosion regimes. In our last simulation, we have decreased k_g = 5 km^2.My^{-1}, we start to see some small topographic perturbations, while we also see that for the case with k_g= 1 km^2. My^{-1} and thus the largest value for τ, complex structures finally develop, assessing the fact that the model with by a factor 5 and we indeed observe the emergence of structures even when the filter is perfectly capable of producing complex topographies when this corresponds to the correct averaged solution. Yet we insist on the fact that recovering all the details of the correct continuous solution of --requires α to correctly resolve all the scales of the model, otherwise what we obtain is a numerical approximation of the averaged solution at the filter scale. For instance if we use a filter with parameter α=1.2 km as previously done the final topographies for active (Fig. **??**-g). Here again the impact of the filter is important and allows to keep only what we believe to be the correct structures.

This last set of simulation shows the major impact of k_g in the wavelength of the structures that can emerge from our simulation. We have also performed additional simulations using various k_w values for a given k_g= 5 km^2.My^{-1} and . The results have shown that k_w must be high enough to make the structures appear, but they also show that k_g = 1 km^2.My^{-1} are indeed much more smooth that those presented in Fig. **??**.

was most important than k_w in the wavelength control. We consider a dedicated study should be conducted with our model to quantify these effects but it is beyond the scope of this article. A complete study can be found in **?**. Even if it was performed using an other LEM model, similar conclusions with those drawn from his study are also expected in our case.

5 Discussion

This work belongs We consider this work as belonging to the common effort of the scientific community to harmonize landscape evolution models. The implementations of the consistent water flux and the It is our belief that the most of our observations and practical recommendations can also be applied to a wider range of sediment evolution models that the one we use in this study. The implementation of the large structure simulation strategy should be accessible to every LEMs , and in particularsatisfying (H1), (H2) and (H3). In particular, we believe that filtering would be also very useful for the models of

??? that takes the general form:

$$\left|\begin{array}{ll} \dfrac{\partial h_s}{\partial t} + div\,(\boldsymbol{J}_s) = S_s & \text{in } \Omega\times]t_0,T[, \\ -\boldsymbol{J}_s\cdot\boldsymbol{n} = B_s & \text{on } \partial\Omega_{\mathcal{N}}\times]t_0,T[, \\ h_s = 0 & \text{on } \partial\Omega_{\mathcal{D}}\times]t_0,T[, \\ h_s(t=t_0) = h_{s,0} & \text{in } \Omega, \end{array}\right. \tag{22}$$

with a source given by

$$S_s = U - \kappa_w s_{ref}^{-p_{s,2}} \left(\frac{q_w}{q_{ref}}\right)^{r_s} ||\nabla(h_s+b)||^{p_{s,2}},$$

with U a sediment source term (or an uplift depending on the interpretation of b) and a sediment flux given by:

$$\boldsymbol{J}_s = -s_{ref}^{-p_s} k_g ||\nabla(h_s+b)||^{p_s}\nabla(h_s+b) \quad \text{in } \Omega\times]t_0,T[.$$

~~Those~~ The behavior of those models are relatively close to model (**??**)-(**??**) that we have studied in detail here, with the main difference that the non-linear term $q_w^{r_s}||\nabla(h_s+b)|^{p_s}$ appears as a reaction term rather than in a diffusive term. ~~An~~ In particular, for $p_w = -1$ the observations on linear stability for model (**??**) match the conclusion of the linear stability analysis of **??**. We can thus expect that model (**??**) will potentially suffer from similar numerical stability issues that the ones we analyzed in detail for model (**??**)-(**??**), although this certainly requires a dedicated study before drawing conclusions. In particular, several elements can help keeping the numerical errors under control: high order space and time schemes, explicit time schemes, specific solvers for the water flow model avoiding inverting a linear system, etc. Nevertheless, an immediate application of the LSS in this context consists of course in replacing q_w by its filtered version $\mathcal{F}^{\mathcal{N}}(q_w)$ in the second member of (**??**) and can only improve the numerical stability. We also believe that the ξ-q model of **?** could benefit from a similar filtering strategy. ~~Notice nevertheless that the last test cases displayed in Fig. ?? emphasize the fact that correctly~~

Correctly using filters requires some understanding of the scales involved in the model. Although this is not ~~a such~~ such an easy task in general, ~~we believe that it is very likely that to get an idea of those scales one can use τ in the same way than the viscosity and more generally Reynolds number can be used to anticipate the flow scales. Nevertheless, we can give some generic guidelines that should apply in any situation: first, at the very least the constraint ont the mesh size $\varepsilon < \alpha$ must be fulfilled to allow the filter to correctly clean the sub-cell scale phenomenons. Next,~~ as generic guidelines concerning the relation between the filter size α and the precision of the results it is clear that the chosen filtering parameter α should resolve the main sediment structures that one wants to correctly represent in the flow, ideally fulfilling an equivalent of Nyquist's rule. For instance if an essential valley is 1 km large, then α should be several times smaller (and ideally smaller than 100 m). A good practical test consists in comparing the filtered topography $\mathcal{F}(h_s+b)$ and the unfiltered one h_s+b. The structures of h_s+b that one wants to simulate ~~accurately~~ accurately should be preserved in $\mathcal{F}(h_s+b)$, of course in a smoother way. For instance, for a given value of α if a small topographic depression in which water could in principle flow is observed on h_s+b

but is absent in $\mathcal{F}(h_s + b)$, then if one really wants to capture water flow inside this "channel" the value of α must be reduced and the mesh refined accordingly if needed. The filter should in any case be able to clean numerical approximation and solver errors, implying that we should at the very least have $\gamma = \alpha/\Delta_{xy} > 1$ to correctly resolve the targeted α spatial scale. To allow the filter to correctly clean errors that could otherwise have a destabilizing effect on the final configuration, higher values of α should probably be used for increasing values of τ.

Notice that in the present paper, we have for simplicity always used uniform meshes with a constant Δ_{xy}, hence obtaining a constant ratio $\gamma = \alpha/\Delta_{xy}$. As an immediate extension, one could resort to adaptive mesh refinement to refine the mesh in areas where τ becomes large and thus where numerical errors are more likely to be large, mitigating the increase of the system's size and thus the increase of the computational cost. In practice for constant coefficients k_g and k_w this would be equivalent to refining the mesh where water flow occurs. In addition, one could replace the constant parameter α by a space/time variable coefficient $\alpha(x, y, t)$ in an adaptive filtering strategy, where the filter size could be chosen in coherence with the local size of the structures one wants the model to be able to reproduce.

5.1 Recovering realistic landscapes

~~Both the consistent MFD and the~~ In principle, the use of filters ~~are introduced~~ allows to get rid of ~~any mesh dependency and~~ the influence of numerical noise in the solution. An apparent drawback is that for unperturbed data, complex topographies ~~are less likely to~~ will no longer appear by themselves through the perturbations induced by either the numerical approximation or the numerical solvers. Moreover, natural landscapes ~~do have~~ exhibit some heterogeneity even ~~for situations where~~ under low τ ~~is not that high and that we thus suspect to not being "chaotic". Consequently it would be highly interesting to have a simple tool that allows to recover~~ regime. This suggests an ingredient is missing, and this ingredient is well-known by geologists: the heterogeneity. Indeed heterogeneity is everywhere in nature, and could be injected in such a model to make realistic looking topographies ~~. Fortunately, thanks to our interpretation of MFD as a discretization of , we see that the coefficient~~ emerge. This idea is of course not new but we propose to invesigate the effect of heterogeneity in the context of the hydro-sedimentary model we use for this paper.

The first heterogeneity we consider here is injected into the k_m ~~can play this role as it will naturally induce heterogeneity in the flow. To illustrate this~~coefficient, reflecting variable soil rugosity. Since acquiring a roughness map adapted to the spatial scales relevant to our approach is difficult and probably not relevant for a synthetic case study, we resort to an artificial yet efficient trick, namely the Perlin noise **?** that is often used in animated movies or video games to produce realistic looking mountains or river networks. This type of noise can easily be used to build isotropic heterogeneity maps with controlled spatial scales. We thus consider our "three rivers" test case using variable coefficients k_m in space and time (Fig. **??**). Figure **??**~~b~~ -b illustrates a typical distribution in space of the k_m coefficients when using a Perlin noise. The range of values for the k coefficient (from $k_m = 0.01$ m.s^{-1} to $k_m = 10$ m.s^{-1}) is arbitrarily fixed while respecting realistic value ranges. Impacted by the heterogeneity in k_m, the water flow is still distributed between neighboring cells according to the gradient of the slope, but it ~~will~~ also preferentially choose to enter the cell ~~at~~ with the highest k_m, especially when the slopes become gentle and relatively

close between neighbors. ~~Consequently, heterogeneous k_m coefficients help in keeping the water flow focused even on gentle slopes. Having a realistic range of k_m values may seem uncertain. Indeed, range of k_m values can be compared with the range of typical Gauckler-Manning-Strickler roughness coefficients measured in nature for different vegetation and lithology (e.g. ?) but only if the mobility function is considered to be the hydraulic radius with a unit value of one meter. However, as this assumption is not relevant for the spatial-scales currently considered for in LEMs, there is no direct link between k_m and currently available roughness values. We thus simply fixed for this simulation minimum coefficients values at $k_m = 0.01$ m.s^{-1} and maximum coefficients values at $k_m = 10$ m.s^{-1} to get realistic ranges of the flow velocity in rivers and k_m variation.~~

The flow then acquires a high degree of complexity despite a filter which set at $\alpha = 1.1\Delta_{xy}$ makes it possible to eliminate numerical errors.

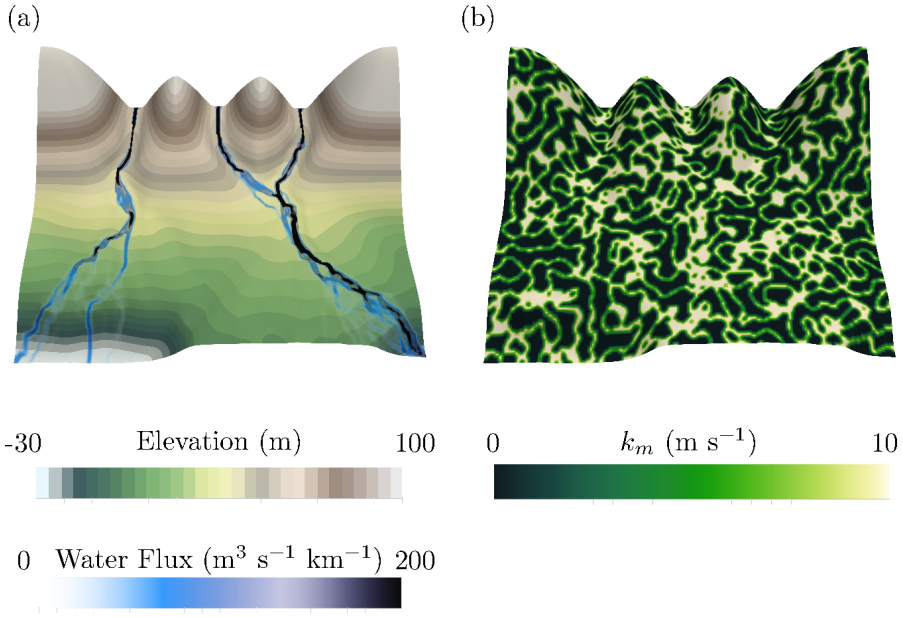

Figure 20. The "three rivers" test case with Perlin noise based coefficient k_m. a: Final (at T=6My) elevation and associated water flow with variable in space and time k_m coefficients. b: k_m coefficients at T=6My

The same approach can be applied ~~in~~ to the other synthetic test case used in section ~~??. The set of simulations shown in Fig. ?? are~~ **??**, using $\alpha = 2\ \Delta_{xy}$: the simulations are now performed with spatially and temporally varying k_m coefficients (the same range of k_m values is ~~also usedhere). The first observation is that more complex topographic structures are simulated (to be compared with Fig. ??). The two first simulations (Fig.~~ used). Figure **??**-a-b ~~) have the same~~ shows the initial and the final state of the simulation with a special focus on the geomorphic structures produced, which are clearly more complex when comparing to the result shown in figure **??**-d.

In a second time, we introduce a similar heterogeneity in the rain maps. When we use solely a rain heterogeneity incorporating

the same spatial scales than in the k_m ~~coefficients distribution. We set (α, Δ_{xy})= (1.2 km, 1 km) for the first simulation (Fig. ??-a) while (α, Δ_{xy})= (1.2 km, 0.25 km) is used in the second simulation (Fig. ??-b). The final elevation between those two simulations are very close, which is what is expected. Differences are still observable, but mainly at small spatial scales, where the effect of the grid refinement allows to capture more details. We then set (α, Δ_{xy})= (0.3 km, 0.25 km) for the third simulation (Fig. ??~~maps, the geomorphic structures produced are very similar to those obtained using only the heterogeneous k_m coefficients . The most visual satisfying result is obtained for a simulation using both variable k_m and rain maps (Fig. **??**-c~~).~~ ~~It shows that using a a filter size close but slighty above to Δ_{xy} is also important to capture the whole small-scale features that can be simulated on this discretized domain. Finally, the last simulation (Fig. ??-d) has exactly the same parameters that the third one, but another heterogeneity is added on rain-fall, using here again a Perlin noise. Of course the more complex topography is produced when the more heterogeneity in data is injected. Figure ?? shows a frontal representation of the same simulation with the associated water flow. Comparing with Fig. ??, we have jumped from a non-consistent, non-reproducible and numerical errors dominated model to consistent and reproducible model able to produce complex geomorphic features.~~). ~~This result encourages us to say that our model has the ability to reproduce complex and realistic structures. However, further investigations will have to be performed to confirm. In particular, an detailled analysis of the valleys geometry and spacing will have to be undertaken to understand more precisely the dependency on $\tau = (k_w q_w^{r_s})/(k_g q_{ref}^{r_s})$.~~

5.2 Overcoming the accumulation and flat areas limitations~~of MFD approaches~~

In the general setting, there is no reason why the sediments should evolve in such a way that ~~the "drainage" or "curvature" assumption~~ one of the sufficient conditions (**??**) is always fulfilled, which can lead to some non physical behavior of the GMS model (**??**) and thus also the pure MFD algorithms. ~~Indeed, for cells such that $s_K = 0$, the MFD algorithms stop water in cell K and no flow can go to the neighbours of cell K.~~ This can occur in two obvious situations: ~~when K belongs to~~ in an accumulation area (a topographic depression) or a flat area~~(all neighbours either higher or at the same level than K)~~. In principle, water arriving into an accumulation area should create a "lake" whose bathymetry will be determined by a water balance between incoming flow, infiltration and evaporation. If the surface reaches the threshold of the lake, then some water leaves the lake and the water flow restarts from the lake threshold. In flat areas, water will spread diminishing its height until the full area is covered. To reproduce those effects that are not originally taken into account, implementations the MFD algorithms ~~and more generally the flow routing algorithms of the literature~~ all incorporate practical workarounds~~that can take different forms: a uniform distribution of flow over neighbours for flat areas, a water balance under the hypothesis of a flat water surface for accumulation areas, etc~~. Thanks to our interpretation as the discretization of a continuous model, ~~first we can observe that those limitations should be expected., as is well-posed from the mathematical point of view if $-\Delta(h_s + b) > 0$ which corresponds to a no water accumulation areas or flat areas assumption. The second observation is that we can~~ we can easily propose a generalization of (**??**) that overcomes those limitations, by noticing that model (**??**) is in fact a simplification of the shallow water equations with friction. Indeed, appropriately choosing the friction model and assuming that the mass conservation of water is at steady state a quite general model arising from applying the hydrostatic approximation to the

shallow water equations would be to consider (see appendix **??**):

$$\left|\begin{array}{ll} -div\left(k_m h_w \eta_w\left(h_w\right) s_{ref}^{-p_w}||\nabla(h_w+h_s+b)||^{p_w}\nabla(h_w+h_s+b)\right)=S_w & \text{in } \Omega, \\ -k_m h_w \eta_w\left(h_w\right) s_{ref}^{-p_w}||\nabla(h_w+h_s+b)||^{p_w}\nabla(h_w+h_s+b)\cdot n=B_w & \text{on } \partial\Omega_{\mathcal{N}}, \\ h_w=0 & \text{on } \partial\Omega_{\mathcal{D}}, \end{array}\right. \tag{23}$$

with the associated water flux strength:

$$q_w=\left|k_m h_w \eta_w\left(h_w\right)\right| s_{ref}^{-p_w}||\nabla(h_w+h_s+b)||^{p_w+1}. \tag{24}$$

This is almost (**??**) except that it uses the hydraulic gradient instead of the topographic one.The assumption $\nabla(h_s+b)\approx\nabla(h_w+h_s+b)$ while valid on pronounced slopes is obviously not valid anymore in accumulation areas (at equilibrium, the hydraulic gradient is almost zero while the topographic gradient is large) and flat areas (where the topographic gradient is zero and the hydraulic one is not)~~, which is coherent with the restriction to areas such that $-\Delta\left(h_s+b\right)>0$~~. The non-linear model (**??**) is thus a natural generalization of the GMS model (**??**) with a built-in handling of accumulation and flat areas which no longer requires practical workarounds. However, model (**??**) does not come without any drawbacks. The first one is that we now have to choose the water mobility function η_w, as we are solving for the water height unknown. This will both influence the repartition of water and the strength of the water flow~~, while it was completely transparent for the MFD approach with model~~ . In the same way, the absolute value of the coefficient k_m will now impact the strength of the water flux through h_w, while only its contrasts were relevant for the GMS model (**??**). Thus, some fine tuning is required for (**??**) to produce meaningful results. The last and probably more important drawback is that (**??**) being non-linear in its unknown h_w, its discretization will be more involved and computationally expensive than for (**??**). ~~We perform it using again finite volumes which will in practice require solving non-linear equations instead of solving the well-behaved MFD linear system . This is the reason why the MFD remains an attractive alternative when no flat areas appear in the topography, the water balance and flat water surface assumption giving in general good results for accumulation areas. Indeed, let~~ Llet us compare the results obtained with the original ~~Gauckler-Manning-Strickler~~ GMS model (**??**) and with the more involved hydrologic model (**??**) on the "three rivers" test case, using filters in both cases. The water mobility function η_w for (**??**) is simply chosen as equal to one if h_w is positive and 0 otherwise.

As we can observe in Fig. **??**, if the two models of course do not produce exactly the same results the general behavior is very similar. Even more close results could certainly be obtained by finely tuning the mobility function. We do not want to explore this any further in the present paper and simply want to illustrate that while suffering from some limitations, the ~~consistent MFD (~~GMS model (**??**) ~~) is~~ and thus MFD algorithms remain a very strong and attractive approximation on ~~draining topographies. In particular, the MFD computations can easily be an order of magnitude faster that the full hydrologic computations which fully justifies using MFD for draining topographies provided the consistency correction depicted in the first part of the paper is used.~~ suitable topographies.

6 Conclusions

After ~~recalling the interpretation of ? of MFD algorithms as discretization of Gauckler-Manning-Strickler and the associated consistency correction, we have explained how to extend it to the most classical MFD algorithms of the literature in order to get rid of their well documented mesh dependency. This is a necessary yet not sufficient step to obtain reproducible landscape evolution simulations. Next~~illustrating the numerical instabilities arising from the self-amplification phenomenons at the core of coupling overland flow and sediment evolution models, we have proposed to mimic the LES strategy for CFD computation in the context of landscape evolution models, relying on the well known Leray-α differential filter. Numerical experiments assess that ~~the combination of consistent MFD and~~ filtering produces results robust to numerical perturbations. It is our belief that this "large structures simulation" (LSS) approach goes far beyond the specific model considered here and that any LEMs could benefit from it~~, especially as the cost of implementing and using filtering is not high~~. Indeed, experiments performed without any filtering strategy have shown that it ~~is~~ can become extremely difficult to distinguish between the imprint of numerical errors and physical processes. Provided fine enough filter parameter and mesh size are used, only the non physical heterogeneity will disappear. The apparently missing visual complexity that previously arose from numerical noise can be physcally re-introduced when heterogeneous data are considered. Similarly to LES models, we believe that a mathematical analysis and numerical analysis of the filtered model should be achievable. ~~Both are the subject of active research and we~~ We hope to be able to publish such analysis in a future paper. ~~In particular we anticipate that this may bring a more straightforward link between the value of the ratio τ and the transition from non chaotic to chaotic behaviors. Let us also mention that although we have only presented here a mono-lithologic version of our model, our implementation considers the mutli-lithologic case which opens perspectives for realistic case studies~~To complete this work, we also plan to use in our next study the full model capacity in building a mutli-lithology realistic test case. Finally, pursuing the analogy with LES, an interesting perspective would be to analyze whether it is feasible to develop sub-filter models to increase the filtered model accuracy when α is quite large, in order to reduce the need for fine α and thus fine meshes and consequently the overall cost of the approach.

Code availability. All the numerical schemes used in this paper are fully described in the appendix **??**. Implementation was performed in code ArcaDES, which is available through the commercial simulator DionisosFlow™.

Appendix A: ~~Finite volume discretization~~Derivation of analytic solutions

~~In this section we describe the full finite volume discretization of system ---. We assume that the mesh is compatible with the boundary decomposition, i. e. there exists subsets $\mathcal{F}_{ext}^{\mathcal{N}}$~~ For simplicity, we consider in this section the special case where $b = 0$, k_w and ~~$\mathcal{F}_{ext}^{\mathcal{D}}$ such that~~k_g are constants, the water mobility function and coefficient k_m are both equal to one $\eta_w(h_w) = 1$ and $k_m = 1$. To ease the reading, we will not write the dimension constants s_{ref} and q_{ref}, as they are both equal to one in the

chosen unit system. The sediment flux simplifies into:

$$\boldsymbol{J}_s = \bigcup_{\sigma\in\mathcal{F}_{ext}^{\mathcal{N}}} -\eta_s(h_s)||\nabla(h_s+b)||^{p_s}\left(q_w^{r_s}k_w\nabla(h_s+b)+k_g\nabla(h_s+b)\right) \quad \text{and} = \bigcup_{\sigma\in\mathcal{F}_{ext}^{\mathcal{D}}} . \text{ in } \Omega\times]t_0,T[,$$

~~Notice that all our simulations without filters employs the same numerical schemes but of course replacing the filtered values by the original ones. ***Leray-α filtering equation:*** Using the TPFA the approximate filter $\mathcal{F}_{\alpha,h}$ is defined for $u_\mathcal{T} = ((u_K)_{K\in\mathcal{T}},(u_\sigma)_{\sigma\in\mathcal{F}_{ext}})$ by~~ We consider the simplified setting where $\eta_s(h_s)=1$, which is only an approximation of the function η_s we have used everywhere else in the paper. This setting corresponds to the analytic steady state solutions studied in **?**. Since $\eta_s(h_s)\approx 1$ as soon as h_s is large enough, we label those solutions as "quasi steady state". We seek quasi steady state solutions that are morevoer uniform in the y variable $h_s(x,y,t)=h_{s,x}(x)$, and symmetric with respect to the axis $x=0$, and we consider only the interval $]0,Lx/2[$. We finally assume that S_s and S_w are equal to two constants $S_{s,x}$ and $S_{w,x}$. We have consequently $\nabla(h_s+b)=\partial_x h_{s,x}\boldsymbol{e}_x$ and the water equation reduces to:

$$\mathcal{F}_{\alpha,h}(u_\mathcal{T}) = ((\mathcal{F}_{\alpha,K}(u_\mathcal{T}))_{K\in\mathcal{T}},(\mathcal{F}_{\alpha,\sigma}(u_\mathcal{T}))_{\sigma\in\mathcal{F}_{ext}}),$$

$$-\partial_x\left(h_{w,x}|\partial_x h_{s,x}|^{p_w}\partial_x h_{s,x}\right) = S_{w,x}.$$

~~where:~~

$$\alpha^2\sum_{\sigma\in\mathcal{F}_K\cap\mathcal{F}_{int}}\frac{|\sigma|}{\overline{d}_{KL}}(\mathcal{F}_{\alpha,K}(u_\mathcal{T})-\mathcal{F}_{\alpha,L}(u_\mathcal{T}))+|K|\mathcal{F}_{\alpha,K}(u_\mathcal{T}) = |K|u_K \quad \text{for all } K\in\mathcal{T},$$

$$\mathcal{F}_{\alpha,\sigma}(u_\mathcal{T}) = \mathcal{F}_{\alpha,K}(u_\mathcal{T}) \quad \text{for all } K\in\mathcal{T} \text{ and all } \sigma\in\mathcal{F}_K\cap\mathcal{F}_{ext}^{\mathcal{N}},$$

$$\mathcal{F}_{\alpha,\sigma}(u_\mathcal{T}) = 0 \quad \text{for all } K\in\mathcal{T} \text{ and all } \sigma\in\mathcal{F}_K\cap\mathcal{F}_{ext}^{\mathcal{D}}.$$

~~The discrete Neumann filter $\mathcal{F}_{\alpha,h}^{\mathcal{N}}$ of course satisfies but with Neumann boundary conditions on every $\sigma\in\mathcal{F}_{ext}$. ***Sediment mass conservation equations:*** We now assume that the time interval $]0,T[$ is subdivided into N_T subintervals $]t_n,t_{n+1}[$, where $t_0=0$ and $t_{N_T+1}=T$. We denote $\Delta t^n = t_{n+1}-t_n$. The discrete quantities associated with time t_n will be denoted as usual with a superscript n. The TPFA finite volume scheme for the mass~~ Assuming $-\partial_x h_{s,w}>0$ (the solution is decreasing fom the center of the domain to its boundary) this leads to $\partial_x q_{w,x}=S_{w,x}$, $q_{w,x}=-h_{w,x}|\partial_x h_{s,x}|^{p_w}\partial_x h_{s,x}$, and finally $q_{w,x}=q_w(0)+S_{w,x}x$.

In the same way, the conservation of sediments ~~for the flux is given by~~reduces to:

$$\left|\begin{array}{l} \dfrac{|K|}{\Delta t^n}(h_{s,K}^{n+1}-h_{s,K}^n)+\displaystyle\sum_{\sigma\in\mathcal{F}_K\cap\mathcal{F}_{int}}\frac{|\sigma|}{\overline{d}_{KL}s_{ref}^{p_w}}\eta_{s,\sigma}^{n+1}\Delta\Psi_{KL}^{n,n+1}+\sum_{\sigma\in\mathcal{F}_K\cap\mathcal{F}_{ext}^{\mathcal{D}}}\frac{|\sigma|}{\overline{d}_{K\sigma}s_{ref}^{p_w}}\eta_{s,\sigma}^{n+1}\Delta\Psi_{K\sigma}^{n,n+1}, \\ \\ -\displaystyle\sum_{\sigma\in\mathcal{F}_K\cap\mathcal{F}_{ext}^{\mathcal{N}}}|\sigma|B_{s,\sigma}^{n+1}=|K|S_{s,K}^n \quad \text{for all } K\in\mathcal{T}, \\ \\ h_{s,\sigma}^{n+1}+b_\sigma^{n+1}=h_{s,K}^{n+1}+b_K^{n+1}+\boldsymbol{G}_{s,K}^{n+1}\cdot(\overline{\boldsymbol{x}}_\sigma-\overline{\boldsymbol{x}}_K) \quad \text{for all } K\in\mathcal{T} \text{ and all } \sigma\in\mathcal{F}_K\cap\mathcal{F}_{ext}^{\mathcal{N}}, \\ \\ h_{s,\sigma}^{n+1}=0 \quad \text{for all } \sigma\in\mathcal{F}_{ext}^{\mathcal{D}}, \end{array}\right.$$

$$-k_g\partial_x\left(|\partial_x h_{s,x}|^{p_s}\partial_x h_{s,x}\right)-\partial_x\left(k_w q_w^{r_s}|\partial_x h_{s,x}|^{p_s}\partial_x h_{s,x}\right)=S_{s,x},$$

~~where~~ which integrating in x leads to (using again our hypothesis on the sign of $\partial_x h_{s,x}$):

$$\Delta\Psi_{KL}^{n,n+1}=(q_{w,\sigma}^{n+1})^{r_s}||\boldsymbol{G}_{s,\sigma}^{\dagger,n+1}||^{p_{s,1}}(\psi_w(h_{s,K}+b_K)-\psi_w(h_{s,L}+b_L))+||\boldsymbol{G}_{s,\sigma}^{\dagger,n+1}||^{p_{s,2}}(\psi_g(h_{s,K}+b_K)-\psi_g(h_{s,L}+b_L)),$$

$$(\partial_x h_{s,x})^{p_s+1}=(-1)^{p_s+1}\frac{S_{s,x}x+\gamma}{k_g+k_w(q_w(0)+S_{w,x}x)^{r_s}},$$

and thus:

$$\Delta\Psi_{K\sigma}^{n,n+1}=(q_{w,\sigma}^{n+1})^{r_s}||\boldsymbol{G}_{s,\sigma}^{\dagger,n+1}||^{p_{s,1}}(\psi_w(h_{s,K}+b_K)-\psi_w(h_{s,\sigma}+b_\sigma))+||\boldsymbol{G}_{s,\sigma}^{\dagger,n+1}||^{p_{s,2}}(\psi_g(h_{s,K}+b_K)-\psi_g(h_{s,\sigma}+b_\sigma)),$$

$$\partial_x h_{s,x}=-\frac{(S_{s,x}x+\gamma)^{\frac{1}{p_s+1}}}{(k_g+k_w(q_w(0)+S_{w,x}x)^{r_s})^{\frac{1}{p_s+1}}}.$$

~~where the mobility $\eta_{s,\sigma}^{n+1}$ is upwinded using $\Delta\Psi_{KL}^{n,n+1}$ for $\sigma\in\mathcal{F}_{int}$~~To ensure the continuity of the derivatives at $x=0$, let us assume that $\partial_x h_{s,x}(0)=0$ and thus $\gamma=0$, and consequently $q_w(0)=0$. The above relation simplifies into:

$$\eta_{s,\sigma}^{n+1}=\left|\begin{array}{ll} \eta_s(h_{s,K}^{n+1}) & \text{if } \Delta\Psi_{KL}^{n,n+1}\geq 0, \\ \\ \eta_s(h_{s,L}^{n+1}) & \text{if } \Delta\Psi_{KL}^{n,n+1}<0, \end{array}\right.$$

$$\partial_x h_{s,x}=-(S_{s,x}x)^{\frac{1}{p_s+1}}(k_g+k_w(S_{w,x}x)^{r_s})^{-\frac{1}{p_s+1}}.$$

~~and using $\Delta\Psi_{K\sigma}^{n,n+1}$ for $\sigma\in\mathcal{F}_{ext}^{\mathcal{D}}$~~Notice that this is coherent with our assumption $-\partial_x h_{s,x}\geq 0$. The water height $h_{w,x}$ can then be obtained by setting:

$$\eta_{s,\sigma}^{n+1}=\left|\begin{array}{ll} \eta_s(h_{s,K}^{n+1}) & \text{if } \Delta\Psi_{K\sigma}^{n,n+1}\geq 0, \\ \\ \eta_s(h_{s,\sigma}^{n+1}) & \text{if } \Delta\Psi_{K\sigma}^{n,n+1}<0, \end{array}\right.$$

$$h_{w,x} = (-1)^{p_w+1}\frac{S_{w,x}x}{\partial_x h_{s,x}^{p_w+1}} = (S_{w,x}x)(S_{s,x}x)^{\frac{-(p_w+1)}{p_s+1}}(k_g + k_w(S_{w,x}x)^{r_s})^{\frac{p_w+1}{p_s+1}},$$

~~and where the filtered water flux magnitude is approximated by the harmonic mean whenever possible and the mean value otherwise~~which is positive as expected. At this stage, integration for $h_{s,x}$ was simpler in **?** because of the absence of k_g. Indeed, for $k_g = 0$ we have:

$$q_{w,\sigma}^{n+1} = \begin{cases} \mathcal{F}_{\alpha,K}^{\mathcal{N}}(q_{w,\mathcal{T}}^{n+1}) & \text{if } \sigma \in \mathcal{F}_{ext}^{\mathcal{D}} \\ \dfrac{\overline{d}_{KL}\mathcal{F}_{\alpha,K}^{\mathcal{N}}(q_{w,\mathcal{T}}^{n+1})\mathcal{F}_{\alpha,L}^{\mathcal{N}}(q_{w,\mathcal{T}}^{n+1})}{\mathcal{F}_{\alpha,K}^{\mathcal{N}}(q_{w,\mathcal{T}}^{n+1})\overline{d}_{L\sigma} + \mathcal{F}_{\alpha,L}^{\mathcal{N}}(q_{w,\mathcal{T}}^{n+1})\overline{d}_{K\sigma}} & \text{if } \sigma \in \mathcal{F}_{int} \text{ and } \mathcal{F}_{\alpha,K}^{\mathcal{N}}(q_{w,\mathcal{T}}^{n+1}) > 0 \text{ and } \mathcal{F}_{\alpha,L}^{\mathcal{N}}(q_{w,\mathcal{T}}^{n+1}) > 0, \\ \dfrac{1}{2}(\mathcal{F}_{\alpha,K}^{\mathcal{N}}(q_{w,\mathcal{T}}^{n+1}) + \mathcal{F}_{\alpha,L}^{\mathcal{N}}(q_{w,\mathcal{T}}^{n+1})) & \text{if } \sigma \in \mathcal{F}_{int} \text{ and } \mathcal{F}_{\alpha,K}^{\mathcal{N}}(q_{w,\mathcal{T}}^{n+1}) = 0 \text{ or } \mathcal{F}_{\alpha,L}^{\mathcal{N}}(q_{w,\mathcal{T}}^{n+1}) = 0. \end{cases}$$

$$\partial_x h_{s,x} = -(S_{s,x}k_w^{-1}S_{w,x}^{-r_s})^{\frac{1}{p_s+1}}x^{\frac{1-r_s}{1+p_s}},$$

~~We recall that the discrete full topographic gradient is given for any cell $K \in \mathcal{T}$ by~~immediately leading to:

$$^{n}_{s,K}h_{s,x} = \frac{1}{|K|}\sum_{\sigma\in\mathcal{F}_K\cap\mathcal{F}_{int}}\frac{|\sigma|}{\overline{d}_{KL}}(h_{s,L}^n + b_L^n - h_{s,K}^n - b_K^n)(_{\sigma}s,x(0) - _{K}\frac{1+p_s}{2+p_s-r_s}(S_{s,x}k_w^{-1}S_{w,x}^{-r_s})^{\frac{1}{p_s+1}}x^{2+p_s-r_s}.$$

Conversely, if $k_w = 0$ (no couling between water and sediments), we have:

$$+\frac{1}{|K|}\sum_{\sigma\in\mathcal{F}_K\cap\mathcal{F}_{ext}}\frac{|\sigma|}{\overline{d}_{K\sigma}}(\partial_x h_{s,\sigma}^n + b_\sigma^n - h_{s,K}^n - b_K^n)(_{\sigma}s,x = -_{K}(k_g^{-1}S_{s,x}x)^{\frac{1}{p_s+1}},$$

~~while its stabilized version $\boldsymbol{G}_{s,\sigma}^{\dagger,n}$ is given by $\boldsymbol{G}_{s,\sigma}^{\dagger,n} = \boldsymbol{G}_{s,\sigma}^{n} + \boldsymbol{R}_{s,\sigma}^{n}$ with~~and thus

$$h_{s,x} = h_{s,x}(0) - \frac{p_s+1}{p_s+2}(k_g^{-1}S_{s,x})^{\frac{1}{p_s+1}}x^{\frac{p_s+2}{p_s+1}}.$$

In the general case we need to compute:

$$\boldsymbol{G}_{s,\sigma}^{n} = \begin{cases} \dfrac{1}{2}(\boldsymbol{G}_{s,K}^{n} + \boldsymbol{G}_{s,L}^{n}) & \text{if } \mathcal{T}_\sigma = \{K,L\}, \\ \boldsymbol{G}_{s,K}^{n} & \text{if } \mathcal{T}_\sigma = \{K\}, \end{cases}$$

$$h_{s,x} = h_{s,x}(0) - \int_0^x (S_{s,x}u)^{\frac{1}{p_s+1}}(k_g + k_w(S_{w,x}u)^{r_s})^{-\frac{1}{p_s+1}}du.$$

~~as well as~~Using the variable change $v = u^{r_s}$, $u = v^{1/r_s}$ and $du = \frac{1}{r_s} v^{(1-r_s)/r_s} dv$ leads to:

$$\boldsymbol{R}^n_{s,\sigma} = \begin{cases} \dfrac{1}{\overline{d}^2_{KL}} \left(h^n_{s,L} + b^n_L - h^n_{s,K} - b^n_K - \boldsymbol{G}^n_{s,\sigma} \cdot (\overline{\boldsymbol{x}}_L - \overline{\boldsymbol{x}}_K) \right) (\overline{\boldsymbol{x}}_L - \overline{\boldsymbol{x}}_K) & \text{if } \mathcal{T}_\sigma = \{K, L\}, \\ \dfrac{1}{\overline{d}^2_{K\sigma}} \left(h^n_{s,\sigma} + b^n_\sigma - h^n_{s,K} - b^n_K - \boldsymbol{G}^n_{s,\sigma} \cdot (\overline{\boldsymbol{x}}_\sigma - \overline{\boldsymbol{x}}_K) \right) (\overline{\boldsymbol{x}}_\sigma - \overline{\boldsymbol{x}}_K) & \text{if } \mathcal{T}_\sigma = \{K\}. \end{cases}$$

$$h_{s,x} = h_{s,x}(0) - \frac{1}{r_s} S_{s,x}^{\frac{1}{p_s+1}} \int_0^{x^{r_s}} v^{\frac{(1-r_s)(p_s+1)+1}{r_s(p_s+1)}} (k_g + k_w S^{r_s}_{w,x} v)^{-\frac{1}{p_s+1}} dv,$$

~~Water equations:~~ ~~The finite volume scheme for the water equations is simply obtained by replacing $(h_{s,K} + b_K)_{K\in\mathcal{T}}$ by $(\mathcal{F}_{\alpha,K}(h^n_{s,\mathcal{T}} + b^n_{\mathcal{T}}))_{K\in\mathcal{T}}$ in . In other words we apply a consistent MFD algorithm on the filtered topography and reconstruct a consistent water flux by setting $q^{n+1}_K = \|\boldsymbol{Q}^{n+1}_K\|$ with~~which will lead to easily computable analytic solutions in particular for the special combinations of values of r_s and p_s that satisifies $(1-r_s)(p_s+1)+1 = 0$ and cancel the exponant $\frac{(1-r_s)(p_s+1)+1}{r_s(p_s+1)}$.

We start by the special case $p_s = 0$ and $r_s = 2$. In this case, we have:

$$\overset{n+1}{K}h_{s,x} = \sum_{\sigma\in\mathcal{F}_K\cap\mathcal{F}_{int}, \mathcal{F}_{\alpha,K}(h^n_{s,\mathcal{T}}+b^n_{\mathcal{T}}) > \mathcal{F}_{\alpha,L}(h^n_{s,\mathcal{T}}+b^n_{\mathcal{T}})} \frac{\tau^{n,n+1}_{KL} \widetilde{q}^{n+1}_K}{|K| s^{n,n+1}_K} (\mathcal{F}_{\alpha,K}(h^n_{s,\mathcal{T}} + b^n_{\mathcal{T}})_{s,x}(0) - \mathcal{F}_{\alpha,L} \frac{1}{2} S_{s,x} \int_0^{x^2} (h^n_{s,\mathcal{T}} k_g + b^n_{\mathcal{T}} k_w S^2_{w,x} v))(\sigma - K)$$

leading to:

$$\sum_{\sigma\in\mathcal{F}_K\cap\mathcal{F}_{int}, \mathcal{F}_{\alpha,K}(h^n_{s,\mathcal{T}}+b^n_{\mathcal{T}}) < \mathcal{F}_{\alpha,L}(h^n_{s,\mathcal{T}}+b^n_{\mathcal{T}})} \frac{\tau^{n,n+1}_{KL} \widetilde{q}^{n+1}_L}{|K| s^{n,n+1}_L} (\mathcal{F}_{\alpha,L}(h^n_{s,\mathcal{T}} + b^n_{\mathcal{T}})_{s,x} = h_{s,x}(0) - \mathcal{F}_{\alpha,K} \frac{S_{s,x}}{2 k_w S^2_{w,x}} (h^n_{s,\mathcal{T}} \ln \left(k_g + b^n_{\mathcal{T}} \right))(\sigma k_w S^2_{w,x} x^2$$

In the other cases for which $(1-r_s)(p_s+1)+1 = 0$, this leads to:

$$- \sum_{\sigma\in\mathcal{F}_K\cap\mathcal{F}_{ext}} |\sigma| B^{n+1}_{w,\sigma},$$

$$h_{s,x} = h_{s,x}(0) - \frac{1}{r_s} S_{s,x}^{\frac{1}{p_s+1}} \int_0^{x^{r_s}} (k_g + k_w S^{r_s}_{w,x} v)^{-\frac{1}{p_s+1}} dv,$$

and thus

$$
\left|
\begin{array}{l}
\widetilde{q}_K^{n+1} - \displaystyle\sum_{\sigma\in\mathcal{F}_K\cap\mathcal{F}_{int},\mathcal{F}_{\alpha,K}(h^n_{s,\mathcal{T}}+b^n_{\mathcal{T}})<\mathcal{F}_{\alpha,L}(h^n_{s,\mathcal{T}}+b^n_{\mathcal{T}})} \tau_{KL}^{n,n+1}\frac{\widetilde{q}_L^{n+1}}{s_L^{n,n+1}}\left(\mathcal{F}_{\alpha,L}(h^n_{s,\mathcal{T}}+b^n_{\mathcal{T}})-\mathcal{F}_{\alpha,K}(h^n_{s,\mathcal{T}}+b^n_{\mathcal{T}})\right)\\
\\
-\displaystyle\sum_{\sigma\in\mathcal{F}_K\cap\mathcal{F}_{ext}} |\sigma|B_{w,\sigma}^{n+1} = |K|S_{w,K}^n \quad \text{for all } K\in\mathcal{T},\\
\\
s_K^{n,n+1} = \displaystyle\sum_{\sigma\in\mathcal{F}_K\cap\mathcal{F}_{int},\mathcal{F}_{\alpha,K}(h^n_{s,\mathcal{T}}+b^n_{\mathcal{T}})\geq\mathcal{F}_{\alpha,L}(h^n_{s,\mathcal{T}}+b^n_{\mathcal{T}})} \tau_{KL}^{n,n+1}\left(\mathcal{F}_{\alpha,K}(h^n_{s,\mathcal{T}}+b^n_{\mathcal{T}})-\mathcal{F}_{\alpha,L}(h^n_{s,\mathcal{T}}+b^n_{\mathcal{T}})\right)\\
\\
\tau_{KL}^{n,n+1} = \dfrac{|\sigma|k_{m,\sigma}^{n+1}}{\bar{d}_{KL}s_{ref}^{p_w}}||\boldsymbol{G}^n_{\mathcal{F},s,\sigma}||^{p_w},
\end{array}
\right.
$$

$$h_{s,x} = h_{s,x}(0) - \frac{p_s+1}{p_s r_s}\frac{S_{s,x}^{\frac{1}{p_s+1}}}{k_w S_{w,x}^{r_s}}((k_g + k_w S_{w,x}^{r_s}x^{r_s})^{p_s/(p_s+1)} - k_g^{p_s/(p_s+1)})$$

~~where~~

$$
\boldsymbol{G}^n_{\mathcal{F},s,\sigma} = \left|
\begin{array}{ll}
\dfrac{1}{2}(\boldsymbol{G}^n_{\mathcal{F},s,K}+\boldsymbol{G}^n_{\mathcal{F},s,L}) & \text{if } \mathcal{T}_\sigma = \{K,L\},\\
\\
\boldsymbol{G}^n_{\mathcal{F},s,K} & \text{if } \mathcal{T}_\sigma = \{K\},
\end{array}
\right.
$$

~~and the gradient of the filtered topography is of course given by~~Apart from those cases than cancels the exponant appearing in the intregral, another interesting special case is the linear case $p_s = 0$ and $r_s = 1$ for which we have:

$$\overset{n}{\mathcal{F}},s,K h_{s,x} = \frac{1}{|K|}\sum_{\sigma\in\mathcal{F}_K\cap\mathcal{F}_{int}}\frac{|\sigma|}{\bar{d}_{KL}}(\mathcal{F}_{\alpha,L}(h^n_{s,\mathcal{T}}+b^n_{\mathcal{T}})_{s,x}(0) - \mathcal{F}_{\alpha,K}\int_0^x (h^n_{s,\mathcal{T}}+b^n_{\mathcal{T}}S_{s,x}u))(_{\sigma-K}k_g + k_w(S_{w,x}u))^{-1}du,$$

which leads to:

$$+\frac{1}{|K|}\sum_{\sigma\in\mathcal{F}_K\cap\mathcal{F}_{ext}}\frac{|\sigma|}{\bar{d}_{K\sigma}}(\mathcal{F}_{\alpha,\sigma}(h^n_{s,\mathcal{T}}+b^n_{\mathcal{T}}) - \mathcal{F}_{\alpha,K}(_{s,x} = h^n_{s,\mathcal{T}}+b^n_{\mathcal{T}}))(_{\sigma s,x}(0) - S_{s,x}\left(\frac{x}{k_w S_{w,x}} - _K)\frac{k_g}{k_w^2 S_{w,x}^2}\ln\left|k_g + k_w S_{w,x}x\right| + \frac{k_g}{k_w^2 S_{w,x}^2}\right.$$

It is then easy to choose the value for $h_{s,x}(0)$ such that $h_{s,x}(Lx/2) = 0$.

Appendix B: From shallow water model to the steady-state hydrologic model (??)

Recall that the shallow water systems is given by (see **??**):

$$
\left|
\begin{array}{l}
\dfrac{\partial h_w}{\partial t} + div(h_w\boldsymbol{u}_w) = 0,\\
\dfrac{\partial}{\partial t}(h_w\boldsymbol{u}_w) + div(h_w\boldsymbol{u}_w\otimes\boldsymbol{u}_w) + gh_w\nabla(h_s+b+h_w) = -\kappa_w\left(h_w, ||\nabla(h_w+h_s+b)||\right)|\boldsymbol{u}_w|^{r_w}\boldsymbol{u}_w,
\end{array}
\right. \tag{B1}
$$

where $\boldsymbol{u}_w$ denotes the water speed, g the acceleration due to gravity, and κ_w is the friction coefficient. Then, following **?** and defining $H_{s,c}$ to be the characteristic sediment height, $H_{w,c}$ the characteristic water height, L_c the characteristic domain length, T_c the characteristic time and defining the nondimensional variables:

$$\hat{h}_s = \frac{h_s}{H_{s,c}}, \quad \hat{b}_s = \frac{b}{H_{s,c}}, \quad \hat{h}_w = \frac{h_w}{H_{w,c}}, \quad \hat{\boldsymbol{u}}_w = \frac{T_c \boldsymbol{u}_w}{L_c}, \quad \hat{x} = \frac{x}{L_c}, \quad \hat{y} = \frac{y}{L_c}, \quad \hat{t} = \frac{t}{T_c},$$

we see that (**??**) is equivalent to:

$$\left|\begin{array}{l} \dfrac{\partial \hat{h}_w}{\partial \hat{t}} + \hat{div}(\hat{h}_w \hat{\boldsymbol{u}}_w) = 0, \\ \dfrac{\partial}{\partial \hat{t}}(\hat{h}_w \hat{\boldsymbol{u}}_w) + \hat{div}(\hat{h}_w \hat{\boldsymbol{u}}_w \otimes \hat{\boldsymbol{u}}_w) + g\dfrac{H_{s,c}T_c^2}{L_c^2}\hat{h}_w \hat{\nabla}(\hat{h}_s + \hat{b}) + g\dfrac{H_{w,c}T_c^2}{L_c^2}\hat{h}_w \hat{\nabla}(\hat{h}_w), \\ = -\kappa_w\left(h_w, ||\nabla(h_w + h_s + b)||\right)\dfrac{L_c}{H_{w,c}}\left(\dfrac{L_c}{T_c}\right)^{r_w - 1} |\hat{\boldsymbol{u}}_w|^{r_w}\hat{\boldsymbol{u}}_w. \end{array}\right.$$

The "shallow" hypothesis corresponds to assuming that $L_c/H_{w,c} >> 1$, while the two numbers

$$F_{r,w} = \frac{L_c}{\sqrt{gH_{w,c}}T_c} \quad \text{and} \quad F_{r,s} = \frac{L_c}{\sqrt{gH_{s,c}}T_c},$$

are equivalent to Froude numbers for the water and sediment flows. For long term sediment evolution, it is reasonable to assume that $F_{r,w} << 1$ and $F_{r,s} << 1$, i.e. that gravity is the dominant phenomenon. Combined with the shallow water assumption this suggests to neglect the inertia terms in the nondimensional momentum balance, leading to the hydrostatic assumption:

$$gh_w \nabla(h_s + b + h_w) = -\kappa_w\left(h_w, ||\nabla(h_w + h_s + b)||\right)|\boldsymbol{u}_w|^{r_w}\boldsymbol{u}_w, \tag{B2}$$

Inverting formula (**??**) we obtain the following expression for the water speed:

$$\boldsymbol{u}_w = -\mu_w\left(h_w, ||\nabla(h_w + h_s + b)||\right)\nabla(h_s + b + h_w), \tag{B3}$$

where

$$\mu_w\left(h_w, ||\nabla(h_w + h_s + b)||\right) = \frac{g^{\frac{1}{r_w+1}} h_w^{\frac{1}{r_w+1}}}{\kappa_w\left(h_w, ||\nabla(h_w + h_s + b)||\right)^{\frac{1}{r_w+1}}} ||\nabla(h_s + b + h_w)||^{-\frac{r_w}{r_w+1}}. \tag{B4}$$

Thus, appropriately choosing the friction model, for instance by setting $r_w = 0$ and

$$\kappa_w\left(h_w, ||\nabla(h_w + h_s + b)||\right) = \frac{gh_w}{k_m \eta_w(h_w) s_{ref}^{-p_w} ||\nabla(h_w + h_s + b)||^{p_w}}, \tag{B5}$$

and assuming that the mass conservation of water is at steady state we obtain the following quite general hydrostatic approximation to the shallow water equations:

$$\left|\begin{array}{ll} -div\left(k_m h_w \eta_w\left(h_w\right) s_{ref}^{-p_w} ||\nabla(h_w + h_s + b)||^{p_w}\nabla(h_w + h_s + b)\right) = S_w & \text{in } \Omega, \\ -k_m h_w \eta_w\left(h_w\right) s_{ref}^{-p_w} ||\nabla(h_w + h_s + b)||^{p_w}\nabla(h_w + h_s + b)\cdot n = B_w & \text{on } \partial\Omega_{\mathcal{N}}, \\ h_w = 0 & \text{on } \partial\Omega_{\mathcal{D}}, \end{array}\right.$$

with the associated water flux strength:

$$q_w = |k_m h_w \eta_w(h_w)|\, s_{ref}^{-p_w} ||\nabla(h_w + h_s + b)||^{p_w+1}.$$

Remark B.1. The friction model (**??**) becomes singular when $||\nabla(h_w + h_s + b)|| = 0$. Thus, an alternate choice would be to use something like:

$$\kappa_w(h_w, ||\nabla(h_w + h_s + b)||) = \frac{g h_w}{k_m \eta_w(h_w)(\beta + s_{ref}^{-p_w} ||\nabla(h_w + h_s + b)||^{p_w})},$$

for some $\beta > 0$ (the same holds for function η_w such that $\eta(0) = 0$). This alternate choice is probably more physical, as the term in $s_{ref}^{-p_w} ||\nabla(h_w + h_s + b)||^{p_w}$ can be interpreted as modeling some deceleration in accumulation areas. We have chosen to use (**??**) to be as close as possible to the MFD algorithms of the literature.

Appendix C: Finite volume discretization

In this section we describe the full finite volume discretization of system (**??**)-(**??**)-(**??**)-(**??**). Let Ω be a bounded polyhedral connected domain of $\mathbb{R}^2$, whose boundary is denoted $\partial\Omega = \overline{\Omega} \setminus \Omega$. We recall the usual finite volume notations describing a mesh $\mathcal{M} = (\mathcal{T}, \mathcal{F})$ of Ω. The set of the cells of the mesh $\mathcal{T}$ is a finite family of connected open disjoint polygonal subsets of Ω, such that $\overline{\Omega} = \cup_{K \in \mathcal{T}} \overline{K}$. For any $K \in \mathcal{T}$, we denote by $|K|$ the measure of $|K|$, by $\partial K = \overline{K} \setminus K$ the boundary of K, by ρ_K its diameter and by $\boldsymbol{x}_K$ its barycenter. The set of faces of the mesh $\mathcal{F}$ is a finite family of disjoint subsets of $\mathbb{R}^2$ included in $\overline{\Omega}$ such that, for all $\sigma \in \mathcal{F}$, its measure is denoted $|\sigma|$, its diameter h_σ and its barycenter $\boldsymbol{x}_\sigma$. For any $K \in \mathcal{T}$, the faces of cells K corresponds to the subset $\mathcal{F}_K$ of $\mathcal{F}$ such that $\partial K = \cup_{\sigma \in \mathcal{F}_K} \overline{\sigma}$. Then, for any face $\sigma \in \mathcal{F}$, we denote by $\mathcal{T}_\sigma = \{K \in \mathcal{T} \,|\, \sigma \in \mathcal{F}_K\}$ the cells of which σ is a face. Next, for all cell $K \in \mathcal{T}$ and all face $\sigma \in \mathcal{F}_K$ of cell K, we denote by $\boldsymbol{n}_{K,\sigma}$ the unit normal vector to σ outward to K, and $d_{K,\sigma} = |\boldsymbol{x}_\sigma - \boldsymbol{x}_K|$. The set of boundary faces is denoted $\mathcal{F}_{ext}$, while interior faces are denoted $\mathcal{F}_{int}$. Finally for any $\sigma \in \mathcal{F}_{int}$, whenever the context is clear we will denote by K and L the two cells forming $\mathcal{T}_\sigma = \{K, L\}$, as well as $d_{KL} = |\boldsymbol{x}_K - \boldsymbol{x}_L|$. This for instance allows when looping over the faces σ of cell K to denote by L the other face of σ without resorting to a too heavy notation. To avoid any confusion with water and sediment heights, $\epsilon = \max_{K \in \mathcal{T}} \rho_K$ will denote the mesh size. For any continuous quantity u, its discrete counterpart will be denoted $u_\mathcal{T} = ((u_K)_{K \in \mathcal{T}}, (u_\sigma)_{\sigma \in \mathcal{F}_{ext}})$ where for any $K \in \mathcal{T}$ u_K is the constant approximation of u in cell K while for any $\sigma \in \mathcal{F}_{ext}$ u_σ is the constant approximation of u over face σ.

In the following we will assume that the mesh is orthogonal, i.e. there exists a family of centroids $(\overline{\boldsymbol{x}}_K)_{K \in \mathcal{T}}$ such that:

$$\overline{\boldsymbol{x}}_K \in \overline{K} \quad \forall K \in \mathcal{T} \quad \text{and} \quad \frac{\overline{\boldsymbol{x}}_L - \overline{\boldsymbol{x}}_K}{|\overline{\boldsymbol{x}}_L - \overline{\boldsymbol{x}}_K|} = \boldsymbol{n}_{K,\sigma} \quad \text{for} \quad \sigma \in \mathcal{F}_{int},\ \sigma = \{K, L\}$$

and let us denote $\overline{\boldsymbol{x}}_\sigma$ the orthogonal projection of $\overline{\boldsymbol{x}}_K$ to the hyperplane containing σ for any $\sigma \in \mathcal{F}_K$ and any $K \in \mathcal{T}$ with $\overline{d}_{K,\sigma} = |\overline{\boldsymbol{x}}_K - \overline{\boldsymbol{x}}_\sigma|$, as well as $\overline{d}_{KL} = |\overline{\boldsymbol{x}}_K - \overline{\boldsymbol{x}}_L|$. Then, one can use a two-point finite volume scheme to discretize diffusion operators with scalar diffusion coefficients (no tensors). We also assume that the mesh is compatible with the boundary

decomposition, i.e. there exists subsets $\mathcal{F}_{ext}^{\mathcal{N}}$ and $\mathcal{F}_{ext}^{\mathcal{D}}$ such that:

$$\overline{\partial\Omega_{\mathcal{N}}} = \bigcup_{\sigma\in\mathcal{F}_{ext}^{\mathcal{N}}} \overline{\sigma} \quad \text{and} \quad \overline{\partial\Omega_{\mathcal{D}}} = \bigcup_{\sigma\in\mathcal{F}_{ext}^{\mathcal{D}}} \overline{\sigma}.$$

Notice that all our simulations without filters employs the same numerical schemes but of course replacing the filtered values by the original ones.

Leray-α filtering equation:

Using the two-point flux approximation (TPFA) the approximate filter $\mathcal{F}_{\alpha,h}$ is defined for

$u_{\mathcal{T}} = ((u_K)_{K\in\mathcal{T}}, (u_\sigma)_{\sigma\in\mathcal{F}_{ext}})$

by

$\mathcal{F}_{\alpha,h}(u_{\mathcal{T}}) = ((\mathcal{F}_{\alpha,K}(u_{\mathcal{T}}))_{K\in\mathcal{T}}, (\mathcal{F}_{\alpha,\sigma}(u_{\mathcal{T}}))_{\sigma\in\mathcal{F}_{ext}})$,

where:

$$\left|\begin{array}{l}
\alpha^2 \displaystyle\sum_{\sigma\in\mathcal{F}_K\cap\mathcal{F}_{int}} \frac{|\sigma|}{\overline{d}_{KL}}(\mathcal{F}_{\alpha,K}(u_{\mathcal{T}}) - \mathcal{F}_{\alpha,L}(u_{\mathcal{T}})) + |K|\mathcal{F}_{\alpha,K}(u_{\mathcal{T}}) = |K|u_K \quad \text{for all } K\in\mathcal{T},\\[2ex]
\mathcal{F}_{\alpha,\sigma}(u_{\mathcal{T}}) = \mathcal{F}_{\alpha,K}(u_{\mathcal{T}}) \quad \text{for all } K\in\mathcal{T} \text{ and all } \sigma\in\mathcal{F}_K\cap\mathcal{F}_{ext}^{\mathcal{N}},\\[2ex]
\mathcal{F}_{\alpha,\sigma}(u_{\mathcal{T}}) = 0 \quad \text{for all } K\in\mathcal{T} \text{ and all } \sigma\in\mathcal{F}_K\cap\mathcal{F}_{ext}^{\mathcal{D}}.
\end{array}\right. \tag{C1}$$

The discrete Neumann filter $\mathcal{F}_{\alpha,h}^{\mathcal{N}}$ of course satisfies (**??**) but with Neumann boundary conditions on every $\sigma\in\mathcal{F}_{ext}$.

Sediment mass conservation equations:

We now assume that the time interval $]0,T[$ is subdivided into N_T subintervals $]t_n, t_{n+1}[$, where $t_0 = 0$ and $t_{N_T+1} = T$. We denote $\Delta t^n = t_{n+1} - t_n$. The discrete quantities associated with time t_n will be denoted as usual with a superscript n. The TPFA finite volume scheme for the mass conservation of sediments (**??**) for the flux (**??**) is given by:

$$\left|\begin{array}{l}
\dfrac{|K|}{\Delta t^n}(h_{s,K}^{n+1} - h_{s,K}^n) + \displaystyle\sum_{\sigma\in\mathcal{F}_K\cap\mathcal{F}_{int}} \frac{|\sigma|}{\overline{d}_{KL}s_{ref}^{p_w}} \eta_{s,\sigma}^{n+1}\Delta\Psi_{KL}^{n,n+1} + \sum_{\sigma\in\mathcal{F}_K\cap\mathcal{F}_{ext}^{\mathcal{D}}} \frac{|\sigma|}{\overline{d}_{K\sigma}s_{ref}^{p_w}} \eta_{s,\sigma}^{n+1}\Delta\Psi_{K\sigma}^{n,n+1},\\[2ex]
-\displaystyle\sum_{\sigma\in\mathcal{F}_K\cap\mathcal{F}_{ext}^{\mathcal{N}}} |\sigma|B_{s,\sigma}^{n+1} = |K|S_{s,K}^n \quad \text{for all } K\in\mathcal{T},\\[2ex]
h_{s,\sigma}^{n+1} + b_\sigma^{n+1} = h_{s,K}^{n+1} + b_K^{n+1} + \boldsymbol{G}_{s,K}^{n+1}\cdot(\overline{\boldsymbol{x}}_\sigma - \overline{\boldsymbol{x}}_K) \quad \text{for all } K\in\mathcal{T} \text{ and all } \sigma\in\mathcal{F}_K\cap\mathcal{F}_{ext}^{\mathcal{N}},\\[2ex]
h_{s,\sigma}^{n+1} = 0 \quad \text{for all } \sigma\in\mathcal{F}_{ext}^{\mathcal{D}},
\end{array}\right. \tag{C2}$$

where

$$\Delta\Psi_{KL}^{n,n+1} = (q_{w,\sigma}^{n+1})^{r_s}||\boldsymbol{G}_{s,\sigma}^{\dagger,n+1}||^{p_{s,1}}(\psi_w(h_{s,K}+b_K)-\psi_w(h_{s,L}+b_L)) + ||\boldsymbol{G}_{s,\sigma}^{\dagger,n+1}||^{p_{s,2}}(\psi_g(h_{s,K}+b_K)-\psi_g(h_{s,L}+b_L)), \tag{C3}$$

and

$$\Delta\Psi_{K\sigma}^{n,n+1} = (q_{w,\sigma}^{n+1})^{r_s}||\boldsymbol{G}_{s,\sigma}^{\dagger,n+1}||^{p_{s,1}}(\psi_w(h_{s,K}+b_K)-\psi_w(h_{s,\sigma}+b_\sigma)) + ||\boldsymbol{G}_{s,\sigma}^{\dagger,n+1}||^{p_{s,2}}(\psi_g(h_{s,K}+b_K)-\psi_g(h_{s,\sigma}+b_\sigma)), \tag{C4}$$

where the mobility $\eta_{s,\sigma}^{n+1}$ is upwinded using $\Delta\Psi_{KL}^{n,n+1}$ for $\sigma \in \mathcal{F}_{int}$:

$$\eta_{s,\sigma}^{n+1} = \begin{cases} \eta_s(h_{s,K}^{n+1}) & \text{if } \Delta\Psi_{KL}^{n,n+1} \geq 0, \\ \eta_s(h_{s,L}^{n+1}) & \text{if } \Delta\Psi_{KL}^{n,n+1} < 0, \end{cases} \tag{C5}$$

and using $\Delta\Psi_{K\sigma}^{n,n+1}$ for $\sigma \in \mathcal{F}_{ext}^{\mathcal{D}}$:

$$\eta_{s,\sigma}^{n+1} = \begin{cases} \eta_s(h_{s,K}^{n+1}) & \text{if } \Delta\Psi_{K\sigma}^{n,n+1} \geq 0, \\ \eta_s(h_{s,\sigma}^{n+1}) & \text{if } \Delta\Psi_{K\sigma}^{n,n+1} < 0, \end{cases} \tag{C6}$$

and where the filtered water flux magnitude is approximated by the harmonic mean whenever possible and the mean value otherwise:

$$q_{w,\sigma}^{n+1} = \begin{cases} \mathcal{F}_{\alpha,K}^{\mathcal{N}}(q_{w,\mathcal{T}}^{n+1}) & \text{if } \sigma \in \mathcal{F}_{ext}^{\mathcal{D}} \\ \dfrac{\overline{d}_{KL}\mathcal{F}_{\alpha,K}^{\mathcal{N}}(q_{w,\mathcal{T}}^{n+1})\mathcal{F}_{\alpha,L}^{\mathcal{N}}(q_{w,\mathcal{T}}^{n+1})}{\mathcal{F}_{\alpha,K}^{\mathcal{N}}(q_{w,\mathcal{T}}^{n+1})\overline{d}_{L\sigma}+\mathcal{F}_{\alpha,L}^{\mathcal{N}}(q_{w,\mathcal{T}}^{n+1})\overline{d}_{K\sigma}} & \text{if } \sigma \in \mathcal{F}_{int} \text{ and } \mathcal{F}_{\alpha,K}^{\mathcal{N}}(q_{w,\mathcal{T}}^{n+1}) > 0 \text{ and } \mathcal{F}_{\alpha,L}^{\mathcal{N}}(q_{w,\mathcal{T}}^{n+1}) > 0, \\ \dfrac{1}{2}(\mathcal{F}_{\alpha,K}^{\mathcal{N}}(q_{w,\mathcal{T}}^{n+1}) + \mathcal{F}_{\alpha,L}^{\mathcal{N}}(q_{w,\mathcal{T}}^{n+1})) & \text{if } \sigma \in \mathcal{F}_{int} \text{ and } \mathcal{F}_{\alpha,K}^{\mathcal{N}}(q_{w,\mathcal{T}}^{n+1}) = 0 \text{ or } \mathcal{F}_{\alpha,L}^{\mathcal{N}}(q_{w,\mathcal{T}}^{n+1}) = 0. \end{cases} \tag{C7}$$

The discrete full topographic gradient is given for any cell $K \in \mathcal{T}$ by:

$$\boldsymbol{G}_{s,K}^{n} = \frac{1}{|K|}\sum_{\sigma\in\mathcal{F}_K\cap\mathcal{F}_{int}}\frac{|\sigma|}{\overline{d}_{KL}}(h_{s,L}^n + b_L^n - h_{s,K}^n - b_K^n)(\boldsymbol{x}_\sigma - \boldsymbol{x}_K)$$

$$+\frac{1}{|K|}\sum_{\sigma\in\mathcal{F}_K\cap\mathcal{F}_{ext}}\frac{|\sigma|}{\overline{d}_{K\sigma}}(h_{s,\sigma}^n + b_\sigma^n - h_{s,K}^n - b_K^n)(\boldsymbol{x}_\sigma - \boldsymbol{x}_K),$$

while its stabilized version $\boldsymbol{G}^{\dagger,n}_{s,\sigma}$ is given by $\boldsymbol{G}^{\dagger,n}_{s,\sigma} = \boldsymbol{G}^{n}_{s,\sigma} + \boldsymbol{R}^{n}_{s,\sigma}$ with:

$$\boldsymbol{G}^{n}_{s,\sigma} = \begin{cases} \dfrac{1}{2}(\boldsymbol{G}^{n}_{s,K} + \boldsymbol{G}^{n}_{s,L}) & \text{if } \mathcal{T}_\sigma = \{K, L\}, \\ \boldsymbol{G}^{n}_{s,K} & \text{if } \mathcal{T}_\sigma = \{K\}, \end{cases} \tag{C8}$$

as well as:

$$\boldsymbol{R}^{n}_{s,\sigma} = \begin{cases} \dfrac{1}{\overline{d}^2_{KL}} \left(h^n_{s,L} + b^n_L - h^n_{s,K} - b^n_K - \boldsymbol{G}^{n}_{s,\sigma} \cdot (\overline{\boldsymbol{x}}_L - \overline{\boldsymbol{x}}_K)\right)(\overline{\boldsymbol{x}}_L - \overline{\boldsymbol{x}}_K) & \text{if } \mathcal{T}_\sigma = \{K, L\}, \\ \dfrac{1}{\overline{d}^2_{K\sigma}} \left(h^n_{s,\sigma} + b^n_\sigma - h^n_{s,K} - b^n_K - \boldsymbol{G}^{n}_{s,\sigma} \cdot (\overline{\boldsymbol{x}}_\sigma - \overline{\boldsymbol{x}}_K)\right)(\overline{\boldsymbol{x}}_\sigma - \overline{\boldsymbol{x}}_K) & \text{if } \mathcal{T}_\sigma = \{K\}. \end{cases} \tag{C9}$$

Water equations:

The finite volume scheme for the water equations (**??**)-(**??**) is simply obtained by applying the corrected MFD algorithm of **?** on the filtered topography and reconstructing a consistent water flux by setting $q^{n+1}_K = ||\boldsymbol{Q}^{n+1}_K||$ with:

$$\begin{aligned} \boldsymbol{Q}^{n+1}_K = & \sum_{\sigma \in \mathcal{F}_K \cap \mathcal{F}_{int}, \mathcal{F}_{\alpha,K}(h^n_{s,\mathcal{T}} + b^n_{\mathcal{T}}) > \mathcal{F}_{\alpha,L}(h^n_{s,\mathcal{T}} + b^n_{\mathcal{T}})} \frac{\tau^{n,n+1}_{KL} \widetilde{q}^{n+1}_K}{|K| s^{n,n+1}_K} (\mathcal{F}_{\alpha,K}(h^n_{s,\mathcal{T}} + b^n_{\mathcal{T}}) - \mathcal{F}_{\alpha,L}(h^n_{s,\mathcal{T}} + b^n_{\mathcal{T}}))(\boldsymbol{x}_\sigma - \boldsymbol{x}_K) - \\ & \sum_{\sigma \in \mathcal{F}_K \cap \mathcal{F}_{int}, \mathcal{F}_{\alpha,K}(h^n_{s,\mathcal{T}} + b^n_{\mathcal{T}}) < \mathcal{F}_{\alpha,L}(h^n_{s,\mathcal{T}} + b^n_{\mathcal{T}})} \frac{\tau^{n,n+1}_{KL} \widetilde{q}^{n+1}_L}{|K| s^{n,n+1}_L} (\mathcal{F}_{\alpha,L}(h^n_{s,\mathcal{T}} + b^n_{\mathcal{T}}) - \mathcal{F}_{\alpha,K}(h^n_{s,\mathcal{T}} + b^n_{\mathcal{T}}))(\boldsymbol{x}_\sigma - \boldsymbol{x}_K) \\ & - \sum_{\sigma \in \mathcal{F}_K \cap \mathcal{F}_{ext}} |\sigma| B^{n+1}_{w,\sigma}, \end{aligned} \tag{C10}$$

and

$$\begin{cases} \widetilde{q}^{n+1}_K - \displaystyle\sum_{\sigma \in \mathcal{F}_K \cap \mathcal{F}_{int}, \mathcal{F}_{\alpha,K}(h^n_{s,\mathcal{T}} + b^n_{\mathcal{T}}) < \mathcal{F}_{\alpha,L}(h^n_{s,\mathcal{T}} + b^n_{\mathcal{T}})} \tau^{n,n+1}_{KL} \frac{\widetilde{q}^{n+1}_L}{s^{n,n+1}_L} \left(\mathcal{F}_{\alpha,L}(h^n_{s,\mathcal{T}} + b^n_{\mathcal{T}}) - \mathcal{F}_{\alpha,K}(h^n_{s,\mathcal{T}} + b^n_{\mathcal{T}})\right) \\ - \displaystyle\sum_{\sigma \in \mathcal{F}_K \cap \mathcal{F}_{ext}} |\sigma| B^{n+1}_{w,\sigma} = |K| S^n_{w,K} \quad \text{for all } K \in \mathcal{T}, \\ s^{n,n+1}_K = \displaystyle\sum_{\sigma \in \mathcal{F}_K \cap \mathcal{F}_{int}, \mathcal{F}_{\alpha,K}(h^n_{s,\mathcal{T}} + b^n_{\mathcal{T}}) \geq \mathcal{F}_{\alpha,L}(h^n_{s,\mathcal{T}} + b^n_{\mathcal{T}})} \tau^{n,n+1}_{KL} \left(\mathcal{F}_{\alpha,K}(h^n_{s,\mathcal{T}} + b^n_{\mathcal{T}}) - \mathcal{F}_{\alpha,L}(h^n_{s,\mathcal{T}} + b^n_{\mathcal{T}})\right) \\ \tau^{n,n+1}_{KL} = \dfrac{|\sigma| k^{n+1}_{m,\sigma}}{\overline{d}_{KL} s^{p_w}_{ref}} ||\boldsymbol{G}^n_{\mathcal{F},s,\sigma}||^{p_w}, \end{cases} \tag{C11}$$

where

$$\boldsymbol{G}^n_{\mathcal{F},s,\sigma} = \begin{cases} \frac{1}{2}(\boldsymbol{G}^n_{\mathcal{F},s,K} + \boldsymbol{G}^n_{\mathcal{F},s,L}) & \text{if } \mathcal{T}_\sigma = \{K, L\}, \\ \boldsymbol{G}^n_{\mathcal{F},s,K} & \text{if } \mathcal{T}_\sigma = \{K\}, \end{cases} \tag{C12}$$

and the gradient of the filtered topography is of course given by:

$$\boldsymbol{G}^n_{\mathcal{F},s,K} = \frac{1}{|K|} \sum_{\sigma \in \mathcal{F}_K \cap \mathcal{F}_{int}} \frac{|\sigma|}{\bar{d}_{KL}} (\mathcal{F}_{\alpha,L}(h^n_{s,\mathcal{T}} + b^n_{\mathcal{T}}) - \mathcal{F}_{\alpha,K}(h^n_{s,\mathcal{T}} + b^n_{\mathcal{T}}))(\boldsymbol{x}_\sigma - \boldsymbol{x}_K)$$

$$+ \frac{1}{|K|} \sum_{\sigma \in \mathcal{F}_K \cap \mathcal{F}_{ext}} \frac{|\sigma|}{\bar{d}_{K\sigma}} (\mathcal{F}_{\alpha,\sigma}(h^n_{s,\mathcal{T}} + b^n_{\mathcal{T}}) - \mathcal{F}_{\alpha,K}(h^n_{s,\mathcal{T}} + b^n_{\mathcal{T}}))(\boldsymbol{x}_\sigma - \boldsymbol{x}_K).$$

Author contributions. Julien Coatléven: conceptualization, writing, software, simulations. Benoit Chauveau: writing, software, simulations

Competing interests. Both the authors are core developers of the ArcaDES simulator supporting DionisosFlow™, a commercial stratigraphic simulator.

Acknowledgements. The authors would like to thank John J. Armitage and Didier Granjeon for their careful reading of the present paper.

Results with filters and Perlin noise based k_m coefficient. a : results for (α, Δ_{xy})= (1.2 km, 1 km), a : results for (α, Δ_{xy})= (1.2 km, 0.25 km), c: results for (α, Δ_{xy})= (0.3 km, 0.25 km), d: results for (α, Δ_{xy})= (0.3 km, 0.25 km) with additional Perlin noise based perturbation of rain fall Front view of the result of figure **??**-d The two synthetic sedimentary systems we have presented so far can be considered as large-scale configurations. However, some structures emerge clearly at lower spatial scales, as it can be seen in the Gabilan Mesa (California), a case already discussed in detail in **?** and **?** and **?**.We perform a third synthetic case study that has two particularities compared to the two previous ones. First the length scale considered here is small: the domain simulation is a rectangular area of 5 km width over 10 km long and the mesh size mesh size is $\Delta_{xy} = 4$ meters. The filter size is $\alpha = 6$ meters, respecting $\alpha > \Delta_{xy}$. Second, there is no heterogeneity but the sediment production zone ($S_s = 100$ m.My^{-1}) is a rectangular sub-area which creates topographic discontinuities at the sub-area boundaries. For the other parameters, we keep a similar configuration. Rain-fall is constant in time and space (3000 mm/y) and is the unique water supply. Diffusive coefficients are chosen constant with k_g=0.05 km^2.My^{-1} and k_w= 50000 km^2.My^{-1}, and models parameters controlling the non-linearity in the water-sediment coupling are set as $r_s = 2$, $p_s = 0$. Simulation is performed over 3 millions and a steady state is achieved. Results are shown in Fig. **??**. The first observation done at the scale of the whole numerical domain shows without any ambiguity the capacity of our model in particularly well preserving symmetry in the sub-area. This is less true outside the sub-area and the reason is probably because the slopes are so gentle that some zones they are considered by the model as flat area, which is not in agreement with the drainage assumption. Second observation is done by comparing the spacing between valleys in this simulation with the valleys spacing observed in the Gabilan Mesa. In our model the valley are spaced by a lenghtscale of approximately 160 meters, which is at the first order relatively close to what is observed in the Galiban Mesa. The third observation concerns the high values of τ here obtained through small values of k_g necessary to obtain such narrow valleys. With all other parameters left unchanged, we observed that higher values of k_g lead to larger valleys. For such high values of τ, this test case highlights the absolute necessity of using filters to reproduce realistic structures at such spatial scales.

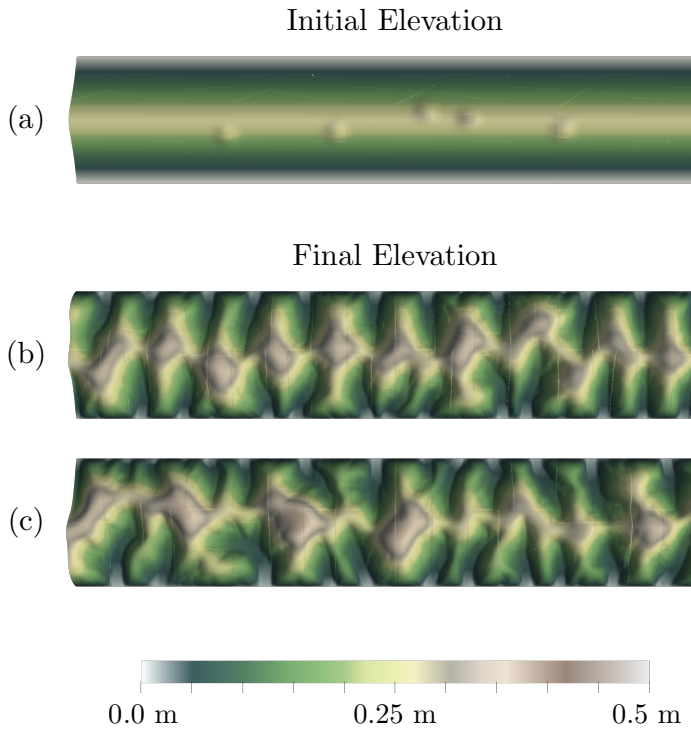

Figure 21. Application of our model on a small-scale synthetic sedimentary system (top view). The global domain is 10×5 km^2. Results with a grid resolution $\Delta_{xy} = 4$ metersfilters and Perlin noise based k_m coefficient. The filter size is $\alpha = 6$ meters. The red square corresponds

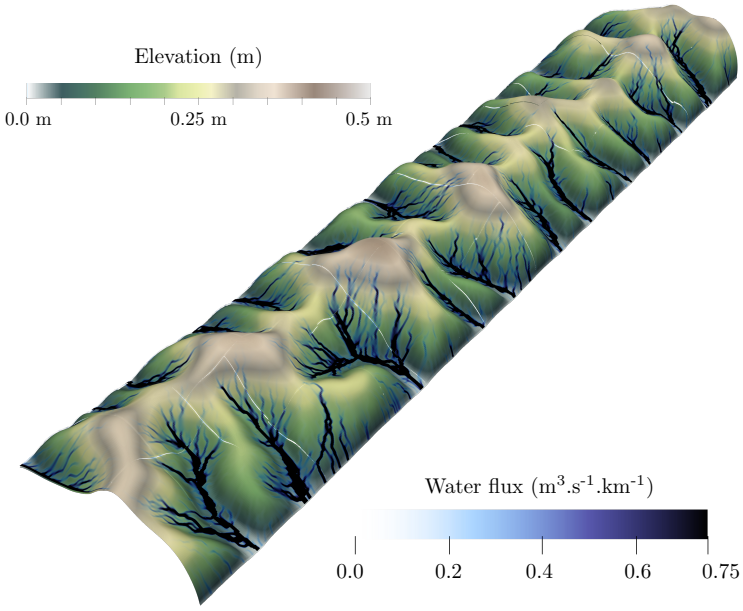

Figure 22. Front view of the result of figure **??**-c

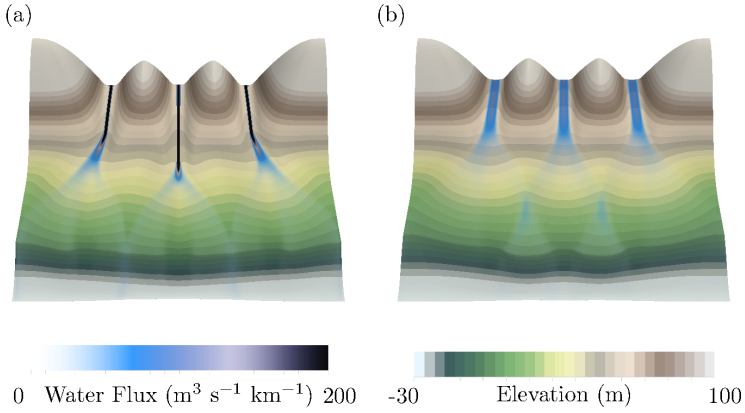

Figure 23. Comparison of models (**??**) and (**??**) on the "three rivers" test case for α=2200 m and Δ_{xy}=2000 m